

POLITECNICO DI TORINO

Dipartimento di Ingegneria Meccanica e Aerospaziale

Corso di Laurea Magistrale in Ingegneria Aerospaziale



Tesi di Laurea Magistrale

Lunar Nano Drone for a mission of exploration of lava tubes on the Moon: Navigation System

Relatore

Prof. Paolo Maggiore

Candidato

Gael Latiro

Co-relatori

Ing. Piero Messidoro

Gen. Roberto Vittori

Ing. Nicolas Bellomo

Matricola

257622

Dicembre 2020

Acknowledgment

There are many people whom I would like to thank for their contributions, both directly and indirectly, to this thesis.

I would first like to thank my supervisor prof Paolo Maggiore which allowed me to carry out this thesis and make contacts with leading figures in the sector.

I also want to thank Eng. Piero Messidoro for his precious help both in terms of logistics and for the experience he shared with us.

To Nicolas Bellomo who helped us enormously despite his constant commitment to work.

Finally, I want to thank the astronaut as well as General Roberto Vittori for his precious help both as a reference and contact figure and as the creator of the project.

To my parents and friends, in particular to my best friend Matteo Lertora who has always supported me and has always been there since I can remember.

To my grandmother, who helped me a lot and unfortunately is no longer with us.

To my aunt, my cousin and my girlfriend, who have always supported and helped me.

I also want to thank my roommates who have accompanied me in these 5 years of university and have also been my colleagues for this thesis project.

To all the people, whom I have not specifically mentioned, but who supported me and believed in me.

Thank you all.

Abstract

On October 5th, 2017, USA Administration announced the USA President plan to return astronauts to the Moon. Looking to the long-term, NASA and several other space agencies are also intent on establishing a permanent lunar base there. This base will not only provide opportunities for lunar science but will also facilitate missions to Mars and beyond.

The main question is, where should such a base be built? For many years, NASA, ESA and other agencies have been exploring the possibility of stable lava tubes as a potential site. According to new study by a team of international scientists, the presence of such a tube has now been confirmed in the Marius Hills region. This location is likely to be the site of future lunar missions and could even be the site of a future lunar habitat.

This study aims to achieve the preliminary design of a Lunar drone and its mission feasibility, focusing mainly on the problem of navigation. The main purpose is to explore the lunar caves and to provide pictures of them, all taking into consideration the use, if possible, of Italian technologies that have directed many of the choices in the system design made to the detriment of a purely theoretical treatment.

This thesis at first provides a purely theoretical overview of the systems used for autonomous navigation in an environment without GPS and in lack of lighting. Consequently, there is a discussion concerning the research for the components necessary for autonomous navigation. In particular, the two methods chosen: visual navigation and LiDAR, are then compared in terms of performance, masses, dimensions and energy consumption.

The autonomous navigation inside tunnels is finally treated by focusing on the problems of maximum speed and lighting. Always taking into consideration the comparison in terms of masses, dimensions, consumption and performance of the two architectures taken into account.

Finally, a discussion on the CAD of the individual components that will make up the drone is carried out in order to reach a possible configuration.

Index

Figures	8
Tables	11
Nomenclature	12
Applicable and reference documents	13
1 Context and objectives of the study	14
1.1 Mission statement and objectives.....	14
1.2 Observational evidence and characteristics of lunar lava tubes.....	15
1.3 State-of-the-art mission concepts	18
1.4 Challenges.....	18
1.5 Summary.....	19
1.6 Possibly supporting missions	19
2 LuNaDrone mission design	21
2.1 Mission overview	21
2.2 Spacecraft overview	25
3 Literature of the Navigation System	27
3.1 SLAM	27
3.2 Elements of vSLAM	28
3.2.1 Base Modules	28
3.2.2 Additional modules for stable and accurate vSLAM	28
3.2.3 Summary.....	29
3.3 Related Technologies.....	29
3.3.1 Visual odometry	29
3.3.2 Structure from motion	30
3.3.3 MonoSLAM	30
3.3.4 PTAM	30
3.3.5 Comparison between MonoSLAM and PTAM	31
3.3.6 Techniques on global map optimization	31
3.3.7 Summary.....	32
3.4 Direct methods	32
3.4.1 DTAM	32
3.4.2 LSD-SLAM.....	33
3.4.3 SVO and DSO	33
3.4.4 Summary.....	33
3.4.5 RGB-D vSLAM.....	34
3.4.6 KinectFusion	34
3.4.7 Slam ++	34
3.4.8 Techniques on RGB-D VO and global map optimization	34
3.5 Open problems	35

3.5.1	Pure rotation	35
3.5.2	Map initialization	35
3.5.3	Estimating intrinsic camera parameters.....	36
3.5.4	Rolling shutter distortion.....	36
3.5.5	Scale ambiguity.....	36
3.5.6	Benchmarking.....	36
3.6	Conclusion	38
3.7	LiDAR Based SLAM.....	39
3.8	Scan-Matching and Graph Optimization	40
3.8.1	Occupancy Map and Particle Filter.....	40
3.8.2	Loop Closure Refinement Step	40
3.9	LiDAR-Camera Fusion	41
3.9.1	The Mandatory Calibration Step	41
3.10	Visual-LiDAR SLAM.....	42
3.10.1	EKF Hybridized SLAM.....	42
3.10.2	Improved Visual SLAM.....	42
3.10.3	Improved LiDAR SLAM.....	43
3.10.4	Concurrent LiDAR-Visual SLAM	43
3.11	Summary.....	43
3.12	Conclusions.....	44
4	Navigation System - Design	46
4.1	Introduction.....	46
4.2	Mission plan.....	46
4.3	Hardware research	48
4.3.1	Cameras.....	48
4.3.2	IMU (Inertial measurement unit)	50
4.3.3	LED	51
4.3.4	LiDAR on Horizontal plane.....	52
4.3.5	LiDAR on Vertical plane	53
4.3.6	OBC	54
4.3.7	Laser distance sensor	55
4.4	Navigation - Option 1	56
4.5	Figures of merit	58
4.6	Starting altitude Limitation.....	59
4.6.1	Vision and Tilt limitation.....	59
4.6.2	Minimum pixel data error estimation	64
4.7	Vertical Speed Limitation	65
4.8	Navigation Option 2.....	67
4.9	Figures of Merits.....	69
4.10	Vertical Speed Limitation	70
4.11	Horizontal speed limitation	71
4.12	Mapping time required	72
4.13	Distance error estimation.....	73
4.14	Battery consideration	74

4.15	Comparison.....	75
4.16	Mission plan Power Consumption.....	76
5	Indoor Navigation – Preliminary evaluation	77
5.1	Visual Odometry.....	77
5.1.1	Configuration.....	77
5.1.2	Lightning.....	78
5.1.3	Figures of merit	79
5.1.4	Algorithm Speed consideration.....	81
5.1.5	Thrusters speed limitation.....	83
5.1.6	Power consumption	85
5.2	Led Heat dissipation	87
5.2.1	Conduction	87
5.2.2	Radiation.....	88
5.2.3	Thermal model	88
5.2.4	Thermal stack	89
5.2.5	Component.....	89
5.2.6	Thermal interface material.....	90
5.2.7	Heat sink.....	91
5.3	LiDAR.....	93
5.3.1	Configuration.....	93
5.3.2	Figures of Merits.....	94
5.3.3	Time Mapping.....	95
5.3.4	Speed consideration	97
5.4	Comparison LiDAR vs Visual Odometry.....	98
5.5	Custom Battery consideration.....	100
5.6	Pros and Cons	101
6	CAD.....	102
6.1	Introduction.....	102
6.2	Navigation System	102
6.2.1	Camera.....	102
6.2.2	IMU	103
6.2.3	LED.....	104
6.2.4	LiDAR Horizontal plane.....	105
6.2.5	LiDAR Vertical Plane	106
6.3	OBC.....	107
6.4	EPS	108
6.4.1	Battery	108
6.5	Propulsion.....	109
6.5.1	Main Thruster	109
6.5.2	Reaction control system.....	111
6.5.3	Valves.....	112

6.5.4	Propellant Tank.....	114
6.5.5	Pressurant Tank.....	115
6.6	Structure.....	116
6.6.1	Configuration 10x20x60	116
6.6.2	Configuration 20x20x30	117
7	Conclusions and recommendations	123
8	References	125

Figures

Figure 1 Potential entrance outcomes from observed pits and rilles	16
Figure 2 [138] (A, B) Mare Tranquillitatis Pit in two near nadir images with opposite Sun azimuth angles, both images are approximately 175 m wide. Oblique views: (C) layering in west wall and a portion of pit floor beneath overhanging mare (29° ema); (D) A significant portion of the illuminated area is beneath the eastern over hanging mare in this image (26° ema), white arrow indicates same boulder marked with black arrow in B. Detailed layering is revealed in (E) and (F). Outcropping bedrock layer thickness estimates are presented in (F) in metres, ±1m	17
Figure 3 These images from NASA's LRO spacecraft show all of the known mare pits and highland pits. Each image is 222 metres wide. [139]	17
Figure 4 Illustation of the flight segment	21
Figure 5 Brainstorming on the possible scenarios of the mission.....	23
Figure 6 On the left the bottom view, on the right the top view of LuNaDrone	25
Figure 7 The two-sided view of LuNaDrone	26
Figure 8 Part numbers	26
Figure 9 Principle of the ICP algorithm. At each iteration, the closest points are extracted between the two scans. From these matches, a transformation is processed and applied on the second scan. Then, the process iterates until a given cost criterion is reached.....	39
Figure 10 Summary of LiDAR based SLAM's advantages and drawbacks.....	41
Figure 11 Different ways of implementing visual-LiDAR SLAM.	44
Figure 12 Mission plan.....	47
Figure 13 ImperX 5 MP CMOS Camera C2420 [141].	48
Figure 14 OBC design.....	54
Figure 15 Laser measurement distance sensor	55
Figure 16 Power, Mass, Size comparison in configuration 1	58
Figure 17 Geometric representation of drone-crater angles.....	59
Figure 18 Deformation of the circle as a function of elevation and distance from the crater.	60
Figure 19 Drone tilt, depending on the height above the ground, during the first rotation in order to accelerate, assuming a distance from the crater of 200m.....	61
Figure 20 Drone tilt, depending on the distance from the crater, during the second rotation in order to decelerate and approach the crater, assuming a height from the ground of 30m.	62
Figure 21 Limitation on the minimum necessary flight height after the initial inclination as a function of the distance from the crater in order to maintain visibility.	62
Figure 22 Limitation on the minimum necessary distance from the crater after the final inclination as a function of the height from the ground in order to maintain visibility of the crater.	63
Figure 23 Comparison Focal lens size as a function of the distance from the lens.....	64
Figure 24 Comparison between the two resolutions as a function of the distance from the crater.	64
Figure 25 Max Vertical Speed according to the configuration 1	65
Figure 26 Power, Mass, Size comparison in configuration 1	69
Figure 27 Max Vertical Speed according to the configuration 2	70
Figure 28 Max Horizontal Speed according to the configuration 2	72
Figure 29 Time required to map while using LiDAR.....	72
Figure 30 Comparison between HFOV and VFOV of the LiDAR scanning area.....	73
Figure 31 LiDAR scan coverage area as a function of distance from walls	73
Figure 32 Comparison between the masses and the dimensions of the custom batteries needed to power the navigation system in the two configurations.	74
Figure 33 Comparison of mass, power, dimensions between the two configurations	75
Figure 34 Power budget of the navigation system	76
Figure 35 Lux generated with an 80W LED depending on the distance from the walls	79
Figure 36 Comparison between the required sizes of the different configurations according to the number of cameras and the distance from the walls.....	79

Figure 37 Comparison between the required masses of the different configurations according to the number of cameras and the distance from the walls.	80
Figure 38 Comparison between the required powers of the different configurations according to the number of cameras and the distance from the walls.	80
Figure 39 Representation of the aperture cone of visibility in 3D space [140].....	81
Figure 40 Maximum speed according to the refresh rate with a distance from the walls set at 10m.....	82
Figure 41 Maximum speed as a function of distance with a refresh rate set at 15Hz.	82
Figure 42 Maximum speed allowed for navigation in caves according to the distance from the walls, with 1N of thrust provided by the auxiliary engines.	84
Figure 43 Maximum speed allowed for cave navigation according to the distance from the walls, with 30N of thrust provided by the auxiliary engines.	84
Figure 44 Graphing of the energy consumption levels due to the various components necessary for navigation in this configuration.....	85
Figure 45 Graphic representation of the Duty Cycle, assuming a refresh rate of 10Hz, of the LEDs and the camera considering the minimum ignition times of the respective components previously analyzed.	85
Figure 46 Representation of the energy consumption as a function of the refresh rate using the DC technique, withstanding a distance from the walls set at 10m.	86
Figure 47 Comparison between the energy consumption of the configuration with DC and the one without.	86
Figure 48 Thermal circuit of an LED array	88
Figure 49 Time required for mapping as a function of the rotation speed of the LiDAR laser sensor. Assuming fixed 1 ° of step as precision in vertical scanning.	95
Figure 50 Time required for mapping as a function of accuracy in vertical resolution Assuming a rotation speed of the laser sensor of the LiDAR of 20Hz.....	95
Figure 51 Points per second scanned by LiDAR as a function of rotation speed, assuming a resolution on the horizontal plane of 0.1°.	96
Figure 52 Graph representing the minimum accuracy of object detection as a function of the distance from the walls to be analyzed. The comparison is made considering 5 different levels of vertical resolution.	96
Figure 53 Maximum speed allowed for navigation in caves according to the distance from the walls, with 50N of thrust provided by rotation of the main motor.	97
Figure 54 Size comparison between LiDAR configuration and visual navigation configuration with various cameras.	98
Figure 55 Mass comparison between LiDAR configuration and visual navigation configuration with various cameras.	98
Figure 56 Power consumption comparison between LiDAR configuration and visual navigation configuration with various cameras.....	99
Figure 57 Comparison of the dimensions between LiDAR technology and visual navigation as the number of cameras varies, taking into account the relative sizes of the batteries needed to power it.	100
Figure 58 Comparison of masses between LiDAR technology and visual navigation as the number of cameras varies, taking into account the relative masses of the batteries needed to power it.	100
Figure 59 Front view of camera and ImperX lens [annex AD_17].	102
Figure 60 Rear view of camera and ImperX lens.	103
Figure 61 Front view IMU, the rear view is omitted as before of significance [annex AD_18]	103
Figure 62 Front view of the LED [annex AD_19].....	104
Figure 63 Front view of LED optics with 60 ° FOV [annex AD_20].....	104
Figure 64 Front view of the LiDAR which deals with mapping at 360 ° on the horizontal plane [annex AD_21]	105
Figure 65 Front view of the LiDAR which takes care of mapping the ground and estimating the height [annex AD_22].....	106
Figure 66 Rear view of the LiDAR which takes care of mapping the ground and estimating the height	106
Figure 67 OBC front view	107
Figure 68 OBC rear view	107
Figure 69 Battery pack with connectors in the 6x1 configuration [annex AD_15].....	108
Figure 70 Battery pack with connectors in 3x2 configuration [annex AD_16]	108

Figure 71 50 N thruster front view [annex AD_26].....	109
Figure 72 100 N thruster front view [annex AD_28].....	110
Figure 73 75 N thruster front view [annex AD_27].....	110
Figure 74 Front view of the 1N thruster necessary for the attitude control of the drone [annex AD_24]	111
Figure 75 Front view of the 5N thruster necessary for the attitude control of the drone [annex AD_25]	112
Figure 76 Front view of a LEE IEP solenoid valve used for trim control thrusters [annex AD_33].....	112
Figure 77 Front view of a pintle [annex AD_35]	113
Figure 78 Front view of a Latch valve [annex AD_34]	113
Figure 79 Front view of a check valve [annex AD_36].....	113
Figure 80 Front view of a Filter [annex AD_37]	114
Figure 81 Front view of the propellant tank	114
Figure 82 Upper view of the propellant tank.....	115
Figure 83 Front view of the pressurizing tank	115
Figure 84 Front view of the assembly in the 10x20x60 configuration.....	116
Figure 85 Side view of the drone assembly with structure and components.	117
Figure 86 Side view of the drone assembly with structure and components.	118
Figure 87 Top view of drone with structure.....	119
Figure 88 Bottom view of drone with structure.....	119
Figure 89 Side view of the drone assembly considering only the components, without structure.	120
Figure 90 Side view of the drone assembly considering only the components, without structure.....	121
Figure 91 Top view of the drone without structure	122
Figure 92 Bottom view of the drone without structure	122

Tables

Table 1 <i>High resolution imaging confirms existence of cavernous lunar sub-surfaces</i> [137].....	15
Table 2 <i>Mission requirements</i>	22
Table 3 <i>Mission contingencies [annex AD_01]</i>	24
Table 4 <i>Main characteristics of the current configuration of the spacecraft</i>	25
Table 5 <i>Comparison of representative algorithms</i> [91].....	38
Table 6 <i>Comparison of various space qualified COTs cameras [annex AD_05]</i>	48
Table 7 <i>Data sheet ImperX 5 MP CMOS Camera C2420</i> [141].	49
Table 8 <i>Data Sheet IMU</i> [127]	50
Table 9 <i>Comparison of various COTs LEDs [annex AD_03]</i>	51
Table 10 <i>Data Sheet LED</i> [128]	51
Table 11 <i>Comparison of various COTs LiDAR [annex AD_08]</i>	52
Table 12 <i>Data Sheet LiDAR 360°</i> [129]	52
Table 13 <i>Data Sheet LiDAR limited FOV</i> [130]	53
Table 14 <i>Data Sheet OBC</i> [131]	54
Table 15 <i>Data Sheet Laser Distance sensor</i>	55
Table 16 <i>System features considering the configuration 1</i>	58
Table 17 <i>Speed Limitation according to configuration 1</i>	65
Table 18 <i>System features considering the configuration 2 [annex AD_10]</i>	69
Table 19 <i>Vertical Speed Limitation according to configuration 2</i>	70
Table 20 <i>Horizontal Speed Limitation according to configuration 2</i>	71
Table 21 <i>Description of the various phases of the mission with the times and energy consumption inherent to the navigation system</i>	76
Table 22 <i>Lighting levels of various environments</i> [134]	78
Table 23 <i>Summary table of parameters used to estimate speed limits in the configuration with visual navigation</i>	83
Table 24 <i>Relative properties of TIMs, advantages and disadvantages</i>	90
Table 25 <i>Thermal conductivity and emissivity for various materials at 25°C</i>	91
Table 26 <i>Heat sink manufacturing process comparison</i>	92
Table 27 <i>System features considering the LiDAR configuration with laser distance sensor [annex AD_11]</i> ..	94
Table 28 <i>Power, Mass, Size comparison considering the LiDAR configuration with laser distance sensor</i>	94
Table 29 <i>Summary table of parameters used to estimate speed limits in the configuration with LiDAR</i>	97
Table 30 <i>Summary table of the parameters obtained considering the batteries to power the navigation system</i>	100

Nomenclature

<i>Acronym</i>	<i>Description</i>
<i>SLAM</i>	Simultaneous localization and mapping
<i>vSLAM</i>	Visual simultaneous localization and mapping
<i>AR system</i>	Augmented reality system, is a combination of real and virtual worlds, real-time interaction, and accurate 3D registration of virtual and real objects
<i>BA</i>	Bundle Adjustment
<i>TAM</i>	Tracking and mapping
<i>PTAM</i>	Parallel Tracking and Mapping
<i>VO</i>	Visual Odometry
<i>Sfm</i>	Structure from motion
<i>MonoSLAM</i>	MonoSLAM: monocular vSLAM
<i>EKF</i>	Extended Kalman filter
<i>LSD SLAM</i>	Large-Scale Direct Monocular simultaneous localization and mapping
<i>IR</i>	Infrared
<i>PEVO</i>	Projection error of virtual object
<i>PRE</i>	Relative pose error
<i>ATE</i>	Absolute trajectory error
<i>NDT</i>	Normal Distributions Transform
<i>CNN</i>	Convolutional Neural Networks

Applicable and reference documents

Applicable documents:

<i>AD_01</i>	<i>Mission contingencies</i>
<i>AD_02</i>	<i>Bell point calculation</i>
<i>AD_03</i>	<i>Navigation Table_LED</i>
<i>AD_04</i>	<i>Navigation Table_Heat Sink</i>
<i>AD_05</i>	<i>Navigation Table_Camera</i>
<i>AD_06</i>	<i>Navigation Table_IMU</i>
<i>AD_07</i>	<i>Navigation Table_Laser sensor</i>
<i>AD_08</i>	<i>Navigation Table_LiDAR</i>
<i>AD_09</i>	<i>Navigation Table_OBC</i>
<i>AD_10</i>	<i>Navigation Table_Navigation</i>
<i>AD_11</i>	<i>Navigation Table_Indoor Navigation</i>
<i>AD_12</i>	<i>Navigation Table_Heat dissipation</i>
<i>AD_13</i>	<i>Navigation Table_Camera resolution</i>
<i>AD_14</i>	<i>Navigation Table_Battery consideration</i>
<i>AD_15</i>	<i>CAD_EPS_battery 6x1</i>
<i>AD_16</i>	<i>CAD_EPS_battery 3x1</i>
<i>AD_17</i>	<i>CAD_Navigation_Camera</i>
<i>AD_18</i>	<i>CAD_Navigation_IMU</i>
<i>AD_19</i>	<i>CAD_Navigation_LED</i>
<i>AD_20</i>	<i>CAD_Navigation_LED optics</i>
<i>AD_21</i>	<i>CAD_Navigation_LiDAR xy</i>
<i>AD_22</i>	<i>CAD_Navigation_LiDAR z</i>
<i>AD_23</i>	<i>CAD_Navigation_OBC</i>
<i>AD_24</i>	<i>CAD_Propulsion_Thruster 1N</i>
<i>AD_25</i>	<i>CAD_Propulsion_Thruster 5N</i>
<i>AD_26</i>	<i>CAD_Propulsion_Thruster 50N</i>
<i>AD_27</i>	<i>CAD_Propulsion_Thruster 75N</i>
<i>AD_28</i>	<i>CAD_Propulsion_Thruster 100N</i>
<i>AD_29</i>	<i>CAD_Propulsion_Tank</i>
<i>AD_30</i>	<i>CAD_Propulsion_Pressurizing tank</i>
<i>AD_31</i>	<i>CAD_Structure 10x20x60</i>
<i>AD_32</i>	<i>CAD_Structure 20x20x30</i>
<i>AD_33</i>	<i>CAD_Propulsion_Solenoid Valve</i>
<i>AD_34</i>	<i>CAD_Propulsion_Latch_OX</i>
<i>AD_35</i>	<i>CAD_Propulsion_Pintle</i>
<i>AD_36</i>	<i>CAD_Propulsion_Check valve</i>
<i>AD_37</i>	<i>CAD_Propulsion_Filter</i>

1 Context and objectives of the study

1.1 Mission statement and objectives

Mission statement:

“To design a flying drone able to autonomously hover inside a lava tube entering a skylight, taking photos and mapping the internal surface. The concept of the drone is based on the strategic idea already experienced with Cubesats: small spacecraft, low mass and cost, standardized, affordable by Academies and SME’s and easy to deliver in Space”

The primary and secondary objectives of the mission have been deduced from the mission statement and are:

Primary objectives:

- To design an autonomously flying drone
- To explore and photograph lava tubes

Secondary objectives:

- To map the interior of lava tubes
- To develop a low cost and low mass drone concept to be standardize

1.2 Observational evidence and characteristics of lunar lava tubes

The chance for the actual existence of lunar lava tubes was postulated during the early 1960's. In 1971, a study concerning the possible presence of lava tubes in the Marius Hills region was published, with the evidence of rilles on the surface [1].

In 2009, the 10 m-resolution images taken by the Terrain Camera (TC) aboard SELENE (nicknamed Kaguya) showed three huge vertical holes in the lunar Marius Hills, Mare Tranquillitatis and Mare Ingenii. The holes have aperture diameters and depths of several tens of metres to one hundred metres [2]. Haruyama et al. (2009) [3] hypothesized that they are possible “skylights” opened on subsurface caverns such as lava tubes.

In 2010, NASA's Lunar Reconnaissance Orbiter (LRO) photographed the skylight in the Marius Hills in more detail, showing both the 65-metre-wide pit and the floor of the pit about 36 metres below [4]. The LRO has also imaged over 200 pits that show the signature of being skylights into subsurface voids or caverns, ranging in diameter from about 5 m (16 ft) to more than 900 m (3,000 ft), although some of these are likely to be *post-flow features* rather than volcanic skylights [5]. Figure 3 shows some examples.

In 2011, NASA launched GRAIL, whose purpose was to evaluate the gravity field of the Moon in order to detect its internal structure. It also made it possible to confirm the presence of lava tubes underneath the surface. To this purpose, a skylight of 65 metres in diameter and 80-85 metres deep, with a roof thickness of 20-25 metres has been proven to exist. It is located in the Marius Hills region and occurs in a shallow rille-like trough about 400 metres wide and 300-400 metres deep. It is expected to hide a large cavern beneath the visible surface that extends about 60 km to the west of the skylight, where the cavern itself is approximately 30 km in length [6].

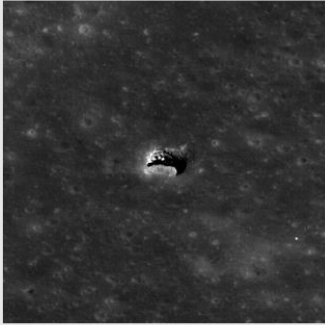
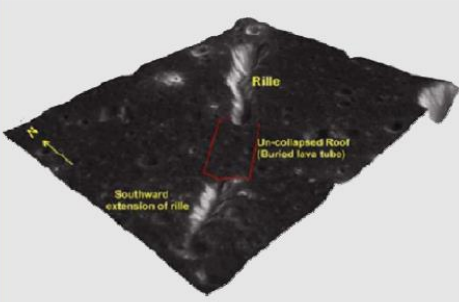
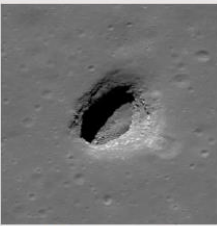
Recently Discovered Lunar Pits and Tubes	
 <p>Marius Hills Skylight</p> <ul style="list-style-type: none"> • 14.09 deg. N. 303.31 deg. E. • 45 m deep • 48 m to 57 m diameter 	 <p>Chadrayaan-1 Lava Tube</p> <ul style="list-style-type: none"> • North of Rima Galilaie, region of Oceanus Procellarum • 1.72 km length (un-collapsed section) • Tube diameter estimated at 120 m (Rille depth is ~85 m)
 <p>Mare Ingenii Pit</p> <ul style="list-style-type: none"> • 35.95 deg. S. 166.06 deg. E. (Far Side) • 101 m x 66 m wide with a depth of ~60 m • SSE side of pit wall slopes ~45 deg. 	 <p>Mare Tranquillitatis Pit</p> <ul style="list-style-type: none"> • 8.34 deg. N. 33.22 deg. E. • 84 m to 99 m diameter • 107 m deep

Table 1 High resolution imaging confirms existence of cavernous lunar sub-surfaces [137]

Again in 2011, a study conducted on Chandrayaan-1's observations, an Indian lunar spacecraft, showed a buried, un-collapsed and near horizontal lava tube in the vicinity of Rima Galilaei [7].

A remnant of the volcanic tube, whose roof has capsized and created a valley is named a "rille". It may happen that the roofs of such tubes do not collapse and remain intact, with a hollow interior in most cases. A skylight is a lava tube ceiling collapse potentially providing a means of entrance into the tunnel. Figure 1 illustrates typical entrance possibilities which may be encountered for the pits and tubes identified in Table 1. More details about Mare Tranquillitatis Pit are reported in Figure 2.

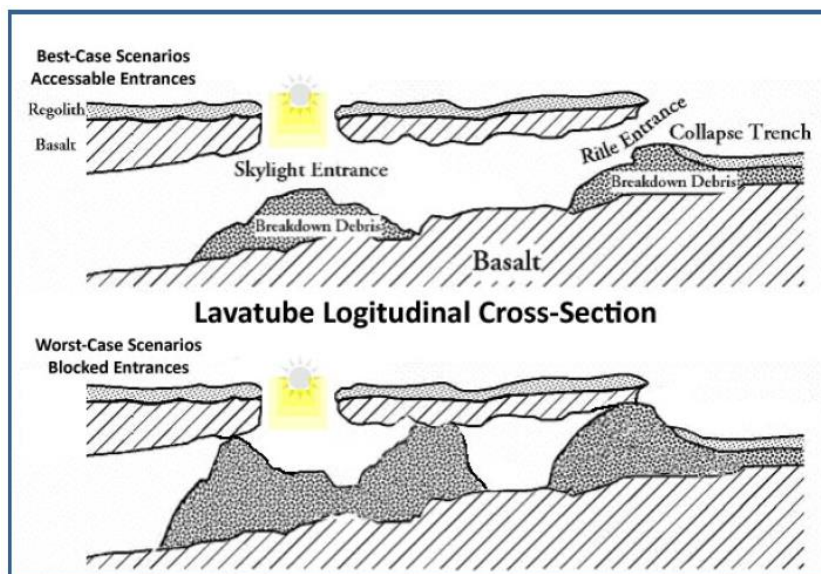


Figure 1 Potential entrance outcomes from observed pits and rilles

To map the distribution and age of bedrock at the surface, investigations for understanding the geological processes associated with ancient lunar basaltic lava flows are still needed.

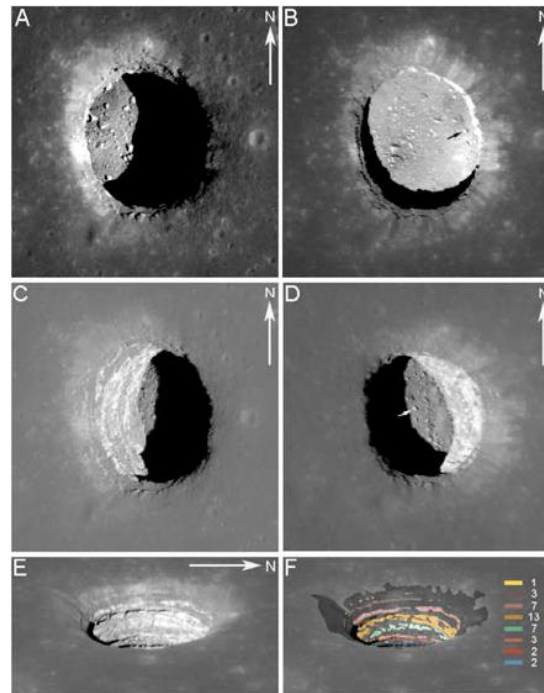


Figure 2 [138] (A, B) Mare Tranquillitatis Pit in two near nadir images with opposite Sun azimuth angles, both images are approximately 175 m wide. Oblique views: (C) layering in west wall and a portion of pit floor beneath overhanging mare (29° ema); (D) A significant portion of the illuminated area is beneath the eastern overhanging mare in this image (26° ema), white arrow indicates same boulder marked with black arrow in B. Detailed layering is revealed in (E) and (F). Outcropping bedrock layer thickness estimates are presented in (F) in metres, $\pm 1m$

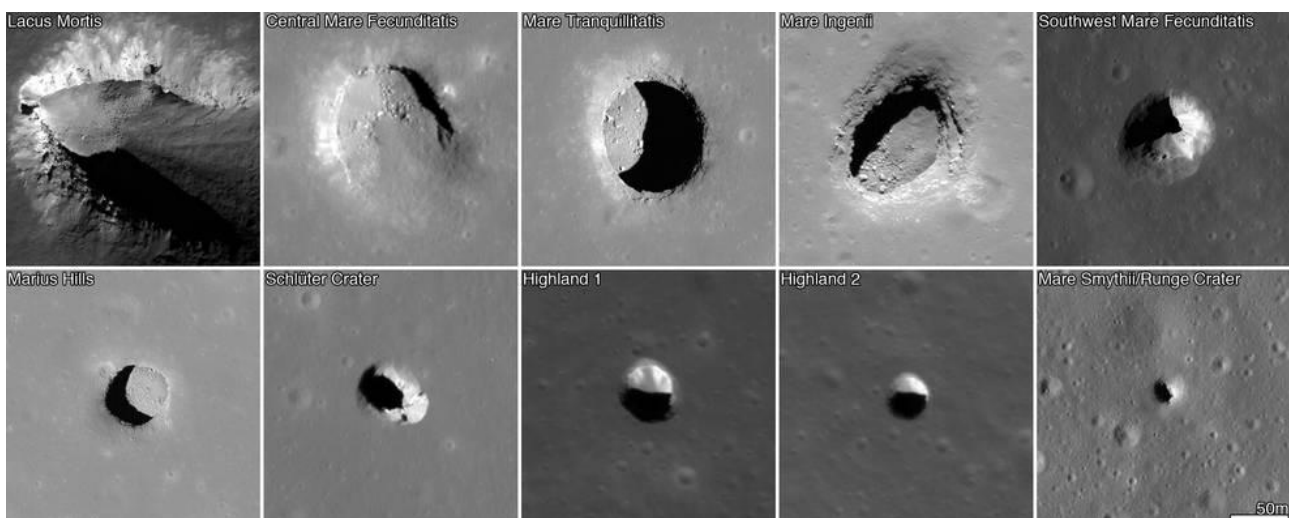


Figure 3 These images from NASA's LRO spacecraft show all of the known mare pits and highland pits. Each image is 222 metres wide. [139]

Lava tubes tend to have smooth floors, with possible “soda straws” stalactites formed by lava dipping from the ceiling. Due to the lesser gravity, lava tubes on the Moon may be much larger in diameter than those found on Earth [8]. These caverns would be suitable for human habitation, because they could provide safety

from hazardous radiations, micro-meteoritic impacts, extreme temperatures and dust. However, polar regions are interesting as well, because they appear to have abundant ice water. According to a new discovery presented at NASA's Lunar Science for Landed Missions Workshop, it appears that there is a location on the Moon that merges both aspects: a possible lava tube that is located in the northern polar region (Philolaus Crater) [9].

For what concerns radiation protection, the thickness of the roof of the caves is expected to be tens of metres [7], that would certainly be advantageous, but, on the other hand, it would represent an obstacle for the design of a communication system between the inside of these caves and the surface.

On the surface of the Moon the fluctuations of the temperature are extremely wide, whereas the interior of the caves is expected to maintain an almost constant temperature around -20°C . As a result, this aspect would greatly ease the design of the thermal control system of all those devices that would operate in this environment.

1.3 State-of-the-art mission concepts

Mission architecture usually includes the number of robotic entities and their roles (i.e. probes, landers...), their approximate mass (which has implications on the traditional space mission architecture components of launch vehicle and trajectory), the methods of communication, the power strategies employed, and the concept of operations. Multi-mission architectures are also possibilities for skylight and cave exploration. One such multi-mission architecture would be broken into three phases, the first phase being the flyover and surface investigation of a skylight and deployment of a sensor package to a skylight entrance. The second phase could send mobile robots in to explore lava tubes or cave network. The third phase could include deliver of habitats, robots and personnel with specialized scientific instruments. A reference set of mission goals can be defined in order to compare mission architectures. Those goals are to enter a lava tube cave via skylight, to explore it and to send data [8].

1.4 Challenges

From several tests on Earth, it is known that ground penetrating radar often fails to detect lava tubes especially if the lava was deposited in multiple flows. This is because of the partial reflection of the radar at interfaces between layers of material, caused by repeated lava flows.

From a scientific perspective, in many cases it may be sufficient to get beyond the "twilight zone" (the transition between areas illuminated for some period during the day and areas of constant darkness) to define the distance to be travelled inside a cave. This region is likely to be indicative of the variation of different significative parametres, such as potential to support life, volatile contents and geological features, impacted by sunlight, temperature variations or rock fall during skylight formation.

Moreover, some scientists believe that using propulsive vehicles may lead to possible problems, such as the contamination of volatiles trapped at the bottom of a skylight or even the death of living organisms inside a cave. Additionally, there may be the possibility of contaminating scientifically important sites with that strategy.

The main issues to cope for planetary cave exploration are:

- access to the cave
- in-cave mobility
- data collection and processing
- power sources
- communication

Spacecraft configuration has a large impact on how these issues have to be managed. As an example, the lack of solar power underground may put large limitations on how the spacecraft could move. Energetically, it does not make sense to carry the propulsion system required for landing along for further cave explorations activities. Tethered solutions may also be considered.

Note that modelling in lava tubes requires active sensing and due to the expected larger size of lava tubes on the Moon, sensors in this environment must have long range, which requires increased power. To this purpose, technologies like active sensing could provide a physical barrier to miniaturization [8].

1.5 Summary

Hybrid propulsive configurations may be considered. External tethered lighting or power source systems may be considered. Wireless power and data transmission within line of sight of the tethered communication node would eliminate the need for exploration robot to physically reach it, which is critical in unpredictable environments. Combination of active sensing (good for shadowed regions but lower resolution and range limited by power) and cameras (higher resolution but unable to determine 3D scale) required to build sufficiently detailed models for science and robot operations. Commercial magneto-inductive communications system indicates an achievable data rate of 2412bps through rock. Magneto-inductive comm requires a large and heavy antenna. While it is a great technology for later use in cave operations, it may not be feasible for the first, lightweight robotic explorers [8].

For what concerns power and communication, extended periods without access to solar power, limited accessibility to communication and operating exclusively in a dark environment have to be taken into account. High energy density batteries would enable longer cave excursions with low battery masses [8]. Limited data link through rock can be achieved with very low-frequency radio or magneto-inductive comm. These technologies are under development terrestrially for cave and mining communication and rescue and have undergone significant advances in mass and power requirements over the past few years [8].

1.6 Possibly supporting missions

Moon exploration will gain more and more interest in the next few years. To this purpose, many different companies are developing new landers and rovers to be launched. The study in this document is based on the idea that LuNaDrone will have to be carried to the proximity of an above-mentioned skylight by one of them. For instance, JAXA's lander named SLIM (Smart Lander for Investigating Moon), whose departure is planned for January 2022, will land in the vicinity of Marius Hills Hole, with an accuracy of about 100 metres, next to a lava tube [10].

For instance, it would be reasonable to take into consideration NASA's CLPS (Commercial Lunar Payload Services), an initiative which allows rapid acquisition of lunar delivery services from American companies for payloads that advance capabilities for science, exploration or commercial development of the Moon. Investigations and demonstrations launched on commercial Moon flights will help the agency study Earth's nearest neighbour under the Artemis program. Moreover, NASA has identified agencies and external science payloads that will fly on future CLPS missions, including the Volatiles Investigating Polar Exploration Rover (VIPER). Future payloads could include other rovers, power sources, and science experiments, including the technology demonstrations to be infused into the Artemis program [11]. NASA has chosen Astrobotic, Intuitive Machine and Masten to take part to CLPS programme.

Hakuto-R is the program name for iSpace's first two lunar missions, a commercial initiative with the purpose to demonstrate the capability to softly land and release a rover. It will lead to various subsequent high-frequency, cost-effective missions to establish a payload delivery system to the Moon [12].

2 LuNaDrone mission design

2.1 Mission overview

The mission concept is based on the assumption that a lander and/or a rover would deploy LuNaDrone in the proximity of a selected skylight, at a maximum distance of TBD metres from the waypoint from which the vertical descent phase will start. That distance shall be laterly in subsequent iterations decided according to the physical dimensions of the crater to be explored and the performances/architecture of the spacecraft.

After the deployment, LuNaDrone shall be able to conduct at least one autonomous flight. It consists of different phases: take off, climb, hover, horizontally translate to reach the skylight, descend into the lunar pit and come back to the initial point following the same trajectory.

Because landing hazard avoidance was not prioritized, the flight will start and end within an area to be pre-inspected and determined to be safe in terms of obstacles and ground slope.

While hovering, LuNaDrone has to be able to deal with disturbance of the flight and maintain its stability. In addition, a plan about when and how to implement the acquisition of the images has to be carefully developed. During the acquisition, LuNaDrone would need to enlighten the subject.

LuNaDrone has to be able to either store and/or forward the images to the rover/lander.

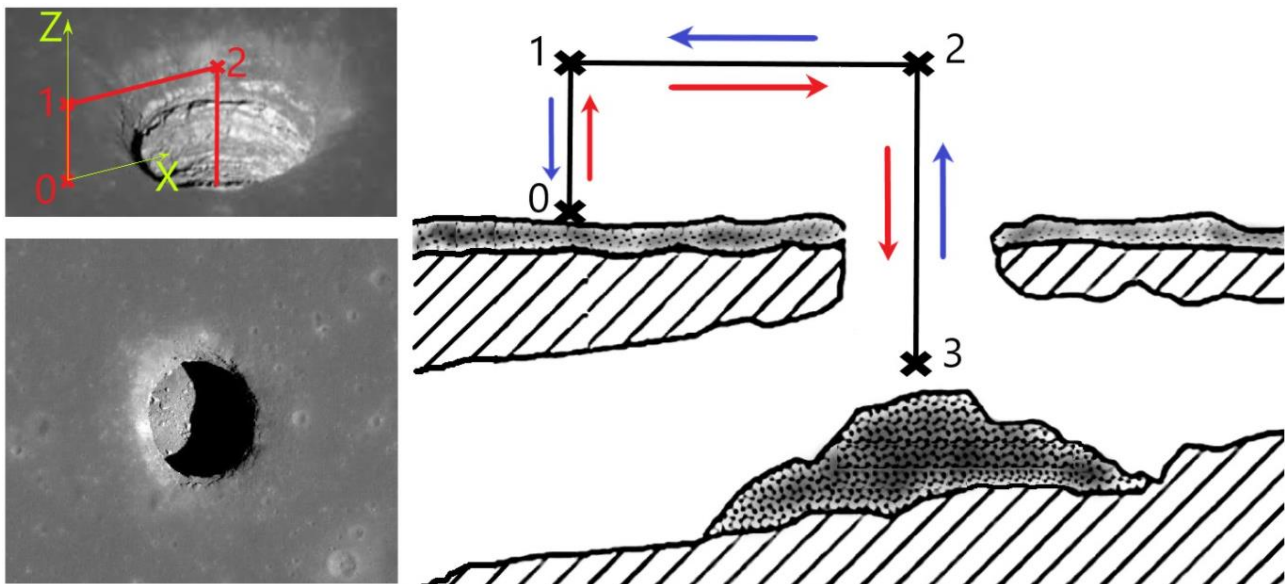


Figure 4 Illustration of the flight segment

A possible flight of the LuNaDrone might be the one shown in Figure 4. The first step, identified by the numbers 0-1, refers to a vertical ascent manoeuvre in which the spacecraft rises from the lunar surface and reaches a predetermined altitude. It will then follow the horizontal translation manoeuvre, where the spacecraft will cover a certain distance along the X-axis without changing its altitude. The last manoeuvre, identified by the numbers 2-3, refers to the descent segment where the spacecraft will decrease its altitude

until it stops at point 3. It is assumed that the LuNaDrone will reach points 1, 2 and 3 with zero residual velocity and, if required, it will have to hover at these points for a predetermined time frame before moving on to the next flight segment. After acquiring the photos of the inside of the lunar pit, LuNaDrone will have to come back to the initial point, following the same trajectory.

Code	Functional and Performance Requirements
R1	The LuNaDrone shall be able to autonomously depart from the surface of a rover, hover, enter in a target Lunar Cave and exit at the end of the mission returning to the rover (TBC)
R2	The LuNaDrone shall be equipped with a propulsion system able to support the entire mission
R3	The LuNaDrone shall be able to withstand a travel time of at least TBC min
R4	The LuNaDrone shall be able to withstand a travel distance of at least TBC Km
R5	The LuNaDrone shall be able to take images of the Cave, store them on-board and transmit them to the Rover and/or Lander at the end of the mission or as soon as possible (TBC)
R6	The LuNaDrone wet mass shall be less than 15 Kg (TBC)
R7	The volume of the LuNaDrone shall be less than 30 X 20 X 20 (TBC) cm while in stowage at the ROVER
Interface Requirements	
R8	The LuNaDrone vehicle shall be able to autonomously depart from the surface of a rover, hover and return to its base on top of the rover.
	Environmental Requirements
R9	The LuNaDrone shall be able to withstand environment (day/night) of the Moon site and Moon Cave (TBC)
R10	The LuNaDrone shall be able to withstand the launch and transport to the Moon environment in stowed conditions (TBC)
Operational Requirements	
R11	The LuNaDrone shall be able to take pictures in visual wavelengths (TBC).
R12	The LuNaDrone shall be able to fly autonomously by means of a pre-programmed flight sequence
Implementation requirements	
R13	The LuNaDrone shall make use of non-toxic propellants that are safe to handle on ground
R14	The LuNaDrone functional simulator shall be able to show the vehicle functional architecture and simulate the mission
R15	The LuNaDrone 3D-printed scaled model shall be able to show the vehicle physical architecture and the technology critical components

Table 2 *Mission requirements*

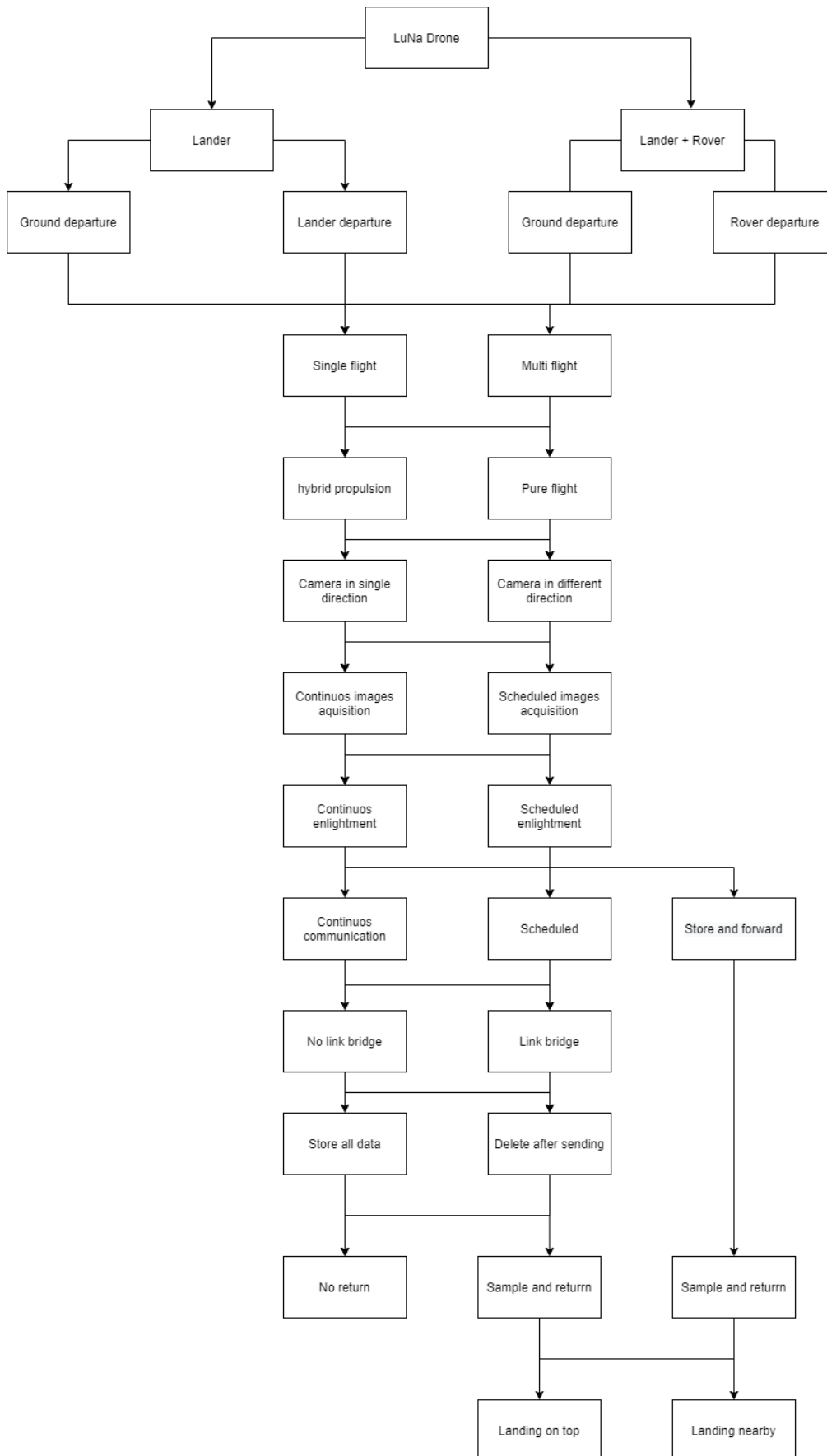


Figure 5 Brainstorming on the possible scenarios of the mission



ID	Subject	Mission contingencies
MC-001	Lander Lander + rover	The lander must land no more than TBD meters from the skylight. The rover must be able to approach at least TBD meters from the skylight.
MC-002	Ground departure Rover/Lander departure	The LuNaDrone will first be released to the lunar surface and then take off. The LuNaDrone will take off directly from the lander/rover
MC-003	Continuous communication Scheduled communication Store and forward	The LuNaDrone must be able to communicate continuously. The LuNaDrone has to communicate only when necessary The LuNaDrone will communicate mission data once it emerges from the lava tube.
MC-004	Sample and return No return	The LuNaDrone will be able to return to the lander/rover. The LuNaDrone will not necessarily be able to return to the lander/rover.
MC-005	Flight Hybrid propulsion	The LuNaDrone must be able to explore the hole by flying. In addition to flying, the LuNaDrone must be able to move on the surface with a more efficient propulsion.
MC-006	Landing on top of the lander/rover Landing nearby	The LuNaDrone must be able to land on top of the lander/rover. The LuNaDrone must be able to land at a maximum distance of TBD meters from the lander/rover.
MC-007	NO link bridge Link bridge TBD	The LuNaDrone shall be able to communicate without LOS through the rocks The LuNaDrone shall be able to communicate in LOS with a TBD link bridge
MC-008	Camera/cameras in single direction Camera/cameras in different directions	The LuNaDrone shall be able to take images only towards its movement The LuNaDrone shall be able to take images in all/different directions
MC-009	Single flight approach Multi-phase flight approach	The LuNaDrone shall depart only once, do its operations and land only once. The LuNaDrone shall depart and land TBD times, with scheduled and programmed acquisition plan.
MC-010	Store all data Delete stored data after sending	The LuNaDrone shall be equipped with sufficient memory to save all the mission data The LuNaDrone shall not preserve data after sending
MC-011	Continuous images acquisition Scheduled images acquisition	The LuNaDrone shall continuously use cameras The LuNaDrone shall use cameras following a predicted plan
MC-012	Continuous enlightenment Scheduled enlightenment	The LuNaDrone shall continuously enlight its way for the cameras The LuNaDrone shall enlight following cameras needs

Table 3 Mission contingencies [annex AD_01]

2.2 Spacecraft overview

The main objective of the mission is to acquire images of the inside of lava tubes on the Moon. To this purpose, the system of cameras which will be designed and utilized is of fundamental importance. In particular, the number of cameras, their resolution and their positioning will have to be discussed in order to find the best solution in terms of mass, volume and compatibility with the other subsystems. The propulsion system includes one hydrogen peroxide monopropellant rocket as main engine and at least other eight for the ACS. The spacecraft will obtain its necessary electrical power from lithium primary batteries. The above-mentioned subsystems are strongly linked to the flight profile development, which can state how efficient a manoeuvre is and the angle of inclination of the spacecraft for its movements, which in turn gives information again to the navigation and propulsion systems design.

<i>Subsystem/object</i>	<i>Type</i>
<i>Navigation</i>	IMU+Visual Navigation, IMU+LiDARs
<i>Image acquisition</i>	one 12 Mpx camera, 120° FOV, 15 fps
<i>Propulsion</i>	Hydrogen peroxide 92% wt monopropellant rockets
<i>Electrical power source</i>	Primary batteries
<i>CommSys</i>	X-band 8 GHz, 40-50 Mbit/s

Table 4 Main characteristics of the current configuration of the spacecraft

The drafting of Chapter 1 and Chapter 2 was carried out in collaboration with two colleagues from Politecnico di Torino: Stefano Pescaglia [13] and Gabriele Podestà [14], who were respectively responsible for developing the flight profile (as well as identifying possible electrical power sources), and studying the propulsion system of spacecraft.

Here below some images of the actual configuration are presented. They do not represent a complete spacecraft and no detailed analysis for the compatibility of the subsystems have been carried out. The purpose of these images is to give a rough idea of how the room inside the spacecraft may be utilised, considering the requirements of the different components (e.g. the necessity of the LiDARs to have nothing to hinder their view).

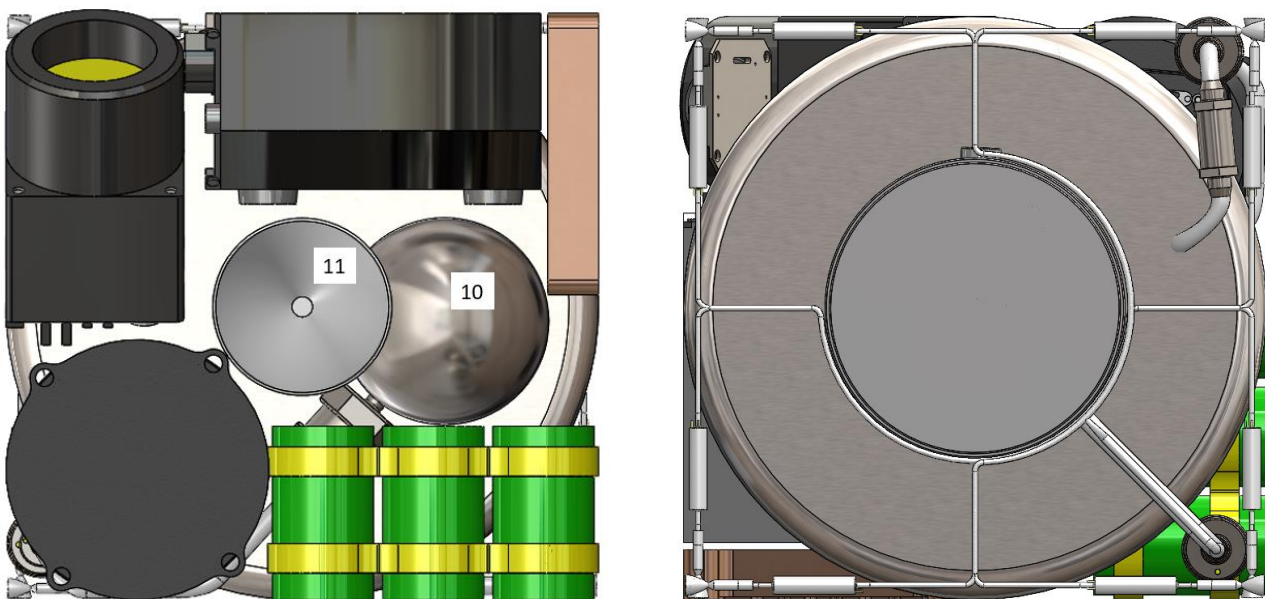


Figure 6 On the left the bottom view, on the right the top view of LuNaDrone



Figure 7 *The two-sided view of LuNaDrone*

Number	Component
1	LiDAR – 360° horizontal plane
2	Propellant tank
3	IMU
4	Lithium primary D-cells
5	OBC
6	LiDAR – vertical plane
7	LED + optics
8	Camera + optics
9	ACS thrusters
10	Pressurant tank
11	Engine

Figure 8 *Part numbers*

3 Literature of the Navigation System

A reliable navigation system is a critical part for a lunar drone, this concerns both autonomous travel, safety and remote teleoperation. In history there have been crossings of 1000 kilometers among which we can note: Apollo 11, Surveyor 5, Ranger 8, Apollo 17 and Lunokhod 2.

In these missions and similar scenarios, the rover needs to operate autonomously or at least with safeguarded supervisory control modes. It must also be able to transmit images and/or videos of the surrounding environment to operators on Earth. Although hardware-related problems like: power, thermal, communication, mechanical and electrical reliability are challenging, the software aspects are equally daunting. In particular, the rover needs capabilities to enable driving over varied terrain and to safeguard its operation. Previous experience with planetary robots (in particular, Lunokhod 2 and the arm on Viking) illustrated how laborious and unpredictable time delayed teleoperation is for remote operators. A better mode of operation is supervised teleoperation, or even autonomous operation, in which the rover itself is responsible for making many of the decisions necessary to maintain progress and safety [15].

Unfortunately first mission for position estimation techniques used sensor like sun sensor, that are not an option in our scenario.

Lava tubes on the Moon are sites of considerable geological interest and hold the potential for scientific discovery and future human habitation. However, these subterranean domains present daunting challenges to exploration and sampling, including GPS-denial, communication denial, stark lighting changes, and highly dynamical motion. Free flying spacecraft have better chances to explore such environments but require robust and precise navigation for advanced autonomy.

3.1 SLAM

The meaning of SLAM is an abbreviation for Simultaneous Localization And Mapping, which is a technique for estimating sensor motion and reconstructing structure in an unknown environment.

If we consider a Simultaneous Localization and Mapping system that uses only cameras and therefore visual information, we are talking about visual SLAM (vSLAM). Visual SLAM can be used as a fundamental technology for various types of applications and has been discussed in the field of computer vision, augmented reality, and robotics in the literature [16].

Simultaneous Localization and Mapping (SLAM) is a technique for obtaining the 3D structure of an unknown environment and sensor motion in the environment. Initially this technique was devised to obtain autonomous control of robots in robotics [17]. Subsequently, SLAM-based applications have become much more popular and have been used in many more applications like: computer vision-based online 3D modeling, augmented reality (AR)-based visualization, and self-driving cars. Initially, many different types of sensors were integrated into the SLAM algorithms, such as: laser range sensors, rotary encoders, inertial sensors, GPS, and cameras [18, 19, 20, 21]

In recent years, SLAM using cameras only has been extensively analyzed and criticized because the sensor configuration is simple and the technical difficulties are higher than others. In recent years, vSLAM algorithm has been proposed in various sectors, such as computer vision, robotics, and AR [22]. These visual algorithms are especially suited for camera pose estimation in AR systems because the system configuration can be basic, a simple camera of a smartphone is enough. One of the most important requirements in AR systems is real-time response to seamlessly and interactively merge real and virtual objects. The problem of this algorithm is the high computational cost required, to solve this problem in the literature various alternatives to the algorithm have been proposed that allow it to be used even in systems of light size and weight, so the application of such vSLAM algorithms is not limited to AR systems. For example, it is also useful for unmanned autonomous vehicles (UAV) in robotics [23].

Generally, the technical difficulties of vSLAM are greater than other technologies based on SLAM logic because the cameras can acquire a much lower amount of data than those of a 360 ° laser sensor which is typically used. From such input, camera poses need to be continuously estimated and the 3D structure of an unknown environment is simultaneously reconstructed. One of the first projects using vSLAM technology was done using a monocular camera and was based on the tracking and mapping feature point in 2000s. This method is called the "feature-based approach".

In the case of having to deal with environments with a lack of structure, which means having a lack of reference points, the vSLAM algorithm no longer searches for the characteristic points of the acquisition, but directly for the whole image. This method has been proposed in the literature and is called "direct approach." With the advent of low-cost RGB-D sensors such as Microsoft Kinect, vSLAM algorithms with both a monocular image and its depth have been proposed. Therefore, the existing vSLAM algorithms introduced in this paper are categorized according to feature-based, direct, and RGB-D camera-based approaches.

3.2 Elements of vSLAM

3.2.1 Base Modules

The framework is mainly composed of three modules as follows.

1. Initialization
2. Tracking
3. Mapping

The first thing to do to start vSLAM is to define a certain coordinate system for camera pose estimation and 3D reconstruction in an unknown environment. Therefore, in the initial phase, the global coordinate system should be defined first, furthermore a part of the surrounding environment is reconstructed as part of the initial map in the global coordinate system. After the initialization, tracking and mapping are performed to continuously estimate camera poses. During tracking, the map that was initially reconstructed is recognized in the image to estimate the image's camera pose relative to the map. To do this, 2D - 3D correspondences between the image and the map are first obtained by matching the features or tracing the features in the image. Subsequently the pose of the camera is calculated from the correspondences by solving the Perspective-n-point (PnP) problem [24, 25]. Normally in most vSLAM algorithms it is necessary that some intrinsic parameters of the camera, so that they are known, are calibrated in advance. Thus, a camera pose is normally equivalent to independent camera parameters with camera translation and rotation in the global coordinate system. The mapping is done by expanding the previous map, by calculating the 3D structure of the surrounding environment, when the camera observes unknown regions.

3.2.2 Additional modules for stable and accurate vSLAM

The following two additional modules are also included in vSLAM algorithms according to the purposes of applications.

1. Relocalization
2. Global map optimization

It is necessary to relocate when, due to fast camera movement or other disturbances, tracking has failed. In the case of relocation it is necessary to recalculate the position of the camera with respect to the map. This

process is called "relocation". If this process is not incorporated in vSLAM systems, the systems can no longer function after the loss of tracking and leads to an irremediable failure making navigation systems useless. Therefore, a fast and efficient method for relocation has been discussed in the literature.

The map typically includes cumulative estimation errors based on camera movement distance. In order to eliminate the error, global map optimization is normally performed. During this process, the map is refined considering the consistency of the information with respect to the entire map. When an area of the map is revisited after a certain camera movement, it is possible to calculate the reference information representing the cumulative error from the beginning to the moment of detection. Then, a constraint on the loop from the reference information is used as a constraint to suppress the error in global optimization.

Closing the loop is a technique for capturing reference information. In closing the cycle, a closed cycle is created by matching the current image with the images acquired previously. If the loop is detected, it means that the camera has acquired one of the previously observed views. If this happens, you can estimate the cumulative error that occurred during camera movement. It is interesting to note that through the relocation techniques it is possible to perform the closed loop detection procedure. So basically the loop detection is performed to get a geometrically coherent map while the relocation for the recovery of a camera pose.

To remove the accumulated error by optimizing the camera's pose, the optimization of the pose graph is used [26, 27]. By doing this, the relationship between the camera poses is represented with a graph and the coherent graph is built to suppress the error in optimization. Bundle Adjustment (BA) is also used to minimize map reprojection error by optimizing both the map and camera poses [28]. In small environments, BA can be performed without closing the loop because the accumulated error is small. In large environments, the tuning procedure is used to efficiently minimize estimation errors.

3.2.3 Summary

In summary, the vSLAM algorithm framework consists of five parts: global map initialization, tracking, mapping, relocation and optimization. The characteristics of a vSLAM algorithm strongly depend on the methodologies used, since each vSLAM algorithm uses different methodologies for each module. Therefore, to understand the performance, advantages and limitations of the algorithm it is important to understand every part of it. It should be noted that TAM (Tracking and Mapping) is used in place of localization and mapping. TAM was initially used in Parallel Tracking and Mapping (PTAM) [29] this because mapping and mapping cannot be done simultaneously as in the traditional way. Unlike monitoring that runs on each frame with one thread, mapping is done at a certain time with another thread.

3.3 Related Technologies

3.3.1 Visual odometry

The use of odometry is to evaluate the consecutive changes of the sensor positions over time, using sensors, for example the wheel encoder, in order to obtain the relative movement of the sensor. Unlike visual odometry (VO) which is based on the use of a camera. From a technical point of view, vSLAM and VO are very important because both are techniques that estimate the positions of the sensors. The relationship between vSLAM and VO can be represented as follows.

vSLAM = VO + global map optimization

The substantial difference between these two techniques is the optimization of the global map during mapping. In the case of Visual Odometry, the geometric consistency of a map is considered only in a small portion of a map or only the relative movement of the camera is calculated without mapping. While, in vSLAM, the global geometric consistency of a map is normally considered. Basically this implies that in order to build a map, in the recent vSLAM algorithms, which is geometrically coherent it is necessary to perform the global optimization. [30, 31, 32, 33]

3.3.2 Structure from motion

Sfm or Structure from motion is a methodology to evaluate the movement of the camera and the 3D structure of the environment in a batch way [34]. In reality if you look at it technically, there is no substantial difference between vSLAM and SfM in real time.

3.3.3 MonoSLAM

The first monocular vSLAM was developed in 2003 by Davison [35, 36, 37], it was called MonoSLAM. MonoSLAM is considered a representative method in filter-based vSLAM algorithms. In this technology the movement of the camera and the 3D structure of an unknown environment are estimated simultaneously and the results are smoothed by an extended Kalman filter (EKF). 6 Degree of freedom (DoF) camera motion and 3D positions of feature points are represented as a state vector in EKF. An assumption of the prediction model is to have smooth motion, and the result of the feature point tracking is used as an observation. By varying the movement of the camera, new characteristic points are added to the state vector. It is possible to notice that initially the map is created by observing a known object in which a global coordinate system is defined. In summary, MonoSLAM consists of the following components.

1. Map initialization is done by using a known object.
2. Camera motion and 3D positions of feature points are estimated using EKF.

In this way, the major limitation is due to the high computational cost as it increases in proportion to the size of the surrounding environment. In the case of large environments, the size of a state vector increases because the number of characteristic points is greater. In these circumstances, being able to obtain the calculation in real time is very complicated.

3.3.4 PTAM

One way around the computational cost problem present in MonoSLAM is by PTAM to split the tracing and mapping into different threads on the CPU, this is the PTAM approach [38]. These two threads run in parallel so that the computational cost of the mapping does not affect the tracking. This implies that although BA needs a computational cost for optimization it can also be used in mapping. This means that the mapping evaluates the accurate 3D positions of the feature points at a computational cost, while the tracking evaluates the movement of the camera in real time. PTAM is the first method to incorporate BA into real-time vSLAM algorithms. Thanks to the publication of PTAM, most of the vSLAM algorithms follow this type of multi-threading approach.

In the PTAM configuration, the map is initially reconstructed using the five-point algorithm [39]. During stakeout the mapped points are projected onto an image to create 2D - 3D matches using texture matching. Using these matches it is possible to calculate camera poses. During the mapping it is possible to evaluate, using triangulation in certain frames, called key frames, the 3D positions of the new characteristic points. One of PTAM's most significant contributions is the introduction of this keyframe based mapping in vSLAM. When a significant difference is measured between an input frame and a key frame, an input frame is selected as the key frame. Essentially large differences are needed to have accurate triangulation. Unlike MonoSLAM, the 3D points of the feature points are optimized using global BA with some key frames and global BA with all key frames and with the map. Finally, during the monitoring process, the new PTAM view uses a relocation algorithm [40]. Use a randomized tree-based feature classifier to find the keyframe closest to the input frame. In summary, PTAM consists of the following four components.

1. Map initialization is done by the five-point algorithm [41]
2. Camera poses are estimated from matched feature points between map points and the input image
3. 3D positions of feature points are estimated by triangulation, and estimated 3D positions are optimized by BA
4. The tracking process is recovered by a randomized tree-based searching [42]

By comparing MonoSLAM and PTAM, the latter has a system capable of handling thousands of characteristic points by dividing the tracking and mapping into different threads on the CPU.

3.3.5 Comparison between MonoSLAM and PTAM

The difference between EKF-based mapping in MonoSLAM and BA-based mapping with keyframes in PTAM is discussed in the literature [43]. From the studies in the literature it appears that to improve the accuracy of vSLAM one of the methods of increasing the number of characteristic points in a map. With these considerations the BA-based approach is better than the EKF-based approach because it can handle a greater number of points.

3.3.6 Techniques on global map optimization

Geometric coherence of the entire map is maintained by using BA for keyframes. BA generally suffers from a problem due to the large number of parameters involved: the camera poses of key frames and points in the map. To avoid this problem in the closing of the cycle it is necessary to optimize the laying chart. When closing the loop, the camera poses are initially optimized using the loop constraint. After optimizing the camera poses, BA is performed to optimize both the 3D positions of the feature points and the camera poses. To make the loop closed an approach based on visual information is used [44]. A bag-of-words-based image retrieval technique has been used to detect one of the keyframes which view is similar with the current view [45].

In the case of a vSLAM system, a stereo camera is selected as the vision sensor. In this case, the scale of the coordinate system is fixed and known. In the case of monocular vSLAM there is an ambiguity of scale and the scale may vary during the movement of the camera in case the global BA is not performed. If this happens, a scale drift problem occurs, meaning that the scale of the coordinate system in each frame may not be consistent. One way to correct for scale drift is to have camera poses optimized in 7 DoF. Strasdat [46] proposed a method for optimizing 7 DoF camera poses based on similarity transformation.

As an extension of PTAM, ORB-SLAM [47] includes BA, vision-based closed-loop detection, and 7 DoF pose-graph optimization. Today ORB-SLAM is the most comprehensive feature-based monocular vSLAM system. ORB-SLAM is extended to stereo vSLAM and RGB-D vSLAM. [48].

3.3.7 Summary

MonoSLAM was developed in 2003. Both tracing and mapping are sequential and simultaneously using EKF. PTAM was developed in 2007. They proposed to separate the tracing and mapping into different threads on the CPU. This multi-threading approach allows you to manage thousands of characteristic points in the map. In large environments, it is difficult to get the overall map optimum and the camera arises due to the local minimum problem in BA. To avoid this problem, closed-loop detection and pose plot optimization can be used before BA. ORB-SLAM includes multi-threaded tracking, mapping and closed-loop detection and the map is optimized using pose graph optimization and BA, and this can be considered as an all-in-one package of monocular vSLAM.

Feature point based vSLAM algorithms typically employ handcrafted feature detectors and descriptors and can provide stable prediction results in textured environments. However, it is difficult to handle curved edges and other complex signals using such handcrafted features. In some special cases, such as environments with poor texture, line features have been used as image features. In addition, the feature points and edges are combined to obtain a reliable estimate of motion-blurred input images. [16].

3.4 Direct methods

Direct methods, unlike the methods illustrated in the previous section, directly use an input image without any abstraction using handcrafted feature detectors and descriptors. They are also called featureless approaches. Typically geometric coherence, i.e. the positions of characteristic points in an image, is used in characteristic-based methods, while photometric coherence is used to measure error in direct methods.

3.4.1 DTAM

In the DTAM algorithm, tracing is performed by taking the input image and comparing it with the images of the synthetic view generated by the reconstructed map. This procedure is equivalent to registering between an image and a 3D model of a map and is efficiently implemented on the GPU in DTAM. Using the multi-baseline stereo [49] it is possible to perform the mapping, therefore the optimization of the map takes place considering the continuity of the space [50] in order to calculate the 3D coordinates of all the pixels. The initial depth map is created using a stereo measurement like PTAM. In summary, DTAM is composed of the following three components.

1. Map initialization is done by the stereo measurement.
2. Camera motion is estimated by synthetic view generation from the reconstructed map.
3. Depth information is estimated for every pixels by using multi-baseline stereo, and then, it is optimized by considering space continuity.

Basically, these methods [51, 52, 53] are designed for fast and online 3D modeling.

3.4.2 LSD-SLAM

One of the most important direct methods is LSD-SLAM. The core idea of LSD-SLAM follows the idea of the semi-dense VO [54]. The difference with the DTAM which reconstructs complete areas in this method the reconstruction objectives are limited to the areas that have an intensity gradient. This involves ignoring the areas without texture as being able to estimate their depth from the images is very complicated. During mapping, the random values are first set as initial depth values for each pixel, then these values are optimized for photometric consistency. This method is called visual odometry since it does not consider the geometric consistency of the entire map.

During 2014, semi-dense VO was extended to LSD-SLAM [55]. In LSD-SLAM, loop-closure detection and 7 DoF pose-graph optimization, as described above, are added to the semi-dense visual odometry algorithm [56]. It can be concluded that LSD-SLAM is composed of the following four components.

1. Random values are set as an initial depth value for each pixel.
2. Camera motion is estimated by synthetic view generation from the reconstructed map.
3. Reconstructed areas are limited to high-intensity gradient areas.
4. DoF pose-graph optimization is employed to obtain geometrically consistent map.

These kinds of semi-dense approaches may succeed in having real-time processing with the CPU. In the literature [57], the accuracy of the LSD-SLAM algorithm for low resolution input images has also been evaluated. LSD-SLAM is also extended to stereo cameras and omni-directional cameras [58].

3.4.3 SVO and DSO

The mapping is done by the direct method, although the stakeout is done by matching the feature points. In feature-based methods, feature descriptors and the Lucas-Kanade tracker [59, 60] are used to find correspondences. The difference from these methods is in the camera movement which can be estimated by minimizing photometric errors around the feature points. This method is considered to be a sparse version of DTAM and LSD-SLAM

DSO is a completely straightforward method differently from SVO [61]. DSO removes as much as possible the error factors from the geometric and photometric perspectives, until it is possible to suppress the cumulative error. In this method, the input image is split into several blocks, then high intensity points are selected as candidates for reconstruction. Thanks to this technique it is possible to distribute the points within the entire image. Furthermore, the use of both geometric and photometric camera calibration results allows DSO to obtain an extremely accurate estimate. A relevant factor is that DSO only considers the local geometric consistency. Therefore, DSO is classified into VO, not vSLAM.

3.4.4 Summary

One way to classify direct methods is by map density. The characteristic of dense methods is to generate a dense map and calculate it in such a way that the depth values are estimated for each pixel in each keyframe. The utility of these methods can be found in real-time 3D modeling with GPUs. Unlike dense methods, semi-dense and scattered methods focus on applications based on tracking sensor poses. These methods can be performed in real time on the CPUs.

3.4.5 RGB-D vSLAM

Thanks to the use of RGB-D cameras, it is possible to directly obtain the 3D structure of the environment with the relative information on the texture. The scale of the coordinate system is known because the 3D structure can be acquired in metric space, unlike monocular vSLAM algorithms.

The basic depth-based vSLAM structure (D) includes an iterative closest point (ICP) algorithm [62] which has also been widely used to estimate camera displacement. This involves recreating the 3D structure of the environment by pairing multiple depth maps, all with the purpose of incorporating RGB into depth-based vSLAM.

Most depth cameras are developed for indoor use. They project IR models into an environment to measure depth information. Detecting IR patterns emitted in outdoor environments is very complicated, in addition, there is a limitation of the depth measurement range so that the RGB-D sensors can capture the environment from 1 to 4m.

3.4.6 KinectFusion

In the KinectFusion discussion a voxel space is used to represent the 3D structure of the environment [63]. The reconstruction of this structure is performed by combining the various depth maps obtained in the voxel space while the displacement of the camera is estimated through the ICP algorithm using an estimated 3D structure and the input depth map, which is vSLAM based on depth. Interestingly, KinectFusion is implemented on GPU so that real-time processing can be achieved.

One way to reduce the computational cost is to hash the voxel block during the mapping process. RGB-D vSLAM suffer from amount of data. In the literature [64], they reduce amount of data by unifying co-planar points.

3.4.7 Slam ++

Salas-Moreno proposed an object level RGB-D vSLAM algorithm [65]. The peculiarity of this treatment is that the 3D objects are registered in advance in the database and then these objects are recognized through an online process. Thanks to these 3D objects it is possible to refine the estimated map and also the amount of data is reduced as the 3D points are replaced by 3D objects.

A similar method was proposed by Tateno, it is a real-time segmentation method for RGB-D SLAM [66]. In this discussion segmented objects are tagged, so these objects can be used as recognition targets.

3.4.8 Techniques on RGB-D VO and global map optimization

RGB images can also be used in RGB-D vSLAM algorithms to perform tracing. In the literature [67, 68] relative camera motion is estimated by tracking feature points between successive frames. Using the characteristic points plotted, it is possible to estimate a translation matrix and then refine it through the ICP algorithm using depth maps. Camera motion detection methods based on photometric coherence have also been

proposed [69]. This type of photometric coherence based camera motion detection is also used in dense vSLAM methods based on monocular camera [70].

The optimization of the pose graph and the optimization of the deformation graph are used in the RGB-D vSLAM algorithms for a geometrically coherent map. In literature Kerl has succeeded in using the optimization of the pose graph to reduce the cumulative error [71]. This type of pose graph optimization is very similar to loop closure in the monocular vSLAM algorithms seen above. Whelan was able to use deformation plot optimization for map refinement and pose plot optimization for camera movement refinement [72]. Unlike other researches, the estimated map is also refined. It is interesting to note how the deformation graph optimization is often used for certain frames and the movement of the camera is instead characterized by the correspondence between an RGB-D image and a reconstructed model [73]. It was possible to estimate a coherent model which can be acquired using deformation plot optimization as often as possible.

It is important to note that the RGB-D SLAM APIs are provided in consumer devices such as Google Tango2 and Structure Sensor3. Specifically, Google Tango provides a stable estimation result by combining information from the internal sensor.

3.5 Open problems

3.5.1 Pure rotation

When a handheld augmented reality device is moved by users, a purely rotary motion sometimes occurs. This type of problem occurs because disparities cannot be observed during purely rotational motion with monocular vSLAM. One of the ways to overcome this drawback is dealt with in the literature [74], ie it is possible to use different projection models to manage the general movement of the camera and the purely rotational movement. Taking into consideration for example homography based tracking which is used for purely rotational motion and 6 DoF camera tracking which is used for other camera movements instead. Another approach is to use two types of 3D point representation depending on the movement of the camera [75]. Points that are not observable with large disparities are represented as 3D rays, while those that are are represented as 3D points, while points. During the tracking process, 3D ray information is used to estimate camera movement. The characteristic points in the image are used as reprojection errors, and the distances between the 3D rays are used.

It is important to specify that in reality purely rotational motion is not a problem in RGB-D vSLAM. This conflict is due to the tracking and mapping processes as it is possible to perform them using depth maps obtained. The mapping cannot continue during pure rotational motion in a vSLAM, monocular camera based.

3.5.2 Map initialization

To get an accurate estimate in vSLAM the map initialization procedure is important. Basically To get an accurate initial map, the baseline should be wide. However, this is not always guaranteed in practical scenarios, for example it may be difficult to perform the ideal camera movement by inexperienced people. A solution to this problem has been proposed by Mulloni, a user-friendly initialization [76]. 2D / 3D guides were used to instruct the ideal camera movement for map initialization. In literature a solution has been proposed by Arth which consists in an initialization based on 2.5D maps for external environments [77]. vSLAM can be initialized into a global coordinate system on earth.

Reference objects such as fiducial markers have been used and known 3D objects are used to obtain a global coordinate system, furthermore the initial camera poses are estimated by monitoring the reference objects. To extend a traceable area, vSLAM is incorporated with it. Vuforia4 provides marker-based SLAM initialization.

3.5.3 Estimating intrinsic camera parameters

Generally vSLAM assumes that you have known intrinsic camera parameters. At this juncture it is necessary to perform the camera calibration before using the vSLAM applications and it is also necessary to fix the intrinsic parameters of the camera during the vSLAM estimation process. In the literature there is a study in which the intrinsic estimate of the camera parameters is obtained during vSLAM [78]. During the vSLAM estimation process the intrinsic parameters of the camera gradually converge. Furthermore, the inherent modification of the camera parameters [79]. is easily managed. This is done by removing the zoom effect of the camera ie estimating the change in focal length based on an offline auto-calibration technique [80].

3.5.4 Rolling shutter distortion

Considering a shutter type is an important way of getting an accurate estimate of the camera's pose. The vSLAM algorithms assume a global shutter and these algorithms estimate the pose of a camera for each frame. Most cameras use the roller shutter due to its cost. Each line of a captured image is taken from different camera poses, this happens in cameras with a rotating shutter.

Directly estimating the camera poses of each row is extremely difficult. An interpolation-based approach to estimate the pose estimate of the rotating shutter camera is typically used. In the literature [81], a spline function is used to interpolate a camera path.

3.5.5 Scale ambiguity

Sometimes absolute-scale information is needed in some vSLAM applications with monocular vSLAM. In the literature Lee has used the user's hand to determine an absolute scale and a global coordinate system [82]. The Knorr literature also used information on the user's face to determine the absolute scale [83]. It is possible to assume that the difference in size of these body parts is small within people. Therefore, these vSLAM systems can accurately estimate information on the scale.

Another approach can be to use different sensors such as accelerometer, gyroscope and magnetic sensor on mobile phones. In the literature [84], information on the scale has been used estimated using the accelerometer. They use frequency domain filtering technique to remove sensor noise.

3.5.6 Benchmarking

Benchmarking is important and its methodologies have been discussed in recent years, to compare vSLAM algorithm.

TrakMark is a method that can provide image sequences with 6 DoF camera movement and intrinsic camera parameters [85]. It is possible to divide the image sequences into three different scenarios: virtualized environments, internal environments and external environments. To evaluate the performance of vSLAM algorithms in the AR/MR research community it is assumed to be using TrakMark. Furthermore, an evaluation

criterion from the point of view of AR/MR research has been proposed. Usually in AR/MR applications, it is okay if the overlay of virtual objects on an image is natural then the image space errors are the most important. In the case of TrakMark, the virtual object projection error (PEVO) was used as a criterion for evaluating the vSLAM algorithms [86]. This classification leads to consider that the virtual points are projected on the input images using the estimated and ideal poses of the camera. In conclusion, distances are measured in the space of the image.

In the literature Martull has been able to provide a stereo dataset following the Tsukuba dataset [87]. This stereo dataset that Tukuba analyzed was used to evaluate stereo algorithms. In addition, a new Tukuba stereo dataset was created using computer graphics. In the dataset the image sequences, camera poses and depth maps for each frame are provided. Using different camera trajectories and lighting conditions you can create the image sequences are created.

The TUM RGB-D benchmarking dataset is able to provide a sequence of RGB-D images with 6 DoF camera poses [88]. A more precise system than vSLAM in order to obtain camera poses using a motion capture system. For the evaluation of local and global errors, relative installation error (PRE) and absolute path error (ATE) respectively.

The KITTI dataset is used to evaluate the vision systems of a driving methodology and includes many types of data [89]. The visual odometry dataset is provided in the dataset. Through the use of RTK-GPS the poses of the camera on the ground are obtained.

SLAMBench unlike other datasets provides a framework for evaluating vSLAM algorithms by precision and power consumption [90]. Also, the KinectFusion implementation is included in SLAMBench in several options (C ++, OpenMP, OpenCL and CUDA).

On-site benchmarking have been organized in International Symposium on Mixed and Augmented Reality (ISMAR) since 2008, which is called "tracking competition." In the tracking competition, participants need to do specific tasks given by organizers using own vSLAM systems. Unlike dataset-based evaluation, participants can control camera movement based on current tracking results. Therefore, the tracking competition can evaluate vSLAM algorithms as an interactive system [16].

3.6 Conclusion

One way to understand the difference between the different methods is to compare them. The table below shows the summary of the representative methods. Each algorithm has different characteristics. To choose an appropriate algorithm one must consider a purpose of an application.

By combining visual and inertial data, we can achieve more stable estimation results

	Method	Map density	Global optimization	Loop closure
Mono-SLAM	Feature	Sparse	No	No
PTAM	Feature	Sparse	Yes	No
ORB-SLAM	Feature	Sparse	Yes	Yes
DTAM	Direct	Dense	No	No
LSD-SLAM	Direct	Semi-dense	Yes	Yes
SVO	Semi-direct	Sparse	No	No
DSO	Direct	Sparse	No	No
KinectFusion	RGB-D	Dense	No	No
Dense visual SLAM	RGB-D	Dense	Yes	Yes
ElasticFusion	RGB-D	Dense	Yes	Yes
SLAM++	RGB-D	Dense	Yes	Yes

Table 5 Comparison of representative algorithms [91]

3.7 LiDAR Based SLAM

The most popular technology for its simplicity and precision is LiDAR which allows 3D mapping with laser scanners. This technology, if applied to the SLAM problem, LiDAR allows to obtain a low drift motion estimation in exchange for an acceptable computational complexity [92, 93].

For the research of 2D and 3D maps, laser scanning methods certainly seem to be very important. LiDAR technology is capable of providing a huge amount of easily interpretable points to perform SLAM. One of the first attempts to reach a suitable SLAM solution with LiDAR was Stop-and-scan [94]. This method is not a reliable solution for navigation purposes even though it avoids motion distortion. One way to correct for motion distortion is IMU blending which allows you to use an error model that takes speed information as input [95]. IMU is often used to predict movement, although it is usually used to not alter the data. Research carried out [96] has allowed to demonstrate that such a method can lead to excessive convergence and to the proposed odometry based only on LiDAR distortion analysis.

Although LiDAR is applied consistently and in many areas, the technique that is used for recording the LiDAR scan has remained unchanged for almost ten years. The most common solution for LiDAR based navigation is the scan matching approach followed by a chart optimization.

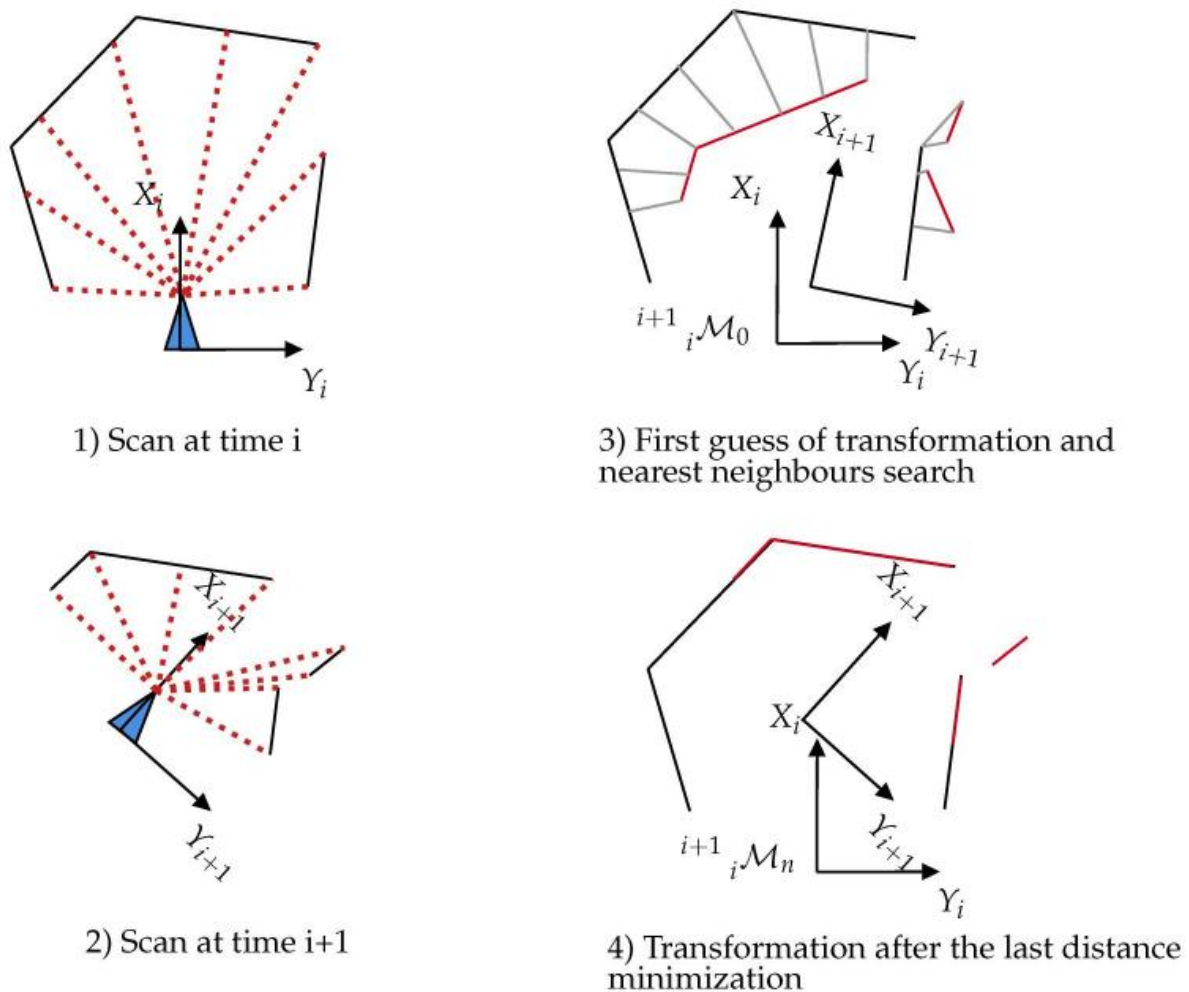


Figure 9 Principle of the ICP algorithm. At each iteration, the closest points are extracted between the two scans. From these matches, a transformation is processed and applied on the second scan. Then, the process iterates until a given cost criterion is reached.

3.8 Scan-Matching and Graph Optimization

The main process used to create 3D maps with LiDAR is scan matching and provides accurate motion information. For the registration of 3D point clouds the iterative closest point (ICP) is generally used [97]. The main drawback is the time-consuming search for point matches and its great sensitivity to the starting point of minimization. Structures of the kd-tree [98] type can be introduced to speed up the search for the nearest point. In the literature the work [99] has pointed out that the robustness of the ICP can be improved by using a probabilistic framework that takes into account the planar structures of the scans; this is called generalized ICP. Alternatively it is a Polar Scan Matching (PSM) [100] that is to estimate a correspondence between each point it uses the polar coordinates provided by the laser scanner.

At each iteration, the closest points are extracted between the two scans, this is the principle of the ICP algorithm. From these matches, a transformation is processed and applied to the second scan. Then, the process iterates until it reaches a certain cost criterion.

Using graph-based methods [101] with LiDAR is one way to reduce local errors. The history of the robot poses is represented by a graph: each node represents a sensor measurement, and the edges represent the constraint generated by the observation (coming from the ICP result). One method based on the pose graph to solve problems is to use various optimization methods such as the Levenberg - Marquardt optimizer.

The use of 2D LiDAR combined with GNSS and IMU was proposed in literature by [102], it was an example of aircraft navigation.

Both 2D and 3D LiDAR can be used to process the scan correspondence, furthermore, if the 2D LiDAR application is considered, filtering-based approaches have been proposed even in the case of a "flat" world hypothesis.

3.8.1 Occupancy Map and Particle Filter

An effective way to mediate the SLAM problem is to use a Rao Blackwellized particulate filter such as Gmapping [103]. This filter has the characteristic of greatly reducing local errors and allows to offer interesting results on planar environments. Each particle represents a possible pose and map of the robot. Generally, a large number of particles is required to correctly map the environment and lead to an increase in calculation times to non-negligible levels. In the literature a search was carried out [104] which showed a particulate filter applied to 2D SLAM, in this project it was possible to calculate a distribution of the proposals very accurately. All based on a likelihood model. Finally, the result led to an accurate map of the occupation grid, which was obtained with an order of magnitude lower number of particles compared to classical approaches. Adapting these types of techniques to 3D is very difficult due to the size of the occupancy grid.

3.8.2 Loop Closure Refinement Step

Previously we had already analyzed various solutions that allowed to obtain a localization and build a map of the environment in an odometric way. The closing phase of the cycle has been added to the LiDAR odometry in order to fully respond to the SLAM problem. Furthermore, the closing of the loop is performed when the robot is in a pre-visited place, all to improve the coherence of the global map. In the literature, there are function-based methods that allow this [105]. The use of geometric descriptors such as lines, planes or spheres is necessary in the case of laser scans. This type of descriptors is used to match scans to detect a possible loop. It is hardly possible to match each scan in real time, in the literature [106]. secondary maps

have been used that represent the environment of different scans. Generally all the finished secondary maps are automatically inserted in the scan correspondence cycle which will allow to carry out the cycle detection on a sliding window around the current robot pose. Magnusson [107] developed a loop detection process using the NDT (Normal Distributions Transform) representation of 3D clouds. This type of process is based on types of histograms of the characteristics which allow to describe the orientation and smoothness of the surface.

The project developed in [108] allowed to demonstrate that the effectiveness of the global drift of a LiDAR-SLAM could be corrected by performing the loop closure. In this study the Kalman filter was simply enhanced with a location recognition module capable of detecting loops.

LiDAR Based SLAM		
	Occupancy Map	Graph-Based
Advantages	Well known and easy to use, very accurate and precise, standard for 2D LiDAR	Allows large-scale SLAM, removes the raw data from the optimization step, allows a very simple loop closing process
Drawbacks	Dedicated to 2D environments only, cannot be used in 3D, very huge amount of memory required for large-scale environments, difficult loop closing process	Need to estimate very accurately the edges and the statistical links between the nodes; the mapping is an optional step

Figure 10 Summary of LiDAR based SLAM's advantages and drawbacks.

3.9 LiDAR-Camera Fusion

Both visual and LiDAR sensors can be used to perform psi SLAM. In the case of visual sensors there is the advantage of having a lot of previous knowledge in that area. Although, as we said earlier, V-SLAM provides accurate results, the existence of predefined parameters such as: the drift of the scale factor in the monocular case, the poor estimate of depth (delayed depth initialization) or the small interval for stereoscopic vision, the scarcity of reconstructed maps (for function-based indirect approaches), the difficulty of using RGB-D in outdoor scenarios, etc. In 3D LiDAR-based SLAM, techniques based on scan matching and graph pose are used. The resulting point clouds are usually not dense enough to be efficient, but there are solutions that focus on finding and extracting landmarks. The main advantage of using LiDAR is its excellent accuracy in measurement and, consequently, in mapping. Nowadays being able to combine both technologies would be of great help for modern SLAM applications, unfortunately this perspective requires a very complicated initial calibration step.

3.9.1 The Mandatory Calibration Step

Ensuring accurate calibration between the two sensors is required to perform SLAM with a LiDAR-camera fusion with optimal performance. However, an extrinsic calibration is crucial to be able to identify the relative transformation between the camera and the LiDAR.

Initially there were gods toolbox that allowed to propose an interactive solution to calibrate a camera on LiDAR [109]. This method allows you to manually mark points related to LiDAR scans and those of the camera frame. Literature [110] describes how automatic laser camera calibration is possible using a checkerboard. In

order to deduce a correct rigid transformation between the two sensors, a straight line extraction is necessary. It is not possible to use all these offline calibration techniques for optimal extrinsic calibration. The problem is inherent in the extrinsic parameters that can change daily and therefore require very specific conditions to function.

Assuming that deep convolutional neural networks (CNNs) have recently become popular in robotic applications, research has been carried out in the literature [111] involving the proposal of a CNN-based calibration. CNN understands LiDAR and camera disparities as inputs and allows calibration parameters to be returned. This allows us to provide a fast inline calibration solution suitable for real-time applications.

At this time, there is still no solution commonly used to process such a calibration in a simple but accurate way.

3.10 Visual-LiDAR SLAM

3.10.1 EKF Hybridized SLAM

In the overview of visual-LiDAR SLAM in the literature it has been demonstrated how the classical formulation of the extended Kalman filter (EKF) SLAM can be modified to integrate such sensor fusion. The research proposed in [112] highlighted the existence of a new EKF expression using data binding, this led to an improvement in SLAM accuracy. In association with the above it can be seen how the work in [113] also guaranteed an RGB-D camera with LiDAR EKF SLAM. The main goal of the research just mentioned was to address the problem of unsuccessful visual tracking. If the LiDAR pose is to be used to locate the point cloud data of the RGB-D camera in order to build a 3D map, it means that the above procedure has failed. A total and real fusion cannot be guaranteed with an approach of this type, but a switching mechanism between the two modes. Also in the literature [114] it has allowed to integrate SLAM algorithms based on vision and inertial measurement using EKF on a low-cost hardware environment for micro air vehicles. The use of a 2D LiDAR was inserted in the SLAM system in order to generate a 2.5D map and thus improve the estimation of the robot pose. Such proposed technologies are loose coupling modes that do not rely on the detection of features in the measurement space. In fact, the literature still lacks more closely coupled LiDAR vision sensor fusion algorithms.

3.10.2 Improved Visual SLAM

The visual-SLAM algorithms, thanks to the remarkable performances achieved, motivated the use of sensor fusion to obtain optimal solutions on those frameworks. In the literature [115] it has been investigated how LiDAR measurement was used for deep extraction. Initially, the projection of the point cloud on the frame is performed, subsequently, the estimation of the movement and the mapping were performed in order to exploit a beam adjustment based on visual key frames. A project that was developed in [116] aimed to propose a direct visual SLAM solution using a depth point cloud scattered by LiDAR. Unfortunately, an existing problem is that the camera resolution is much higher than the LiDAR resolution, this leads to the problem that a large number of pixels have no depth information. A solution has been proposed in the literature [117] to tackle the problem of resolution correspondence. After calculating the geometric transformation between the two sensors, a regression of the Gaussian process was performed to interpolate the missing values. Consequently the LiDAR was used only to initialize the characteristics detected in the images directly in the same way as the RGB-D sensors.

The solution proposed by Zhang [118] consists of a monocular SLAM associated with a 1D laser rangefinder. This solution allows to provide an efficient drift correction with a very low hardware cost, as the monocular SLAM often suffers from scale drift. In literature Scherer [119] has proposed a solution that allows to map the path and vegetation along a river thanks to a flying robot and a hybrid structure. State estimation was performed by visual odometry combined with inertial measurement and LiDAR was used to detect obstacles and map river edges. Unfortunately, the point clouds may contain occluded points which deteriorate the accuracy of the estimate. The project [120] addressed this problem by proposing a direct SLAM method with an occlusion point detector and a co-planar point detector. In these latest articles, visual-SLAM estimated pose was used to record the LiDAR point cloud during the mapping phase.

3.10.3 Improved LiDAR SLAM

Normally the camera performs feature detection, while the visual-LiDAR SLAM, LiDAR is used for motion estimation through scan matching. In literature Liang [121] has made it possible to improve the poor performance of a LiDAR-based SLAM by using scan matching with a visual loop detection scheme using ORB features. A work done by [122] analyzes a 3D laser-based SLAM and has been associated with a visual method of performing loop detection through a keyframe-based technique using visual word bags. Furthermore, Iterative Closest Point (ICP) can be optimized using LiDAR-camera fusion. Finally, in the literature [123] there is a work that used visual information to make an initial hypothesis for a rigid transformation that was used to create a generalized ICP framework.

3.10.4 Concurrent LiDAR-Visual SLAM

There was also other research that wanted to combine LiDAR and visual-SLAM results. For example project [124] intends to use both LiDAR and visual measurements by running SLAM in parallel for each mode and coupling the data. This approach was possible thanks to the use of residuals of both modes during the optimization phase. In the literature Zhang [125] has proposed a solution that couples previous research to design VLOAM. This type of visual LiDAR odometry allows performing low frequency LiDAR odometry to refine motion estimation and correct drift and high frequency visual odometry.

Probably, the work closest to a merger between the two is the one proposed in [126] this research, using a specific cost function considering both the laser and the characteristic constraints, it was possible to perform an optimization of the graph. In this case, both the image data and the laser data would allow to obtain the estimate of the robot pose. A 2.5D map was also created to speed up loop detection.

3.11 Summary

In conclusion, the previously illustrated research mainly used sensor fusion to provide additional information to a LiDAR-only or visual-only SLAM framework. Of all the ways to implement such a SLAM, the hybrid framework is the least studied. Creating a common SLAM structure using visual information and laser range appears to be a real challenge. A more tightly coupled LiDAR vision sensor fusion algorithm has not yet been fully studied in the literature and should be investigated [92, 93].

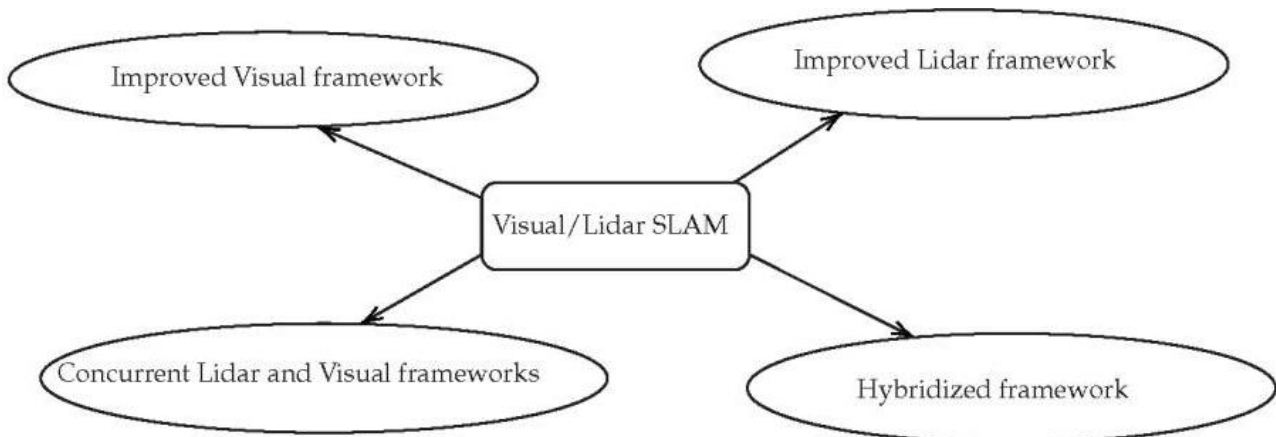


Figure 11 *Different ways of implementing visual-LiDAR SLAM.*

3.12 Conclusions

In order to find the best implementation of SLAM various studies were conducted. It has recently been shown that, for an autonomous robot, it is possible to simultaneously estimate its pose and the map of its surroundings, SLAM remains a promising and exciting research subject in robotics. Theoretically it remains a complete solution for autonomous navigation, but in practice, numerous problems occur. We cannot realistically predict to what extent the development of SLAM can lead to true autonomous navigation. This leads us to state that there is still a need to develop our understanding of SLAM and its contribution to the mobile AI robot.

Currently, there are some robust and efficient solutions that use IMU-hybridized visual sensors. Such approaches are used today in industrial applications mainly based on virtual or augmented reality. RGB-D cameras are a hot topic, but such sensors don't work well in an outdoor environment where ambient light greatly disturbs detection. Visual approaches are prone to drift and are very sensitive to the lack of salient features in the environment. Geometric features such as line, segment or edges have been studied, these are a way to solve the disadvantage of lack of features in monotonous interior environments. The main problems of these reference points are (1) the lack of accurate descriptors for the matching phase and (2) the difficult phase of initializing the corresponding 3D object with few detections. As a result, the 3D sparse representation of the environment is not very accurate due to mismatched characteristics or incorrect initialized ones. Finally, some hybrid maps are generated with different types of landmark representation. A generalized, multi-constraint MAP problem is then solved using these different objects and observations [92, 93].

LiDAR based SLAM solution provides excellent solutions. This type of LiDAR appends allow for very accurate 3D information of the environment, however they have the problem that they are very time consuming and still rely on very simple scan matching approaches which are not very robust. Still very few jobs deal with a 3D scan analysis by extracting some 3D landmarks. None of the SLAM approaches using 3D LiDAR deal with landmarks in a similar way as in the vision-based framework, this is because the processing time required for LiDAR analysis and landmark extraction is high. Right now, planes are the only features used in LiDAR-SLAM approaches. However, planes are not very useful in natural outdoor environments, which by their nature are

not well structured. LiDAR based SLAM is mainly based on matching scanning approaches such as ICP. These algorithms have remained almost the same since their invention thirty years ago.

Some experiments have been done to couple both LiDAR and visual sensors, but all of them remain at a very loose fusion level. The fusion is mainly done using the result of both odometry steps, which means that LiDAR detection or visual detection cannot help each other, and the decision is made at a very late step while fusing the relative displacement estimation. Other approaches only use the depth measurement of LiDAR to initialize the visual features directly. Once again, the capability of LiDAR is totally underused [92, 93].

4 Navigation System - Design

4.1 Introduction

Thanks to the preliminary phase of environmental analysis and future lunar missions carried out in the first chapter; it was possible to develop a preliminary plan of my mission by defining the requirements.

A first mission requirement is that the rover / lander takes us close to the crater, more precisely to a precise point so that we can know our starting position.

Since the goal of the mission is to take some photographs of the inside of the lava tube and send it to the rover so that it can then be communicated to the ground, a relatively simple mission plan was chosen to then complicate it later.

4.2 Mission plan

The mission plan provides for departure from a fixed point with a known direction (point 0).

The drone must be able to fly for the entire duration of the mission. The first step is a vertical take-off at a height (tbd) (Path A). After this the drone needs to rotate on itself until it identifies the crater with the camera, and therefore the direction (Point 1). Subsequently, the drone needs to tilt in the direction of motion to proceed, this limits the minimum height allowed as we must always have visibility of the crater to close the loop on navigation in addition to the additions to the data provided by the IMU. Finally, in the approach phase to the center of the crater, the drone needs to stop, therefore, a reverse rotation to the direction of motion of the drone is required and this limits the minimum distance of visibility depending on the height (Path B).

The center has been chosen because there is more margin on a position error and less chance of a collision, but this choice excludes some navigation methods to determine the position.

Once it has reached the center, the drone must be able to stabilize its attitude (point 2) and depending on the chosen configuration it must also be able to hover for (tbd) seconds in order to map the ground below.

Afterwards it must begin the vertical descent, during this phase a mapping of the surrounding walls is also planned (path C).

Once reached a height (tbd) from the bottom of the crater the drone must be able to stabilize and hover for (tbd) seconds, during which it must be able to rotate on itself while taking photos of the surrounding environment (point 3).

Once this phase is completed, the drone must stabilize its attitude again and begin the vertical ascent maneuver, during which the mapping of the walls continues (Path D).

Finally reached the outside of the crater it must be possible to communicate the acquired data and the images to the rover, which will then send them to the Earth (Point 2).

If at this point you still have enough fuel you can think of going back down and venturing into section G, this is a surplus to the mission and some considerations will be made later.

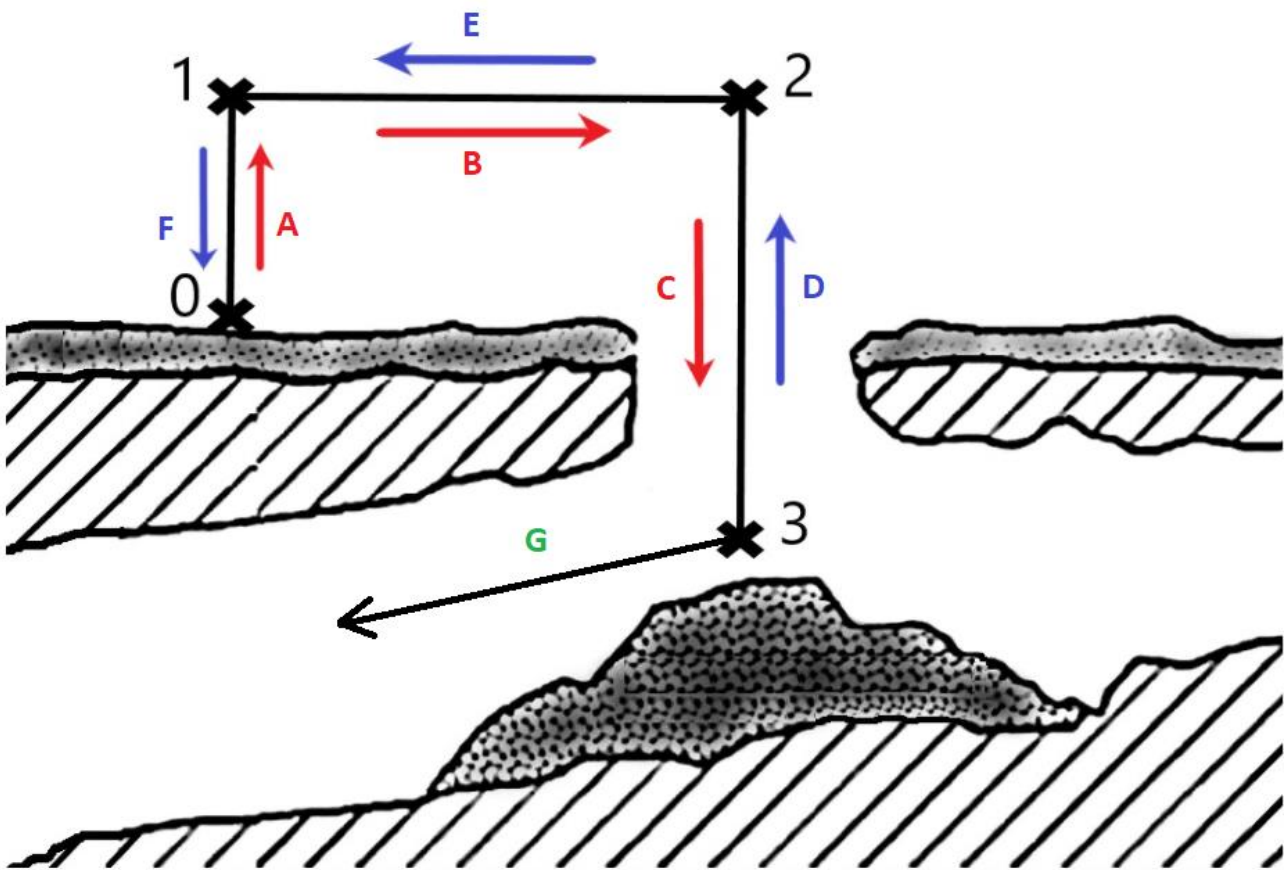


Figure 12 Mission plan

Finally, the mission can be considered concluded and the drone must proceed towards the rover using the communication system to decree the direction and land in the vicinity (Path E). During landing, the LiDAR is used as an altimeter and to map the terrain. During the descent the speed must be very limited and the attitude control very precise (Path F). This is a very critical phase and the images will be sent before landing in case of failure.

All tbd data will be analyzed in the following chapters, but it will be possible to attribute a definitive value only after various trade-off analyses.

4.3 Hardware research

To get an idea of the parameters and requirements of the various components necessary for the navigation system a search of the various hardware has been carried out and the subsequent analyzes are parametric but to obtain results, components have been chosen.

4.3.1 Cameras

The cameras are not a problem, there are all kinds of them, they have very small dimensions and require low power.

as you can see:

Name	Type	Size [dm ³]	Mass [Kg]	Power [W]	Resolution	Mpx	Pixel size [μm]	FOV	fps	min illumination [lux]
B1410	CCD EX-HAD	0,165048	0,304	5,3	1392x1040	1,4	6,45	126	30	0,5
B1411	CCD	0,165048	0,3	5,6	1392x1040	1,4	4,65	139	31	0,5
B1340	CCD	0,1908	0,337	6,7	1312x728	1	5,5	139	169	1
B1610	CCD	0,165048	0,3	5,2	1628x1236	2	4,4	135	25	0,5
B1620	CCD	0,173512	0,32	5,9	1608x1208	2	7,4	111	44	1
B1621	CCD	0,188324	0,342	6	1632x1232	2	5,5	126	42	1
B1641	CCD	0,1908	0,337	6,8	1632x1232	2	5,5	126	83	1
B1921	CCD	0,19044	0,343	6,3	1952X1112	2	5,5	121	39	1
B1922	CCD EX-HAD	0,192556	0,349	5,8	1940X1460	2	4,54	126	25	0,5
B1923	CCD	0,19044	0,17	3,6	1928X1088	2	7,4	106	37	0,5
B1941	CCD	0,1908	0,337	6,9	1952X1112	2	5,5	121	79	1
B1942	CCD EX-HAD	0,1908	0,36	5,5	1949x1460	2	4,54	127	54	1

Table 6 Comparison of various space qualified COTS cameras [annex AD_05]

The parameters that were considered to select the component are: FOV, size, weight, power consumption, resolution, fps, minimum required lighting, minimum exposure time.

In order to meet the preliminary requirements, we have chosen to adopt this camera, to have an idea of overall dimensions and dimensions. However, a communication is underway with Italian companies, as per project requirement, to create a custom optics with variable FOV and a 12 MPx camera, with attached communication and storage system.



Figure 13 ImperX 5 MP CMOS Camera C2420 [141].

Feature	Description	Feature	Description
Output Interface	Camera Link® Base, Medium, Full w/PoCL®	Strobe Output	2 strobes, programmable position and duration
Resolution	2464 (H) x 2056 (V)	Pulse Generator	Yes, programmable
Sensor	Sony Pregius IMX250 CMOS Color/Mono	Data Correction	4 LUTs pre-programmed with Gamma 0.45; Bad pixel correction (static, dynamic) Flat field correction
Sensor Format	8.4mm (H) x 7.1mm (V), 2/3" optical format	Lens Mount	C-Mount (default)
Pixel Size	3.45 microns square	P-IRIS	Optional
Shutter	Global shutter (GS)	P-IRIS Control	Auto, Programmable
Sensor Digitization	8, 10, 12-bit	Supply Voltage Range	12 V DC (5 V – 30 V), 1.5 A inrush
Frame Rate	97 fps (8-bit), 79 fps (10-bit), 35 fps (12-bit)	Power Consumption	Typical: 2.4 W
Dynamic Range	71 dB	Camera Current	Typical: 200 mA @ 12 V
Output Bit Depth	8, 10, 12-bit	PoCL	PoCL capable in Base/Medium/Full mode
Analog/Digital Gain	Manual, Auto; 0 dB – 48 dB, 480 steps	Size - Width/Height/Length	37.0 mm (W) x 37.0 mm (H) x 48.6 mm (L)
Digital Gain	1x (0 dB) to 4x (12 dB) with a precision of 0.001x	Weight	91.8 g
Black Level Offset	Manual (0 – 255), Auto	Vibration, Shock	Complies with IEC60068-2-64 and IEC60068-2-27
White Balance	Manual, Auto, Once, Off	Environmental	-30 °C to +75 °C Operating; -40 °C to +85 °C Storage
Shutter Speed	1 µs/step, 14 µs to 16.0 s	Humidity	10% to 90% non-condensing
Exposure Control	Off, Manual, External, Auto	MTBF	TBD
Regions of Interest (ROI)	2 ROI	Military Standard	MIL-STD-810G
Binning	1x2, 2x1, 2x2	Regulatory	FCC Part 15, CE, RoHS
Sub-sampling	1x2, 2x1, 2x2		
Trigger Inputs	External, Pulse generator, Software, Computer		
Trigger Options	Edge, Pulse width, Trigger filter, Trigger delay, Debounce		
Trigger Modes	Free run, Standard, Fast		
External Inputs/Outputs	2 IN (OPTO, LVTTTL) / 2 OUT (OPTO, TTL)		

Camera Info		
Size	2464x2056	PxL
FPS	27.255	fps
FTM	36.690	ms
EXP	36.690	ms

Color Spectral Response

Sony IMX250

Mono Spectral Response

Sony IMX250

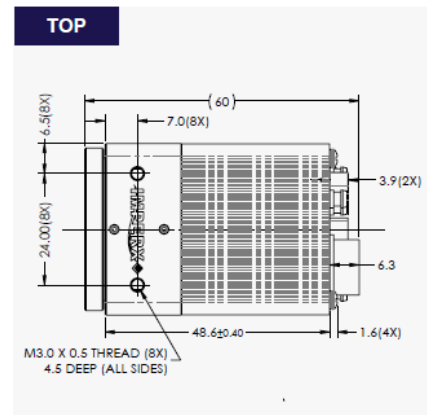
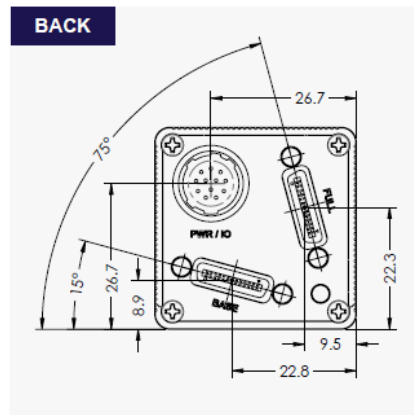
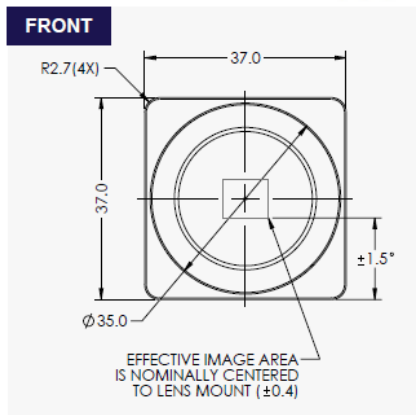
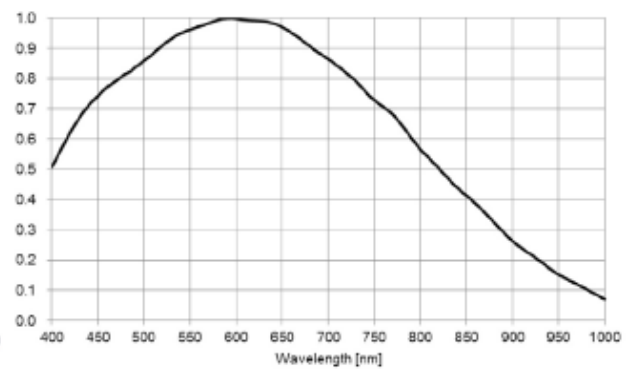
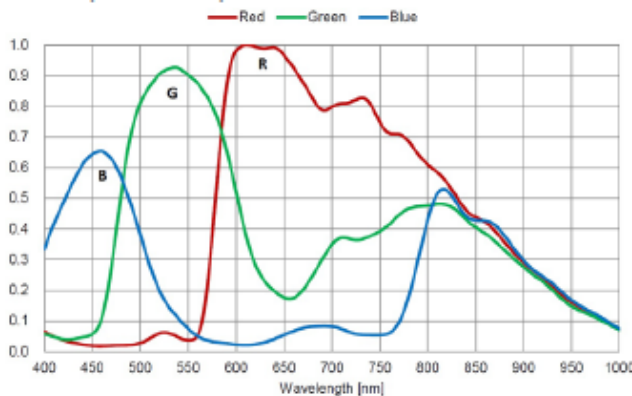


Table 7 Data sheet ImperX 5 MP CMOS Camera C2420 [141].

4.3.2 IMU (Inertial measurement unit)

Since the IMU is the mechanism that gives us the most information about our position it was chosen with high performance and limited errors [annex AD_06]. Furthermore, the energy consumption, masses and dimensions are quite similar between the various existing solutions [127].



Data Sheet:

PARAMETER	UNITS	IMU 42	IMU 42-XP
GYRO			
Gyro Bias Short Term Over Temp. (1 sigma)	°/hr.	<0.5	<0.1
Gyro Angular Random Walk	°/√hr	0.02	0.008
Gyro Scale Factor Short Term Over Temp. (1 sigma)	PPM	<150	<150
Gyro Dynamic Range	°/sec.	±2000	±1000
ACCELEROMETER			
Accelerometer Bias Short Term Over Temp. (1 sigma)	µg	<300	<300
Accelerometer Threshold	µg	10	10
Accelerometer Scale Factor Short Term Over Temp. (1 sigma)	PPM	300	300
Accelerometer VRE	µg/g ²	50	50
Accelerometer Range	g	±30/±50	±30/±50
CHARACTERISTICS			
Size	Liter	0.45	
Weight	Grams	840	
Power	W	15	
Temperature	°C	-45 to 71°	
Temperature Gradient	°C/min	3	
Power Input	VDC	±15, 5	
Interface		SDLC, RS422	
Data Rates	Hz	100 to 4800	
Sync		External or Internal	

OPTIONAL FEATURES	IMU 42-A	IMU 42-B	IMU 42-C	IMU 42-D	IMU 42-E
Nav message rates	100Hz	400Hz	1200Hz	360Hz	200Hz
Ctrl. message rates	600Hz	N/A	N/A	3600Hz	4800Hz
Acc range	±30g	±50g	±60g	±30g	±4.6g
Gyro range	1000°/s	1500°/s	2000°/s	2000°/s	Nav=162°/s Ctrl=200°/s

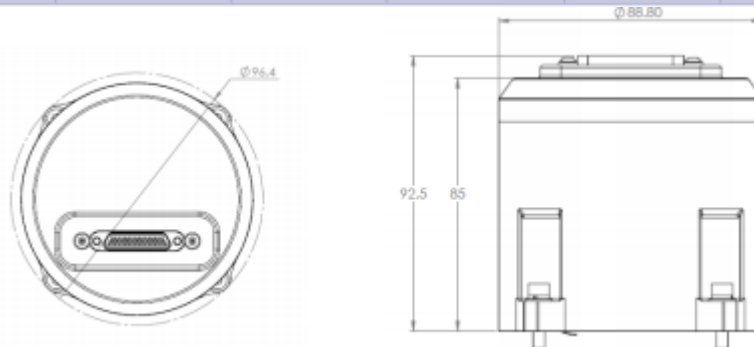


Table 8 Data Sheet IMU [127]

4.3.3 LED

This interface is more problematic, as we need to illuminate the area according to the camera's FOV and distance.

Furthermore, the solutions range from very small LEDs with low consumption, but obviously low lighting levels.

Or very high levels of consumption which, however, also generate a lot of heat and therefore also need a method to dissipate it.

Name	Size [dm ³]	Mass [Kg]	Power [W]	Power out [W]	Angle	efficiency	λ
OD-469L	0,00177	0,04	1,75	0,17	7	90	470
OD-624L	0,00222	0,03	5	0,17	7	90	624
OD-685C	0,00111	0,03	0,12	0,002	7	90	685
OD-250	0,00155	0,01	1	0,25	110	90	850
OD-666	0,00162	0,01	4	0,333	120	90	880
OD-663-850	0,00155	0,01	2,2	0,425	120	90	850
OD-669	0,002389	0,01	6	0,5	120	90	880
OD-669850	0,002389	0,01	6	1,25	120	90	850
OD-663	0,00178	0,01	2	0,17	120	90	880
OD-110W	0,00178	0,02	1	0,14	110	90	850
OD-110L	0,00199	0,02	1	0,11	7	90	850
OD-110LISOLHT	0,00155	0,01	1	0,1	7	90	880
White led	0,007912	0,06	80		120	90	

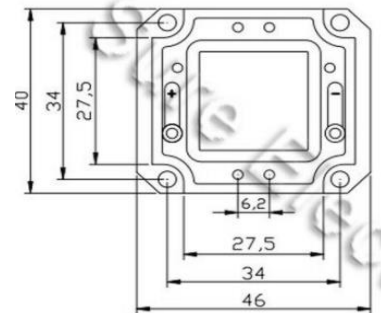
Table 9 Comparison of various COTs LEDs [annex AD_03]

According to these two assumptions, we could think of a configuration with many low-power or few high-power LEDs.

Obviously, in terms of weights and dimensions, the first configuration is very disadvantaged and since our requirements under these aspects are very stringent, we have chosen to adopt the second option [128].

Item	Symbol	Absolute Maximum Rating	Unit
Forward Current	IF	2800	mA
Peak Forward Current	IFP	5600	mA
Reverse Voltage	VR	60	V
Power Consumption	PD	\	mw
Electrostatic discharge	ESD	10000	V
Operation Temperature	TOPR	-25 ~ +120	°C
Storage Temperature	TSTG	-40 ~ +80	°C
Lead Soldering Temperature	TSOL	330 °C for 5sec Max.	

*Ifp Conditions: Pulse Wide ≤ 10msec ≤ 1/10



Item	Symbol	Condition	Min	Typ	Max	Unit
Forward Voltage	VF	IF=2800mA	32	34	36	V
Reverse Current	IR	VR=60V	0	2	10	uA
Viewing Angle	2θ1/2	IF=2800mA			140	deg
Luminous Flux	Φ	IF=2800mA	7200	8000	8800	lm
Color Temperature	Tc	IF=200mA	2700	3000	3500	K
Chromaticity Coordinates	X	IF=2800mA	0.308	0.33	0.346	\
	Y		0.329	0.345	0.36	\
Recommend Forward Current	IF(rec)	IF=2800mA			2800	mA
Color-rendering index	Ra	IF=2800mA			72	

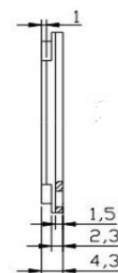


Table 10 Data Sheet LED [128]

4.3.4 LiDAR on Horizontal plane

There are many types and sizes of LiDAR, the best compromise and also the one we have chosen to use is the Ultra puck [129].

Nome	Size [dm ³]	Mass [Kg]	Power [W]	temp range [°C]	aperture angle [deg]	range [m]	accuracy [cm]	PPs	RR [Hz]
HDL-64E		12,7	60	60\ -10	360	120	2	1300000	5\20
HDL-32	0,646565	1	12	60\ -10	360	100	3	695000	5\20
Puck	0,599621	0,83	8	60\ -10	360	100	3	300000	5\20
Puck Lite	0,599621	0,59	8	60\ -10	360	100	3	300000	5\20
Puck Hi-Res	0,599621	0,83	8	60\ -10	360	100	3	300000	5\20
Ultra Puck	0,682165	0,925	10	60\ -20	360	200	3	600000	5\20
Alpha Prime		3,5	22	60\ -20	360	245	3	2400000	5\20

Table 11 Comparison of various COTs LiDAR [annex AD_08]

Specifications	
Sensor	<ul style="list-style-type: none"> • Channels: 32 • Measurement Range: 200 m • Range Accuracy: As good as ±3 cm (under typical conditions)¹ • Return Modes: 2 • Horizontal Field of View: 360° • Vertical Field of View: 40° (-25° to +15°) • Minimum Angular Resolution (Vertical): 0.33° (non-linear distribution) • Angular Resolution (Horizontal/Azimuth): 0.1° to 0.4° • Rotation Rate: 5 Hz to 20 Hz • Integrated Web Server for Easy Monitoring and Configuration
Laser	<ul style="list-style-type: none"> • Laser Product Classification: Class 1 – Eye-safe per IEC60825-1:2014 • Wavelength: ~903 nm
Mechanical/ Electrical/ Operational	<ul style="list-style-type: none"> • Power Consumption: 10 W (under typical conditions)² • Operating Voltage: 10.5 V – 18 V (with interface box and regulated power supply) • Weight: 925 g (typical, without cabling and interface box) • Dimensions: See diagram on previous page • Environmental Protection: IP67 • Operating Temperature: -20°C to +60°C (under typical conditions)³ • Storage Temperature: -40°C to +85°C
Output	<ul style="list-style-type: none"> • 3D LiDAR Data Points Generated: <ul style="list-style-type: none"> - Single Return Mode: ~600,000 points per second - Dual Return Mode: ~1,200,000 points per second • 100 Mbps Ethernet Connection • UDP Packets Contain: <ul style="list-style-type: none"> - Time of Flight Distance Measurement - Calibrated Reflectivity Measurement - Rotation Angles - Synchronized Time Stamps (µs resolution) • GPS: \$GPRMC NMEA Sentence from GPS Receiver or Over Ethernet (GPS not included)

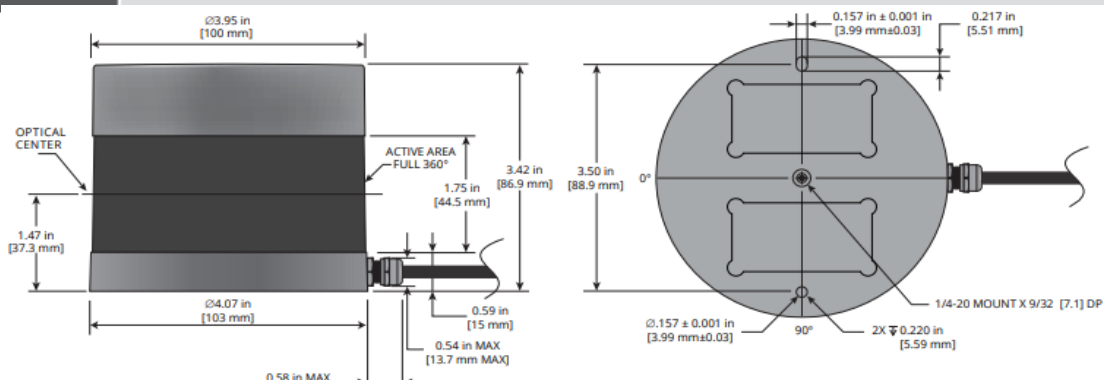


Table 12 Data Sheet LiDAR 360° [129]

4.3.5 LiDAR on Vertical plane

LiDAR in the z direction, used as an altimeter and for mapping the bottom. It requires high sampling speed and a relatively large range [130].

SCALA CHARACTERISTICS	
Laser Class	Class 1
Wavelength Sender IR-LD	905 ± 10 nm
Laser Pulse	< 5 ns with 70W approx.
Detector APD Active Area	160 µm × 595 µm, 3 elements
Horizontal Field of View	145°
Horizontal Angular Resolution	0.25°
Vertical Field of View	3.2°
Vertical Angular Resolution	0.8°
Scan Rate	25 Hz
Number of Layers	3 layers per scan 4 effective layers per 2 scans
Distance Resolution	≤ 100 mm
Typical detection range for cars	150 m

POWER	
Power Supply	9-16 V
Power Consumption	< 7 W

ENVIRONMENTAL CHARACTERISTICS	
Temperature Range	-40°C to +85°C
SCALA Protection Class	IP5K4K, IPX7, IPX9K
BroadR-Reach to Ethernet Converter Box Protection Class	Not waterproof

PHYSICAL CHARACTERISTICS	
SCALA Dimensions With Connector	60 × 108 × 102 mm (H × W × D) 60 × 135 × 100 mm (H × W × D)
SCALA Weight	610 g
Converter Box Dimensions	28 x 79 x 38 mm (H x W x D)
Converter Box Weight	50 g



Table 13 Data Sheet LiDAR limited FOV [130]

4.3.6 OBC

As regards the OBC, a configuration already used previously was chosen to get an idea of the dimensions and consumption [annex AD_09], a more in-depth study will be necessary later considering also the needs of the other subsystems [131].

General	
Expected	5 years in LEO
Processor	32-bit LEON3FT (IEEE-1754 SPARC v8) fault-tolerant processor
FPU	IEEE-754 single/double precision FPU
Processor Clock	50 MHz
SCET	15.25 μ s accuracy
SDRAM	64 MB (post-EDAC)
Instruction Cache	8 kB
Data Cache	8 kB
NVRAM	16 kB (post-EDAC)
Operating Temperature Range	-30°C to +60°C
Nonvolatile System Memory Nand Flash	2 GB (post-EDAC)
Power Supply Input	4.5 V to 16 V
Radiation (TiD)	20 kRAD [qualified >30 kRAD, Si]



Figure 14 OBC design

Interfaces		
SpaceWire	50 Mbps	2
Serial Ports	RS422 / RS485 UARTs	6
Serial Ports	RS485-only UARTs	2
PSS Interface	RS485 PPS input / output	1/1
Analog Input Buffered	24 bit, up to 31250 SPS	8
GPIO	3.3 V logic	16
Debugging	JTAG port for CPU debugging via GRMON/GDB	1
CAN	Implemented on optional daughter board	2
SpaceWire	Implemented on daughter board	2

Size, Weight & Power	
Nominal Power Consumption	1.3 W
Mass	130 g
Length	95.89 mm
Width	90.17 mm
Height	17.20 mm
Height - Optional daughter board	12.50 mm

Table 14 Data Sheet OBC [131]

4.3.7 Laser distance sensor

The laser distance sensor acts as an altimeter, and the maximum distance range depends on the type of surface on which the laser impacts, in a conservative analysis it was decided to consider a sensor that is able to provide sufficient detection even in the worst condition, i.e. with a black surface [132] [annex AD_07].

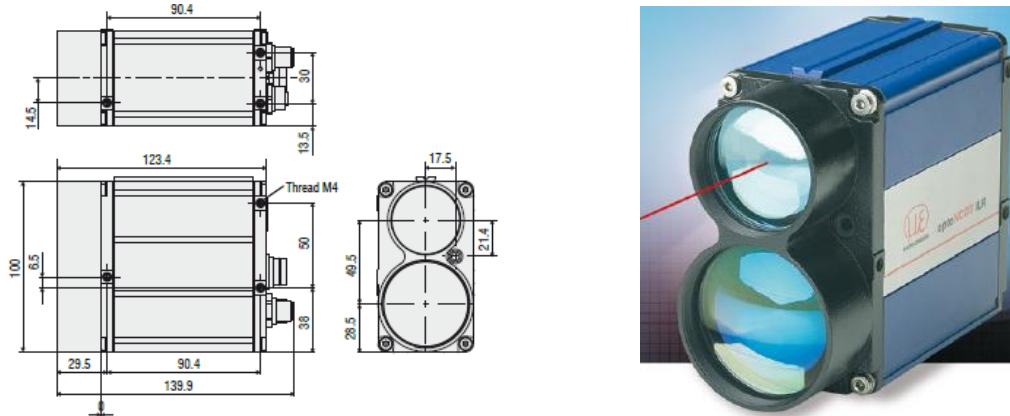


Figure 15 Laser measurement distance sensor

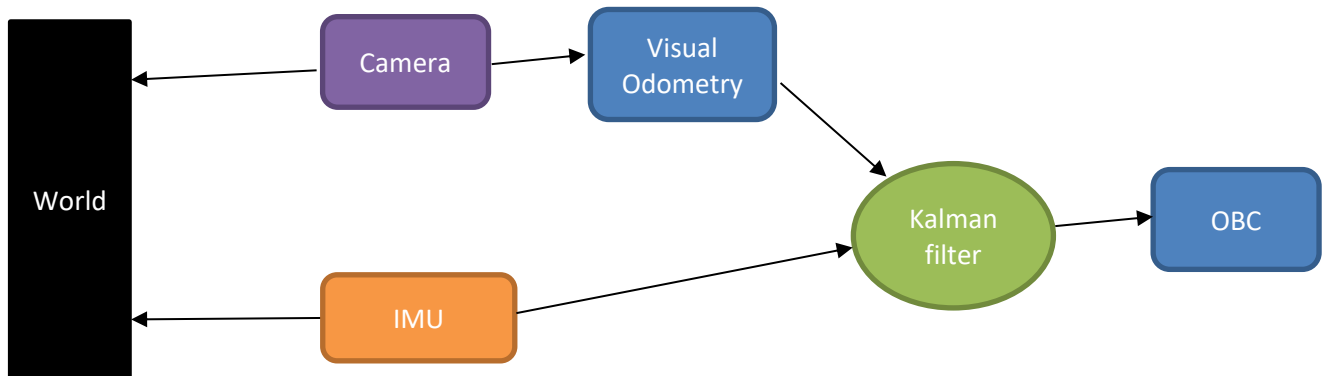
Model	ILR1191-300	
Article number	7112010	
Measuring range ¹⁾	black 6%	8 ... 150 m
	gray 10%	0.5 ... 200 m
	white 90%	0.5 ... 300 m
	Reflector film	0.5 ... 3000 m (ILR-RF250)
Speed	0 ms ⁻¹ to 100 ms ⁻¹	
Accuracy	≤ 20 mm	
Resolution	1 mm	
Linearity ²⁾	± 20 mm (at measurement output 100 Hz) ± 60 mm (at measurement output 2 kHz)	
Measurement frequency	Distance measurement	2000 Hz
	Speed measurement	80 Hz
Light source	Measuring laser (infrared 905 nm) Sighting laser (red 635 nm)	
Laser safety class	EN 60825-1:2014	Measuring laser (laser class 1) Sighting laser (laser class 2)
Operating temperature	-40 ... +60 °C	
Storage temperature	-40 ... +70 °C	
Switching outputs	Q1 / Q2 (max 200 mA)	
Switching points	freely adjustable	
Switching hysteresis	freely adjustable	
Trigger input	adjustable trigger edge and delay, trigger pulse max. 30 V	
Serial interface	RS232 and RS422 with 1.2 kBaud ... 460.8 kBaud 24 bit, gray-coded, 50 kHz ... 1 MHz	
Profibus	RS485, 9.6 kBaud ... 12 MBaud	
Operating mode	single measurement, continuous measurement, external triggering, speed measurement	
Analog output	4 ... 20 mA (16 Bit DA)	
Temperature stability	≤ 50 ppm / °C	
Power supply	10 ... 30 VDC	
Max. power consumption	< 5 W without heating, 11.5 W with heating	
Connection	1 x 12-pin M16, 2 x 5-pin M12 B-coded	
Protection class	IP67	
Housing material	Aluminum strangeness profile, powder-coated	
Weight	800 g (depending on the equipment)	
Vibration/shock	500 g, 0.5 ms, 1 shock in each direction (DIN ISO 9022-30-08-1)	
	10 g, 6 ms, 1000 shocks in each direction (DIN ISO 9022-3-31-01-1)	

Table 15 Data Sheet Laser Distance sensor

4.4 Navigation - Option 1

In the first phase of approach to the crater it was decided to use an IMU and visual navigation on the crater as to establish the position. The camera used for the visual navigation is the same that will then take the photos in the next phase of the mission.

The recognition of the 3D image of the crater has a relatively low computational weight and allows to have a confirmation of the position, as well as improve errors. Without relying only on the integration of the estimated position by IMU permits to reduce the cumulative error.

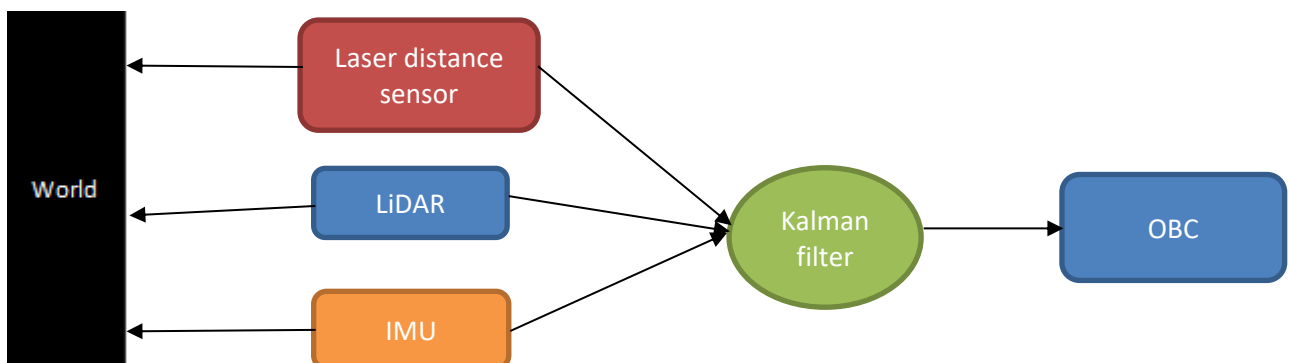


In the descent phase an IMU is always used in conjunction with a LiDAR which allows to close the loop on the position.

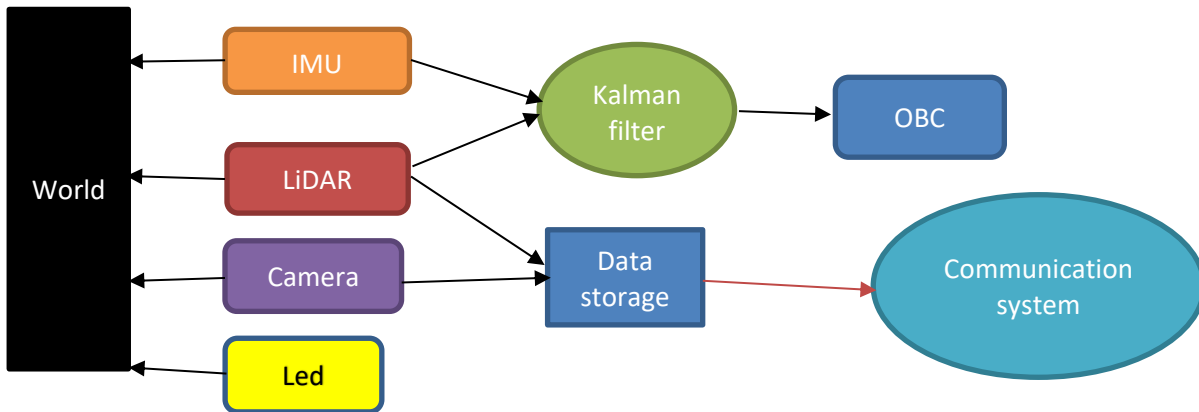
Furthermore, the LiDAR would be necessary for the mapping during the descent, a part of the collected data is used to close the loop with the navigation done by integrating the data provided by the IMU.

Since the data collected by the LiDAR does not need to be processed in real time, the necessary computing capacity is relatively low.

A laser distance detector is used to figure out the distance to the bottom and prepare for the hovering maneuver.



Once reached the bottom it is necessary to rotate the drone on itself and take photographs, during this period it is also necessary to illuminate the surrounding environment; therefore an effective method of lighting must be considered.



The ascent maneuver is carried out in the same way as the descent one, and in the same way it is possible to collect other data relating to the walls of the crater

Reached the top it is necessary to communicate the data collected, to do this the drone must be equipped with an adequate communication system

4.5 Figures of merit

From the system analysis it is possible to estimate some figures of merit that characterize the system [annex AD_10].

	<i>Size [L]</i>	<i>Mass [Kg]</i>	<i>Power [W]</i>
<i>LiDAR XY</i>	0,682165	0,925	10
<i>Laser sensor</i>	0,70338	0,8	5
<i>IMU</i>	0,45	0,84	15
<i>CAMERA</i>	0,36	0,34	4,2
<i>LED</i>	0,007912	0,06	80
<i>OBC</i>	0,13	0,148718102	1,3
<i>Total</i>	2,333457	3,113718102	115,5

Table 16 System features considering the configuration 1

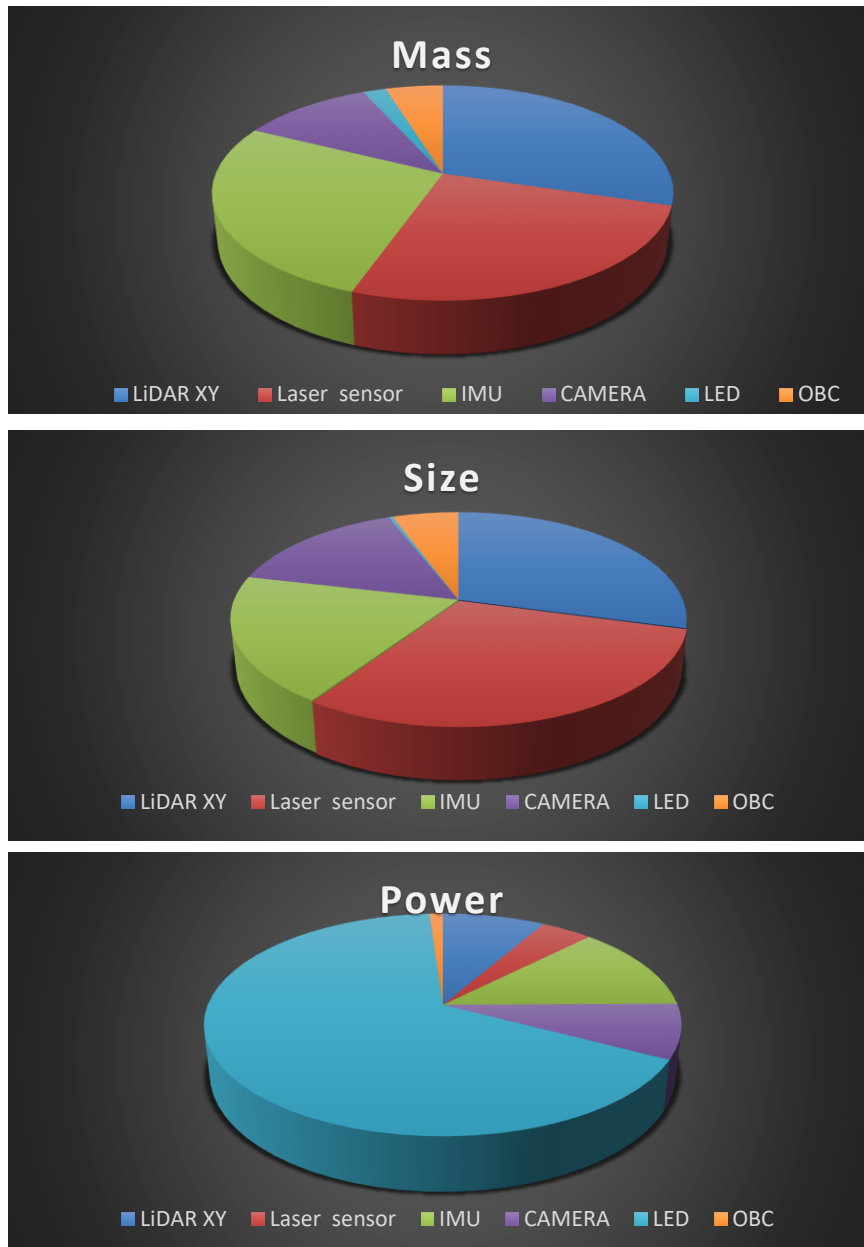


Figure 16 Power, Mass, Size comparison in configuration 1

4.6 Starting altitude Limitation

4.6.1 Vision and Tilt limitation

In the initial phase, the take-off is vertical and the drone is not tilted. Considering the chamber positioned at an angle of 30° downwards. With a 120° FOV for navigation. there are no altitude restrictions such as visibility. However, a minimum height is required to be able to see the crater.

The real limitation is given by the deformation that the crater undergoes as a function of the distance and height at which the drone tries to identify it. This was estimated with geometric correlations and assuming a distance from the crater of 150m and a crater diameter of 100m.

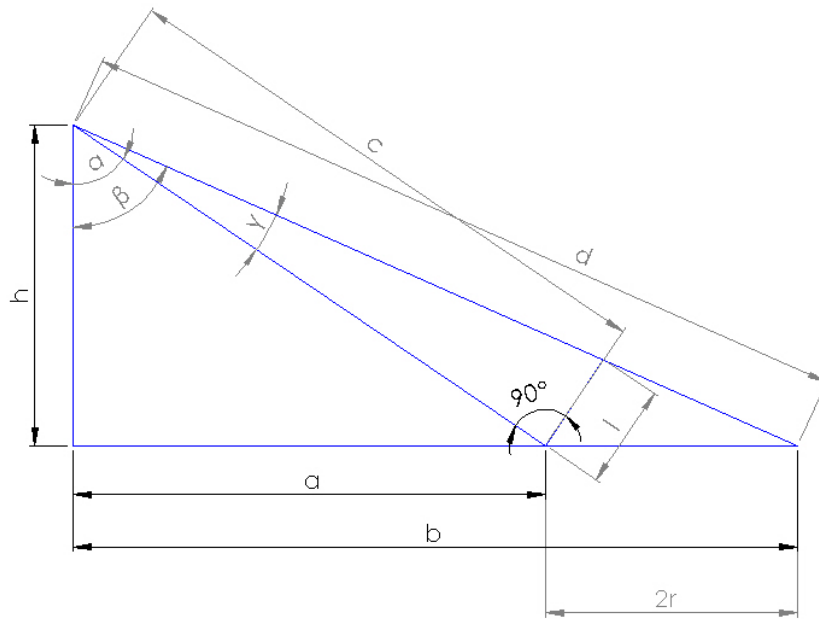


Figure 17 Geometric representation of drone-crater angles

$$\begin{aligned}
 c &= \sqrt{h^2 + a^2} & b &= D + 2r \\
 a &= D - 2r & d &= \sqrt{h^2 + b^2} \\
 \alpha &= \arccos\left(\frac{h}{c}\right) & \beta &= \arccos\left(\frac{h}{d}\right) \\
 \gamma &= \beta - \alpha & l &= c \cdot \tan(\gamma)
 \end{aligned}$$

Putting the formulas together we get:

$$l = \sqrt{h^2 + (D - 2r)^2} \cdot \tan\left(\arccos\left(\frac{h}{\sqrt{h^2 + b^2}}\right) - \arccos\left(\frac{h}{\sqrt{h^2 + a^2}}\right)\right)$$

Where:

l = semi – minor axis
 r = radius
 D = distance
 h = height

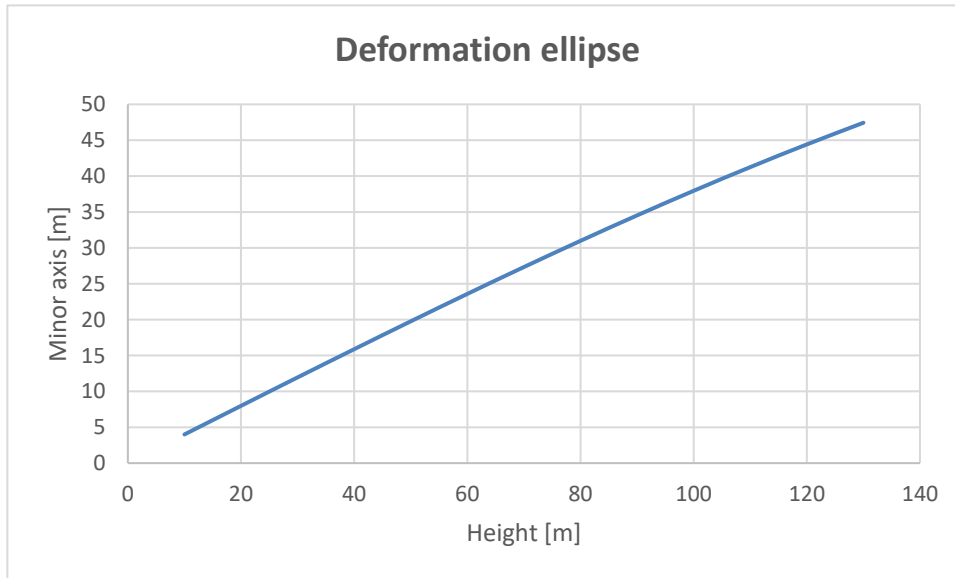


Figure 18 Deformation of the circle as a function of elevation and distance from the crater.

The navigation algorithm allows to identify the crater and therefore the direction to follow. To do this, a model of the crater was previously loaded which will then be compared with the acquired images. To this purpose the crater must have a shape that conforms to the preloaded one. It is therefore assumed that a crater deformation value of $\frac{\text{Diameter}}{\text{semi-major axis}} = 10$, is acceptable for navigation. As can be deduced from the calculations carried out, this implies an initial height of approximately 30 m.

The inclination of the drone necessary to move depends on the propulsion system and consumption. The optimal value for consumption is provided by the analysis of the flight plan and is 37° [13] [14].

To carry out this analysis, geometric considerations were carried out in two different cases. In the case of positive inclination, i.e. advancement of the drone and in the case of braking then inclination with a negative angle [annex AD_13].

In the initial phase the distance was assumed and through the geometric considerations:

$$H = \frac{D}{\tan(\theta)} \cos\left(\gamma - \alpha - \frac{\beta}{2}\right)$$

$$\theta = 180 - (\alpha + \gamma) + \frac{\beta}{2}$$

Where:

H = height

D = distance

α = drone inclination

β = FOV camera

γ = camera inclination

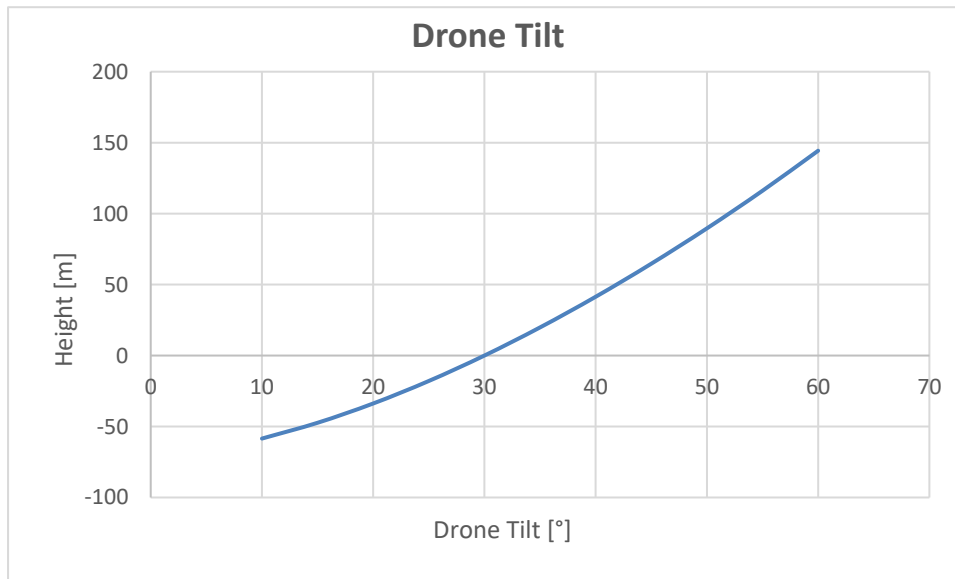


Figure 19 Drone tilt, depending on the height above the ground, during the first rotation in order to accelerate, assuming a distance from the crater of 200m

Negative values have the meaning of representing the visibility of the cameras even at negative angles, so for negative values we have no height limitations.

In the braking phase, on the other hand, the height was assumed and the minimum distance at which one must be in order to view the crater was calculated.

$$D = (H \cdot \tan(\theta)) \cdot \cos\left(\gamma - \alpha - \frac{\beta}{2}\right)$$

$$\theta = 180 + (\alpha + \gamma) + \frac{\beta}{2}$$

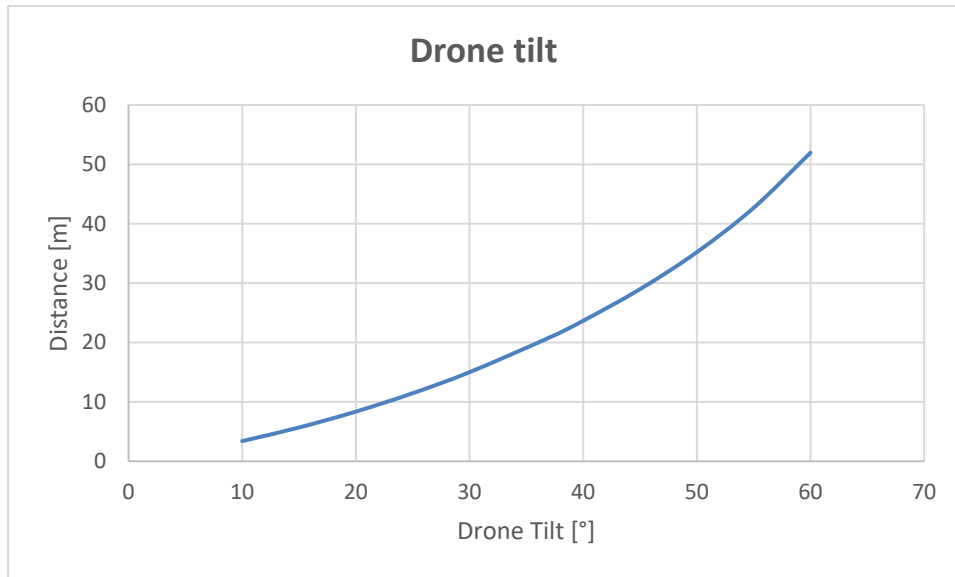


Figure 20 Drone tilt, depending on the distance from the crater, during the second rotation in order to decelerate and approach the crater, assuming a height from the ground of 30m.

The first real limitation comes from the inclination necessary to move the drone. During this phase we must be able to maintain the visibility of the crater in order to correct the errors that accumulate during the integrations of the IMU.

In these analyzes it was considered as the drone angle of inclination 37 ° in accordance with the minimum consumption required [13]. A trade-off analysis will then be necessary to define the system.

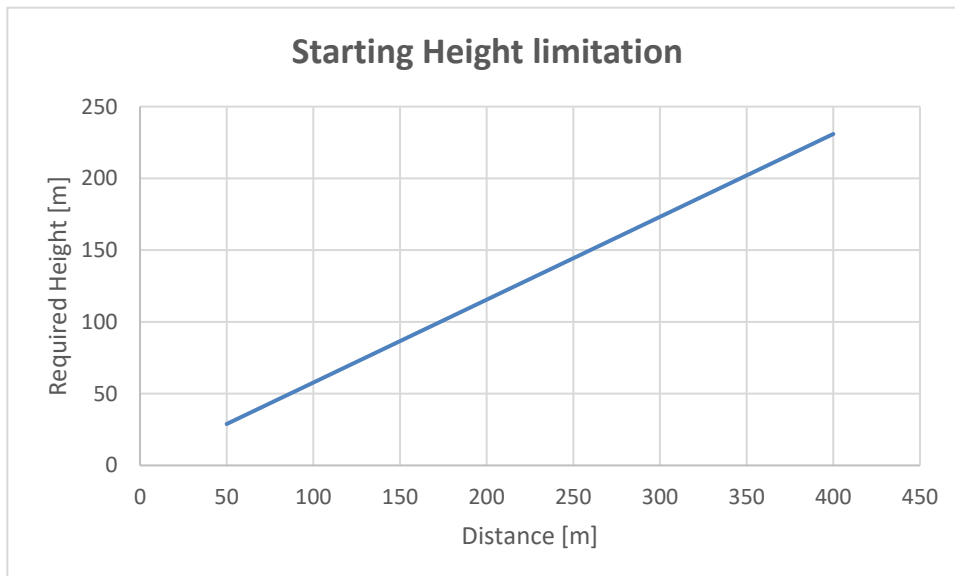


Figure 21 Limitation on the minimum necessary flight height after the initial inclination as a function of the distance from the crater in order to maintain visibility.

Unlike the initial phase, in the stopping phase, the rotation is reversed, so the lower we are the better. Furthermore, the independent variable in this case is distance and not height.

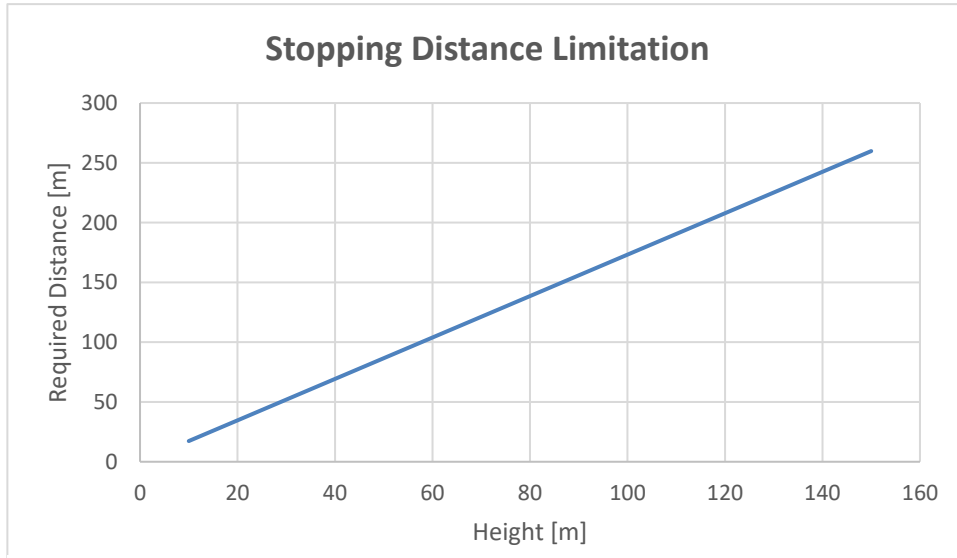


Figure 22 Limitation on the minimum necessary distance from the crater after the final inclination as a function of the height from the ground in order to maintain visibility of the crater.

4.6.2 Minimum pixel data error estimation

Another limitation is due to the maximum perception of objects which is a function of distance, FOV and image quality.

Assuming a crater size of 50m, in the case of a 4MPx camera with a horizontal resolution of 2048 pixel.

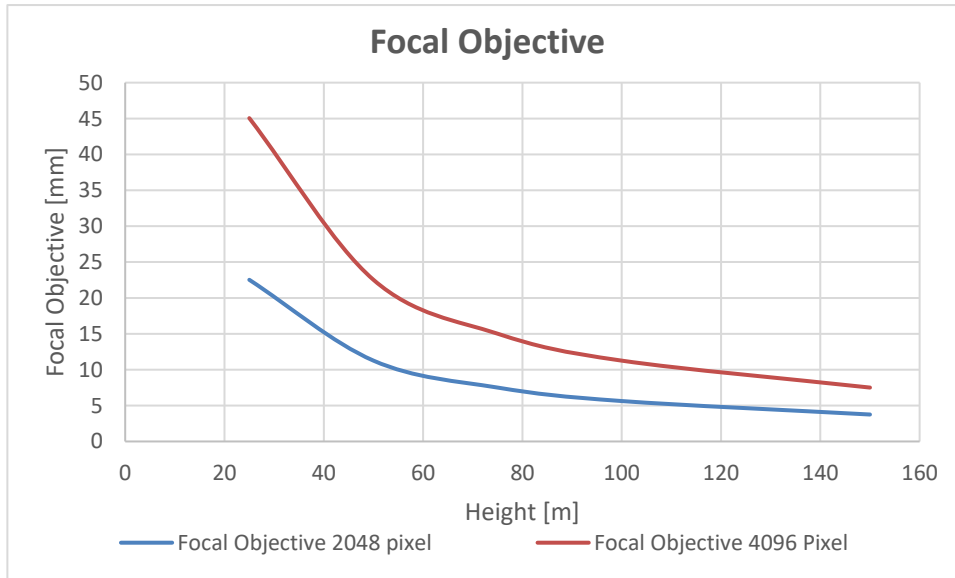


Figure 23 Comparison Focal lens size as a function of the distance from the lens.

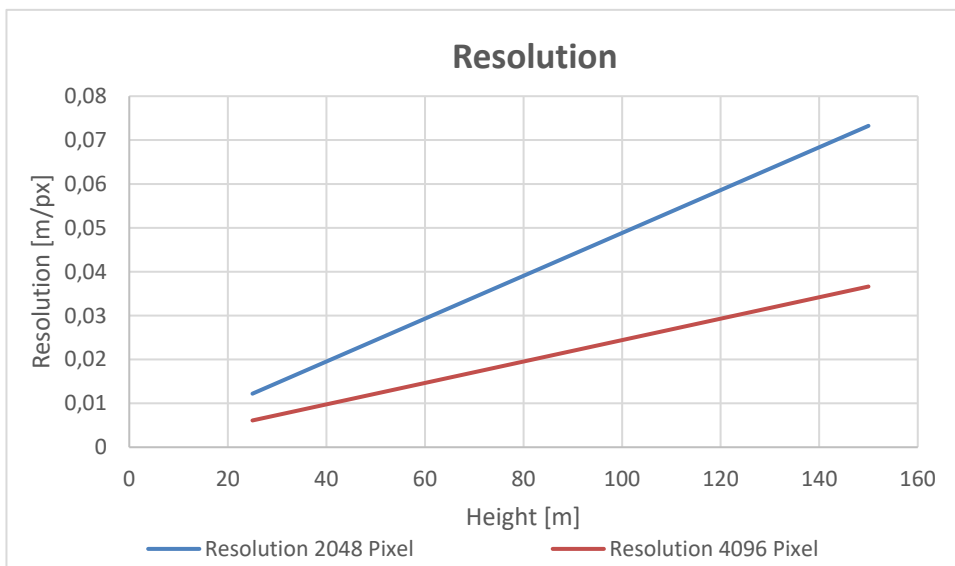


Figure 24 Comparison between the two resolutions as a function of the distance from the crater.

According to the graphs above, the resolution given by the cameras is not the predominant limitation. As you can see, a maximum of a few tens of centimeters is reached as a minimum value.

4.7 Vertical Speed Limitation

By imposing the final speed equal to 0 it is possible to find the maximum speed that allows us to stop considering the distance of the detection.

$$s = \frac{v^2 - v_0^2}{2a} \quad \rightarrow \quad s = \frac{v^2 - v_0^2}{2 \cdot \frac{T}{m}}$$

to consider the various delays, the space covered during the delay was added and the maximum speed allowed was recalculated:

$$s_{delay} = t_{delay} \cdot v_0; \quad t_{delay} = t_{algorithm} + t_{truster}$$

$$Distance = s_{delay} + s$$

to estimate the delay, the activation time of the engine and the navigation algorithm were taken into consideration. also you want 10 times the sampling frequency of the control frequency.

Speed measurement frequency	80	Hz
Distance measurement frequency	100	Hz
Measuring range	200	m
Measuring accuracy	0,02	m
Delay of the thruster	0,02	s
Delay of the algorithm	0,125	s
Delay	0,145	s
Thrust	50	N
Drone mass	15	kg

Table 17 Speed Limitation according to configuration 1

this type of approach is conservative as the mass and thrust of the drone are considered constant, it will need to be refined later [annex AD_10].

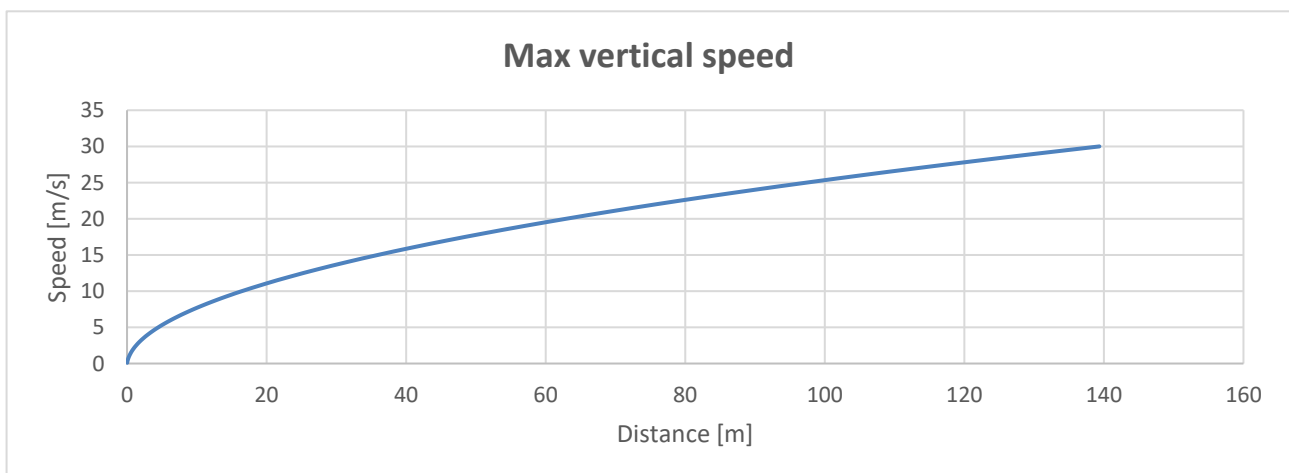


Figure 25 Max Vertical Speed according to the configuration 1

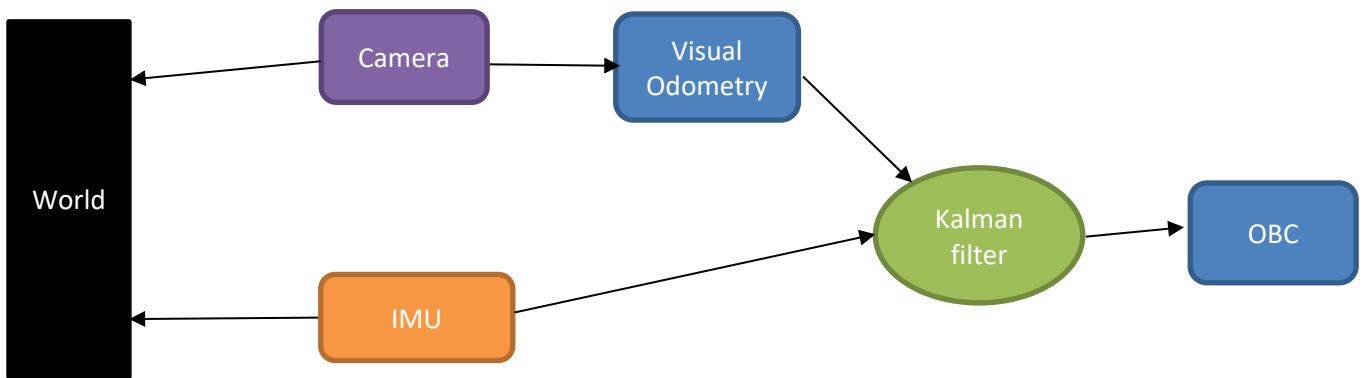
As it can be seen, the speed limitation is given by the obstacle detection distance. Why do we care about the maximum allowed speed? Because the consumption is directly linked to speed. the faster we go the better. The parameters that allow to improve this restriction are precisely the distance, which however is not always dependent on the instrumentation, but more on the conformation of the ground, the thrust of the engine and the delay on the commands due to the processing of navigation data and the response of the engines.

Once the drone has perceived an obstacle it must be able to process the data, send them to the navigation system that gives the command to the propulsive one and begins to brake until it stops before crashing. In our case it just stops at a predetermined distance from the ground in order to carry out the hovering maneuver, but the concept is the same.

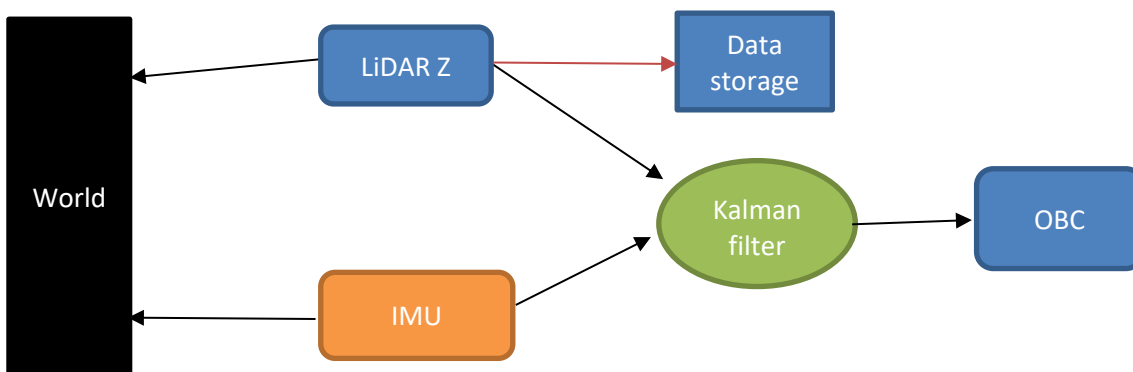
4.8 Navigation Option 2

The first stage in this configuration does not differ from the previous one. For the first phase of approach to the crater it was decided to use an IMU and visual navigation on the crater as to establish the position. The camera used for the visual navigation is the same that will then take the photos in the next phase of the mission.

The recognition of the 3D image of the crater has a relatively low computational weight and allows to have a confirmation of the position, as well as improve errors. Without relying only on the integration of the estimated position by IMU permits to reduce the cumulative error.



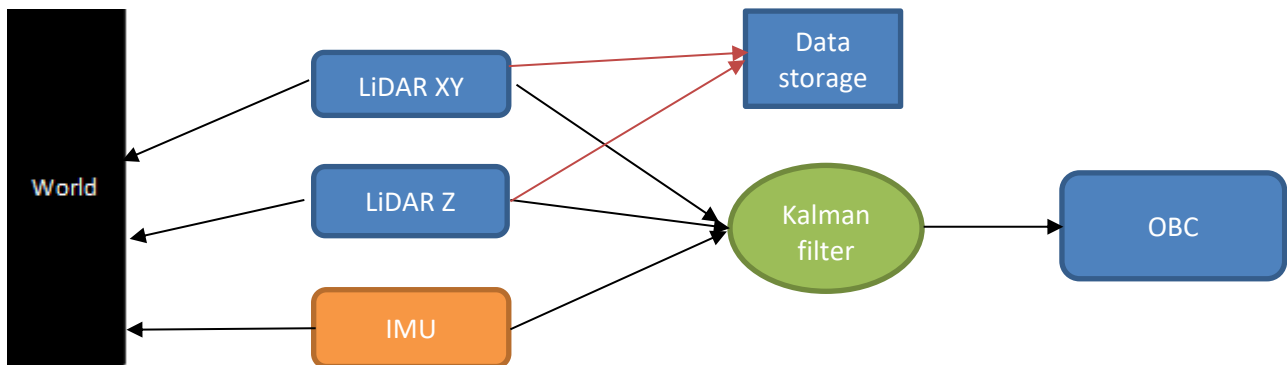
Unlike the previous configuration, a hovering period is required, between the approach to the crater and the descent phase, which is necessary for mapping the crater floor using LiDAR.



In the descent phase an IMU is always used in conjunction with the two LiDAR which allows us to close the loop on our position.

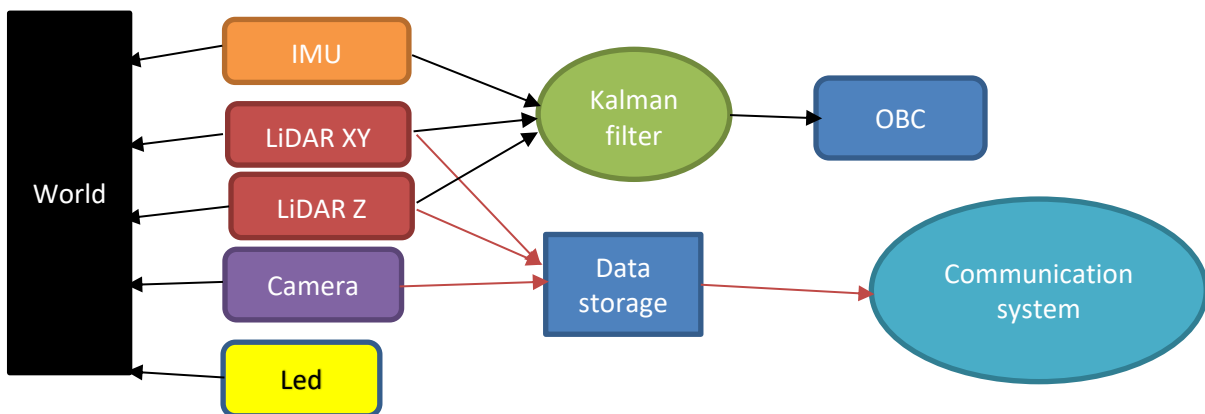
Furthermore, the LiDAR would have been necessary for the mapping during the descent, a part of the collected data is used to close the loop with the navigation done by integrating the data provided by the IMU. Since the data collected by the LiDAR does not need to be processed in real time, the necessary computing capacity is relatively low.

Here the LiDAR on z is used only as an altimeter, thus increasing the sampling frequency, to figure out the distance to the bottom and prepare for the hovering maneuver.



Once reached the bottom it is necessary to rotate the drone on itself and take photographs, during this period it is also necessary to illuminate the surrounding environment; therefore an effective method of lighting must be considered.

In addition, the bottom is mapped more precisely during this maneuver.



The ascent maneuver is carried out in the same way as the descent one, and in the same way it is possible to collect other data related to the walls of the crater.

Reached the top it is necessary to communicate the data collected, to do this the drone must be equipped with an adequate communication system.

Section F of the flight plan will be further explored later.

4.9 Figures of Merits

	Size [L]	Mass [Kg]	Power [W]
LiDAR XY	0,682165	0,925	10
LiDAR Z	0,648	0,51	7
IMU	0,45	0,84	15
Camera	0,36	0,34	4,2
LED	0,007912	0,06	80
OBC	0,13	0,148718102	1,3
Total	2,278077	2,823718102	117,5

Table 18 System features considering the configuration 2 [annex AD_10]

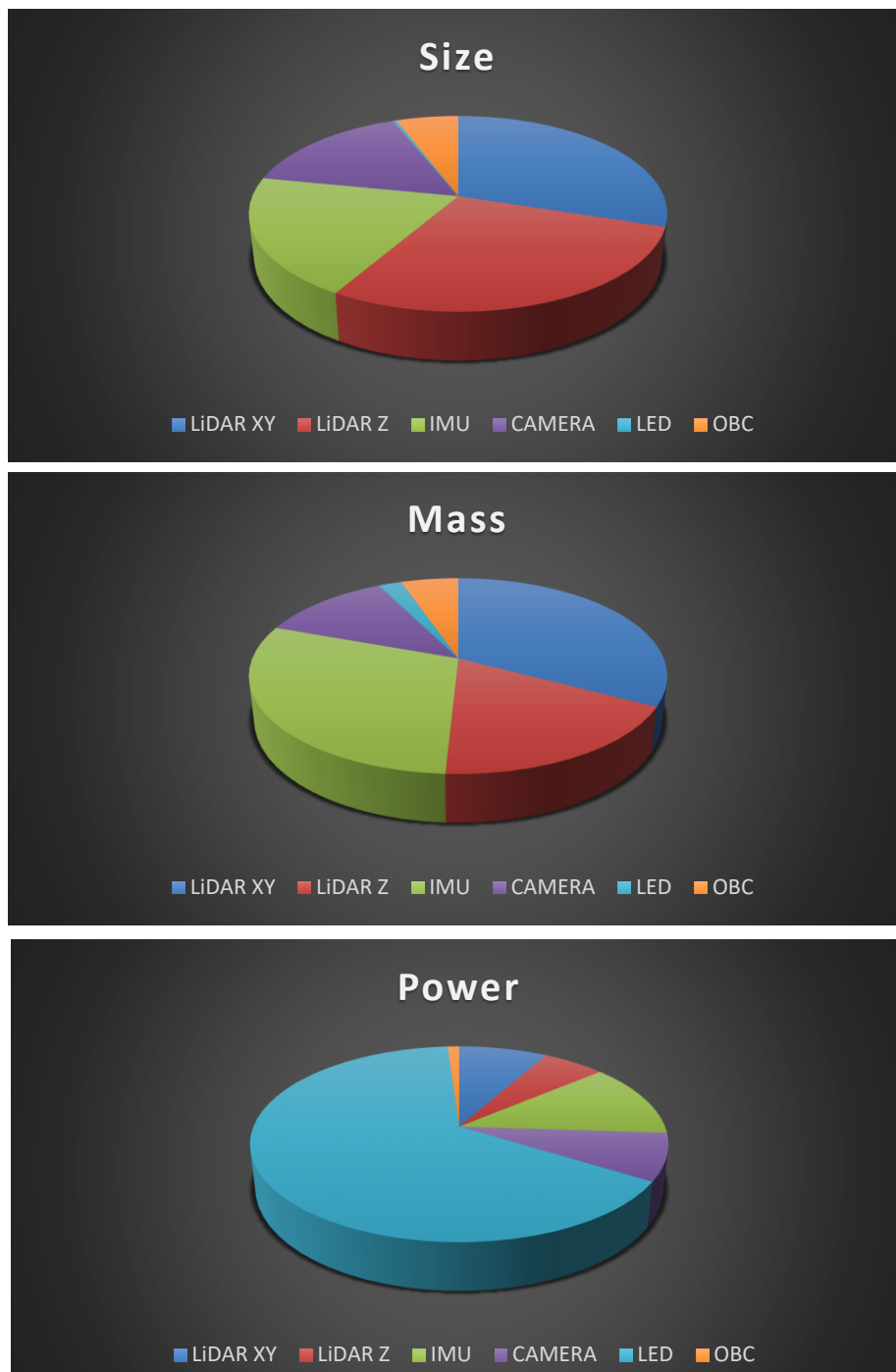


Figure 26 Power, Mass, Size comparison in configuration 1

4.10 Vertical Speed Limitation

Here too the considerations made above are the same, the only difference is the properties of the individual components. In this regard, I omit the theoretical considerations and focus only on the results explicit [annex AD_10].

<i>Speed measurement frequency</i>	25	Hz
<i>Distance measurement frequency</i>	25	Hz
<i>Measuring range</i>	150	m
<i>Measuring accuracy</i>	0,04	m
<i>Delay of the thruster</i>	0,02	s
<i>Delay of the algorithm</i>	0,4	s
<i>Delay</i>	0,42	s
<i>Thrust</i>	50	N
<i>Drone mass</i>	15	kg

Table 19 Vertical Speed Limitation according to configuration 2

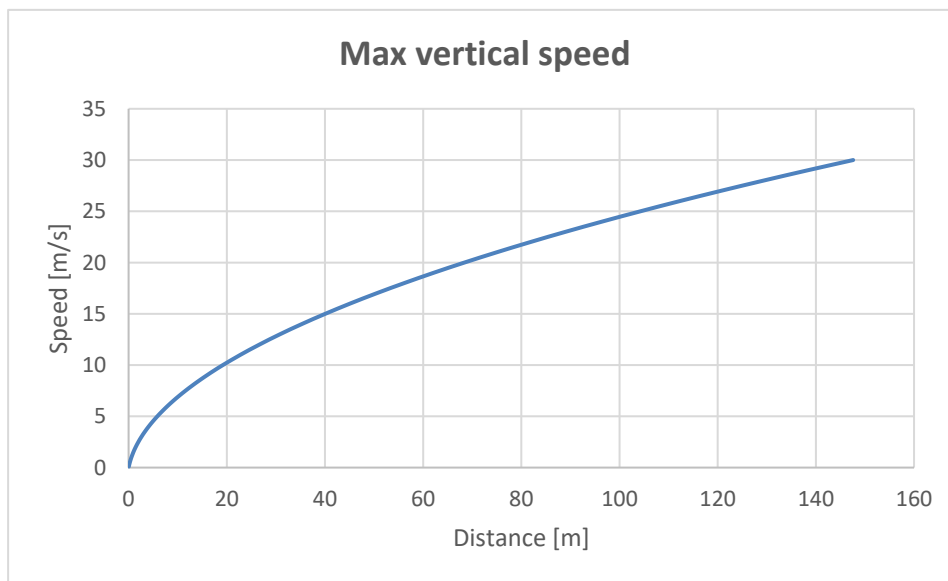


Figure 27 Max Vertical Speed according to the configuration 2

It can be seen that the maximum allowed speed is lower in this configuration because the LiDAR has a sampling frequency much lower than a simple laser altimeter, but it gives us much more complete data. Furthermore, the hovering time to map further penalizes this configuration.

4.11 Horizontal speed limitation

By imposing the final speed equal to 0 it is possible to find the maximum speed that allows to stop considering the distance of the detection [annex AD_10].

In this case, the case of a drone already in possession of a speed and must stop was considered, the acceleration phase from a standstill must be analyzed separately,

$$s = \frac{v^2 - v_0^2}{2a} \quad \rightarrow \quad s = \frac{v^2 - v_0^2}{2 \cdot \frac{T}{m}}$$

Unlike the previous cases, here the main delay is due to the need to rotate the drone to reverse the thrust, this is done through secondary motors with very low thrusts. To consider the various delays, the space covered during the delay was added and the maximum speed allowed was recalculated

$$s_{delay} = t_{delay} \cdot v_0; \quad t_{delay} = t_{algorithm} + t_{thruster} + t_{rotation}$$

$$Distance = s_{delay} + s$$

to estimate the delay, the activation time of the engine and the navigation algorithm were also taken into consideration. Also you want 10 times the sampling frequency of the control frequency.

<i>Camera measurement frequency</i>	15	Hz
<i>measurement frequency</i>	15	Hz
<i>Measuring range</i>	200	m
<i>measuring accuracy</i>	0,2	m
<i>Time rotating drone</i>	1	s
<i>Delay of the thruster</i>	0,02	s
<i>Delay of the algorithm</i>	0,666667	s
<i>Delay</i>	1,686667	s
<i>Horizontal thrust</i>	50	N
<i>Drone mass</i>	15	kg

Table 20 Horizontal Speed Limitation according to configuration 2

The camera's data collection and processing frequency derives from common values (private conversation with AIKO: Autonomous Space Mission).

The rotation time depends on the system's inertia matrix and the torque generated by the attitude control system motors.

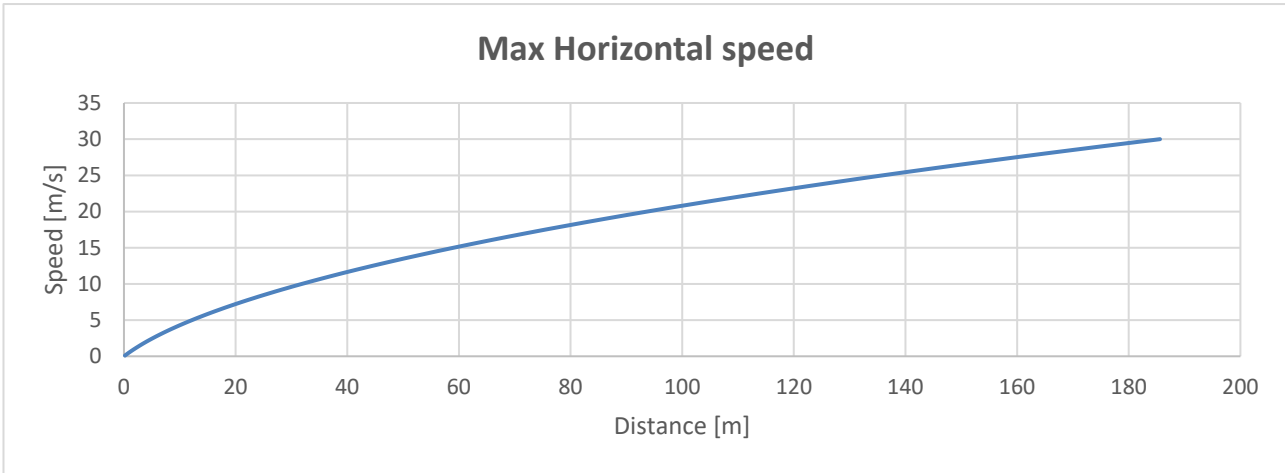


Figure 28 Max Horizontal Speed according to the configuration 2

4.12 Mapping time required

This LiDAR has a very limited FOV, this implies some limitations on the detection distance, but it also brings us advantages in terms of data processing speed thus reducing the hovering time that would be necessary with the other LiDAR. Furthermore, having a very high sampling speed, it is possible to map during the descent, thus having a continuous updating of the data and more precision in navigation [annex AD_10].

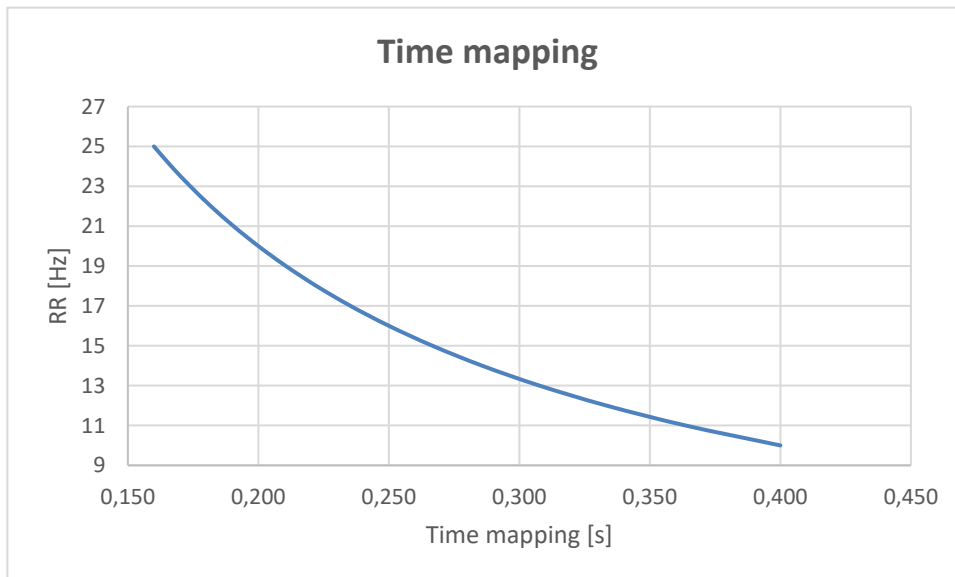


Figure 29 Time required to map while using LiDAR

Obviously the time needed to map varies depending on the sampling frequency. Considering the maximum frequency we obtain a mapping time of 0.160s which is considerably less than what would be necessary considering a 3D LiDAR with a higher vertical FOV. This type of 3D LiDAR would be necessary in case you want to continue the mission and venture into the cave. Moreover, the information necessary for navigation in that type of mission is much higher, such as the level of control and maneuvers required.

4.13 Distance error estimation

As already mentioned previously, the extremely limited vertical FOV limits the detection field and this affects the minimum distance at which we can approach the ground without running the risk of not perceiving an obstacle [annex AD_10].

Being that our drone has a requirement to be 12U in size. The simplest configuration thought is a 20x20x30cm cube. The face facing the ground is 20x20cm and therefore this dimension has been taken as a minimum to characterize the limit distance.

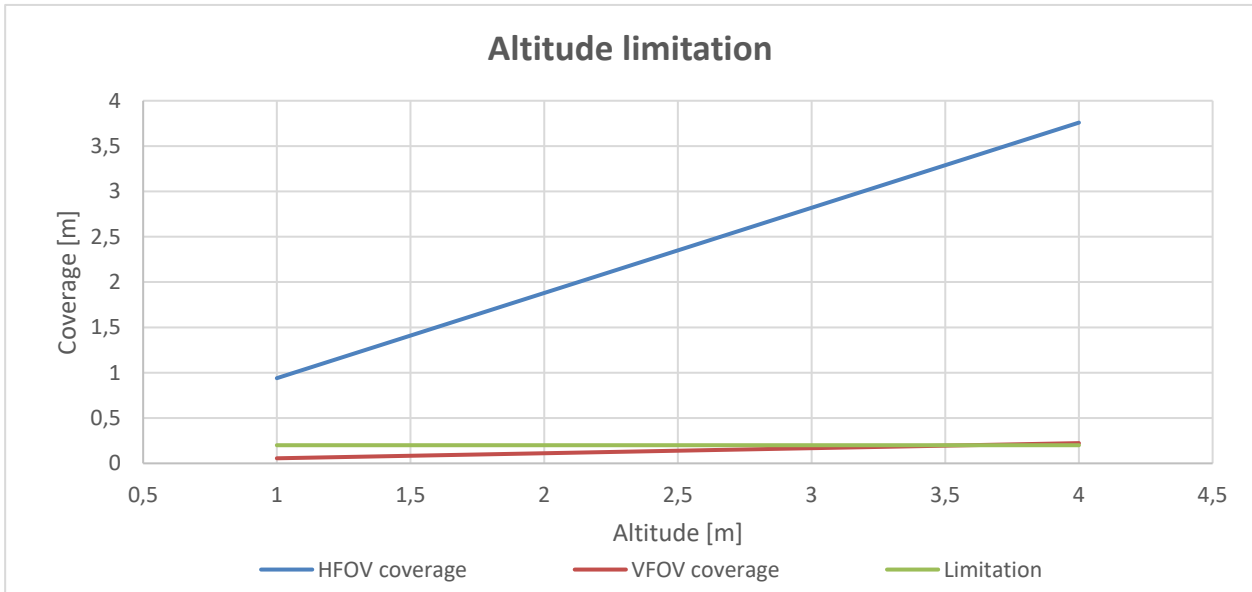


Figure 30 Comparison between HFOV and VFOV of the LiDAR scanning area

Therefore through HFOV and VFOV the two maximum mapping dimensions were found as a function of distance and obviously, being the VFOV much lower, he will have the most stringent limitation.

As you can see the maximum altitude is about 3.6 meters this is actually not a limitation as staying too close to the ground can cause problems with dust and is not recommended.

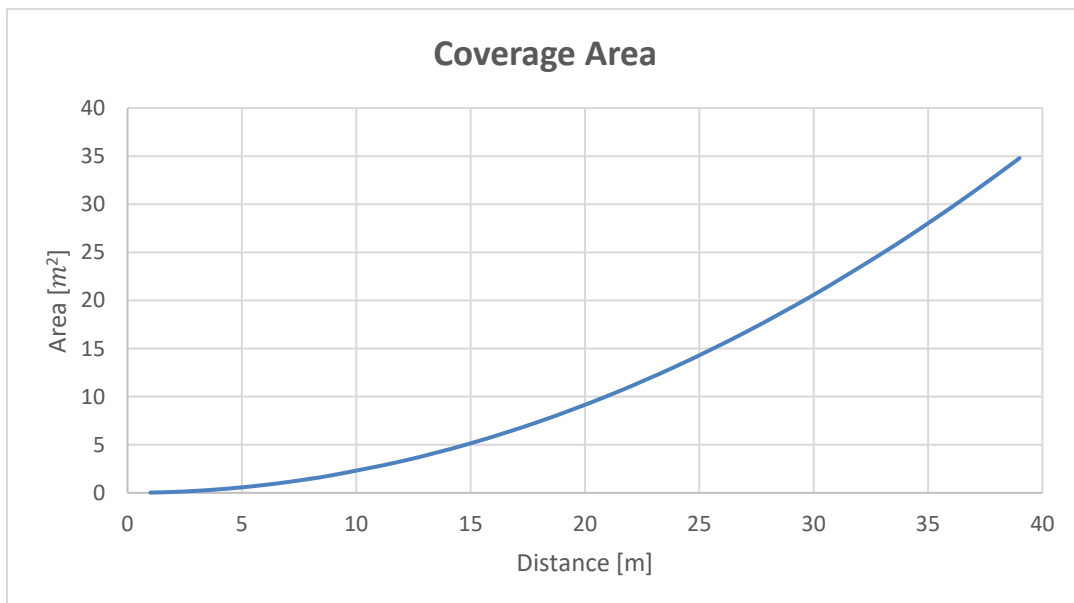


Figure 31 LiDAR scan coverage area as a function of distance from walls

4.14 Battery consideration

Considering the indicative data provided by the EPS [13] for state of practice lithium primary batteries for space use, it is possible to estimate the characteristic dimensions required to power the navigation system in the two illustrated configurations [annex AD_14].

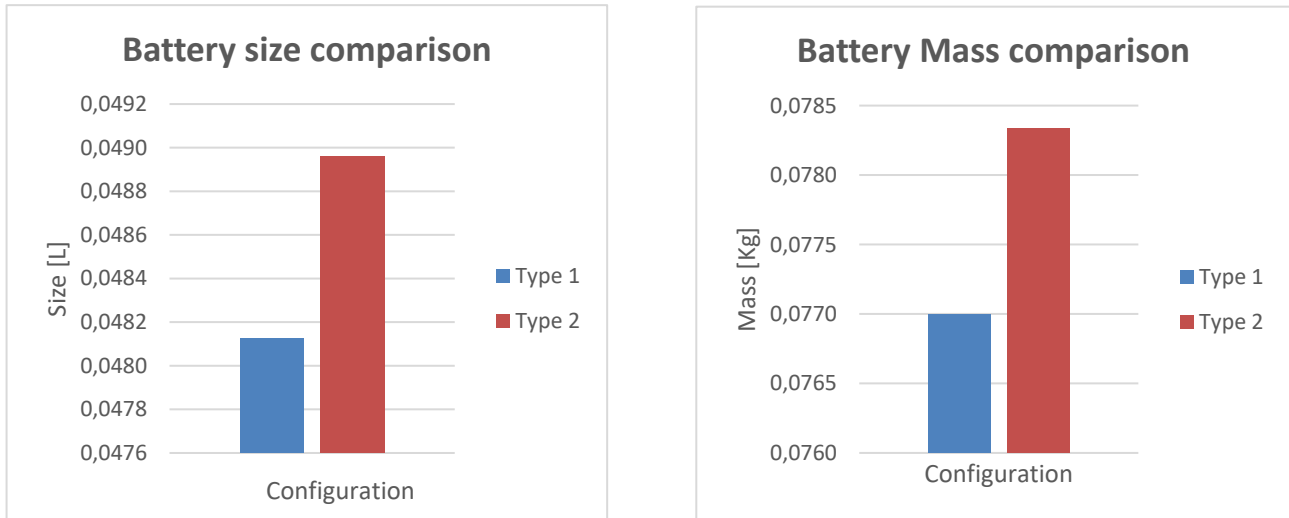


Figure 32 Comparison between the masses and the dimensions of the custom batteries needed to power the navigation system in the two configurations.

The difference in masses and dimensions is really minimal, this is because the energy consumption is very similar between the two configurations.

4.15 Comparison

The first considerations can be made taking into account the main characteristics that are required: mass, dimensions and power [annex AD_10].

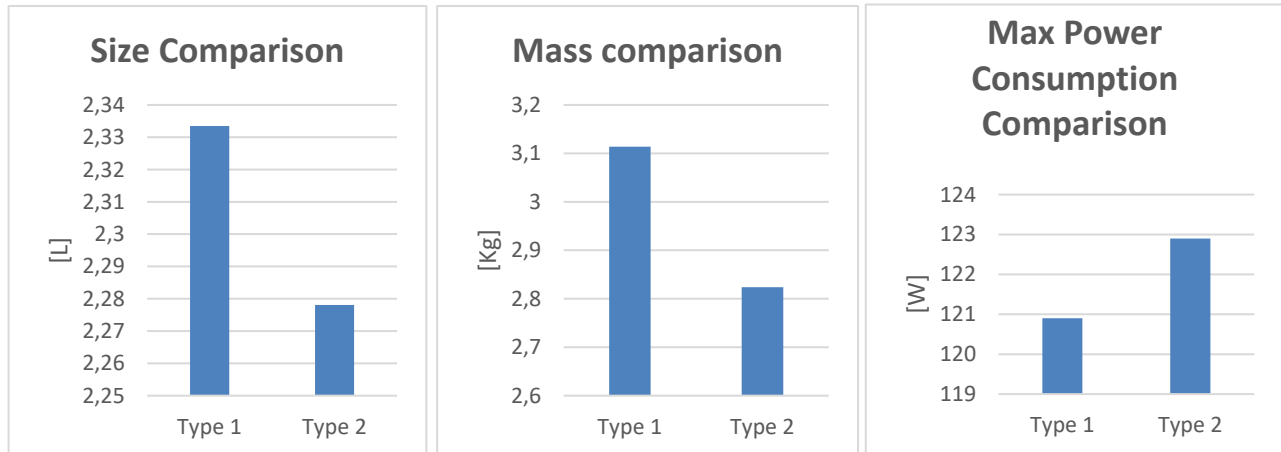


Figure 33 Comparison of mass, power, dimensions between the two configurations

As you can easily see the type 2 configuration, that is the one with double LiDAR, requires both dimensions and lower masses and only a few watts more of power.

This leads us to think that it is the best choice, moreover the type 1 configuration has the defect of not being able to identify the underlying environment well, the laser altimeter only provides us with a measurement of the precise distance from the bottom. Any obstacle not far from the altimeter measurement could impact on the drone, moreover the descent is mainly done with the integration of the data provided by the IMU and this leads to a cumulative error that will surely make us move from the optimal flight plan.

To conclude, the type 1 configuration does not give constructive and structural advantages and is also decidedly inferior in terms of navigation safety, for this reason the type 2 configuration was chosen.

Looking to the future, to navigate autonomously in a tunnel, i.e. the continuation of the mission, a double LiDAR configuration is certainly necessary which would differ from the type 2 one only for the LiDAR along z which must be able to provide more information, to this reason would need two with a 360 ° viewing angle.

4.16 Mission plan Power Consumption

Thanks to the data provided by the flight plan, it was possible to estimate consumption as a function of the time taken in the various flight phases. This type of analysis allows us to estimate the real power required to power the navigation system and which configuration is most suitable.

	<i>Phase</i>	<i>Duration [s]</i>	<i>Power [W]</i>
Phase A	Take off and hovering	13,48	27,5
Phase B	Crater approach	25,67	27,5
Phase C	Hovering and mapping	0,5	27,5
Phase D	Descent	17,2	33,3
Phase E	Hovering and photo	10	117,5
Phase F	Ascent and hovering	22,02	33,3
Phase G	Rover approach and mapping	25,32	27,5
Phase H	Landing	8	37,5

Table 21 Description of the various phases of the mission with the times and energy consumption inherent to the navigation system

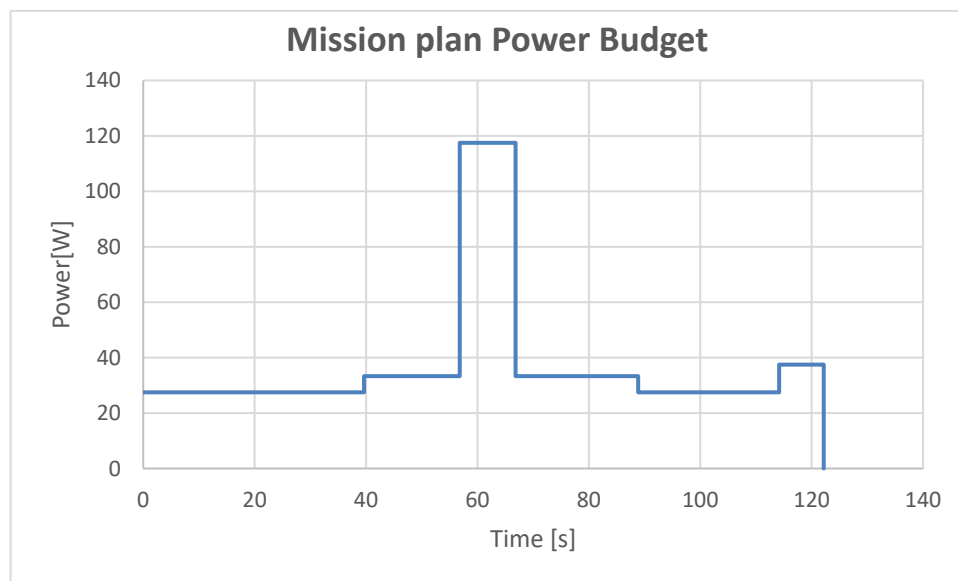


Figure 34 Power budget of the navigation system

As can be seen from the graph above, there is only a small period of time when the energy consumption needed by the navigation system is extremely high. This peak is possible to address thanks to the characteristics of the batteries provided by my colleague who studied EPS or maybe some capacitors [13].

5 Indoor Navigation – Preliminary evaluation

The next step is navigation in the tunnel, it is required a mapping of the surrounding environment and being able to move with 6 DOF.

In this regard it was decided to analyze two possible configurations: LiDAR and Visual Odometry.

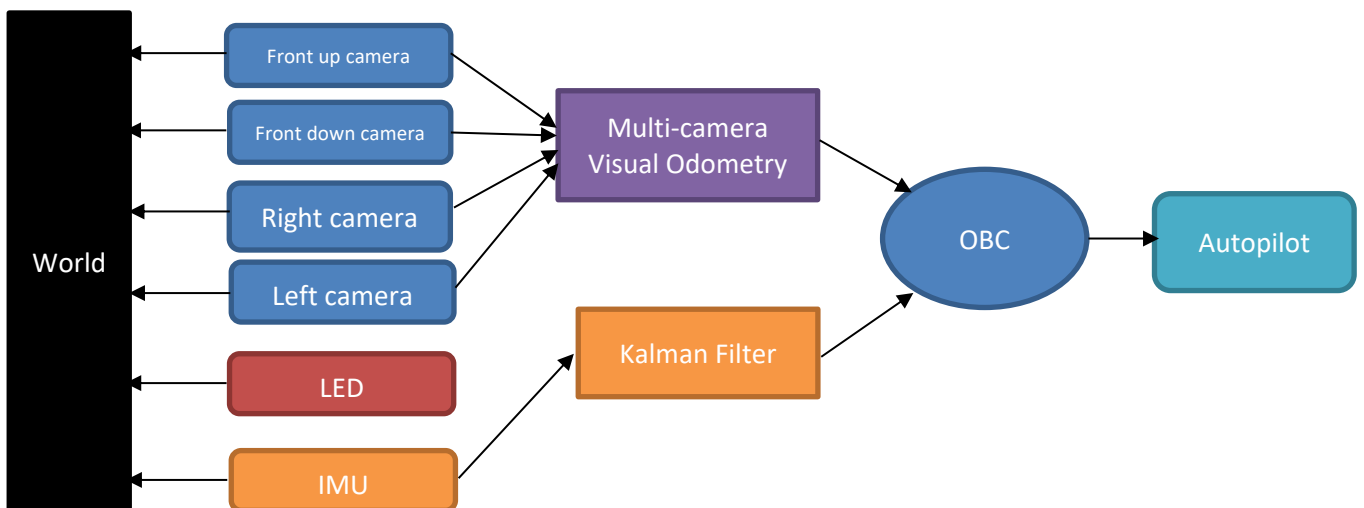
5.1 Visual Odometry

5.1.1 Configuration

To be able to face navigation in an environment without a previous map, the system must be equipped with 4 cameras, two front and two laterals. Also being in a dark environment it is necessary to illuminate it, so the system must be equipped with LEDs that must be able to illuminate sufficiently in the various directions of the cameras.

The problem of constant illumination of the environment leads to the problem of cooling and therefore the addition of mass to be able to cool the LEDs.

Finally, the estimation of the position through the cameras is continuously compared with the data provided by the IMU through a Kalman filter.



5.1.2 Lighting

To be able to perceive an image with the cameras, a minimum background lighting is necessary and this condition depends on the distance we are at and the FOV we want.

In accordance with this it was possible to make an analysis of the power needed as a function of distance. The chosen FOV is 60 ° due to considerations which will be explained later [annex AD_11].

The chosen LED provides 8000 lumens and through the FOV it is possible to obtain the angular span and then Flux [133].

$$\Omega = 2\pi \left(1 - \cos\left(\frac{FOV}{2}\right) \right)$$

$$Flux = \frac{Lumen}{\Omega \cdot distance}$$

The minimum level of illumination supposed to be 100 Lux, which in accordance with the tables is decidedly low [134].

Activity	Illumination on task surface(lux)
Full moon at tropical latitudes	1
Public areas with dark surroundings	20 - 50
Typical family room setting	50 - 100
Overcast day or short visit work area (storage rooms)	100 - 150
Light Office Work, Classroom	250
Heavy Office Work, CAD Work, Library, Shops, Laboratories	500
Supermarkets, Mechanical Workshops	750
Normal Drawing Work, Studio Work, Quality control	1,000
Detailed and Precision Type Work	1500 - 2000
Performance of visual tasks of low contrast and very small size for prolonged periods of time	2000 - 5000
Performance of very prolonged and exacting visual tasks	5000 - 10000
Performance of very special visual tasks of extremely low contrast and small size	10000 - 20000

Table 22 Lighting levels of various environments [134]

Despite the minimum requirement, the energy consumption to illuminate is not negligible, but rather very demanding for a drone of our size, only 12 U.

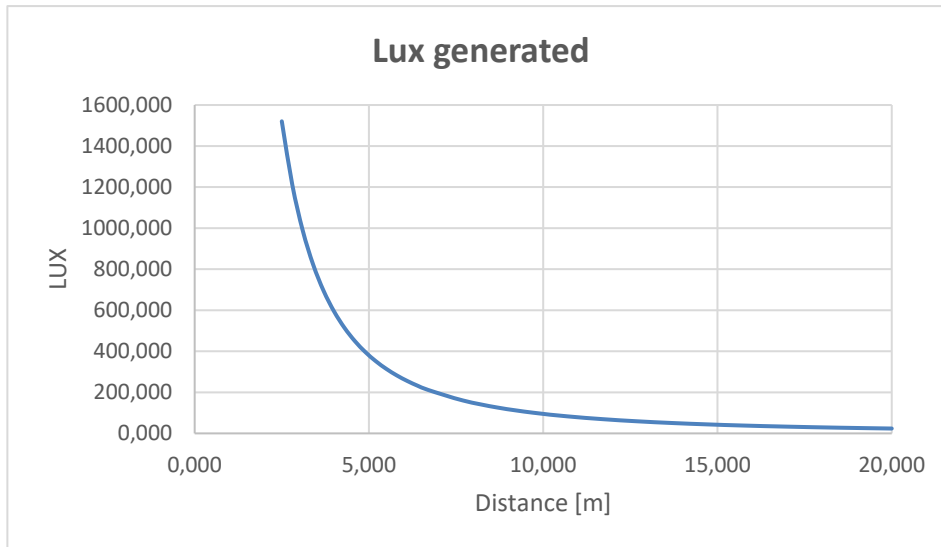


Figure 35 Lux generated with an 80W LED depending on the distance from the walls

5.1.3 Figures of merit

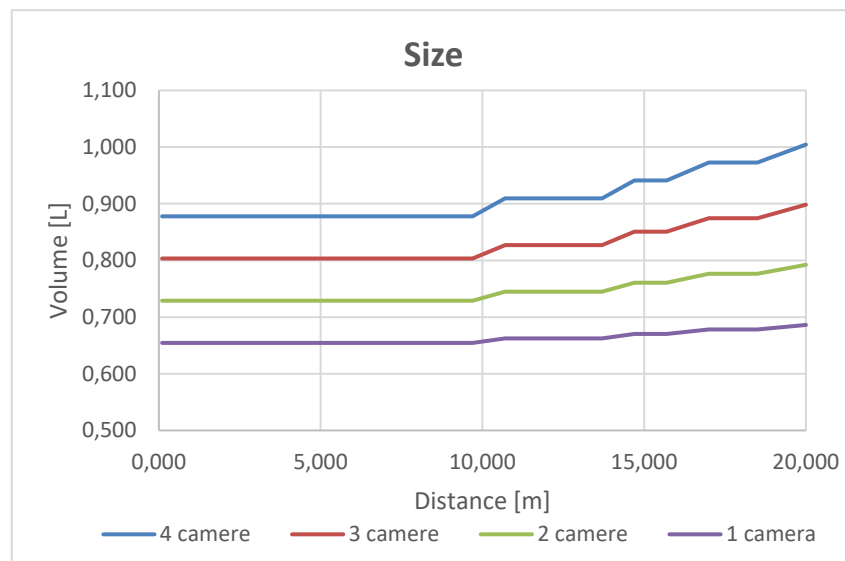


Figure 36 Comparison between the required sizes of the different configurations according to the number of cameras and the distance from the walls.

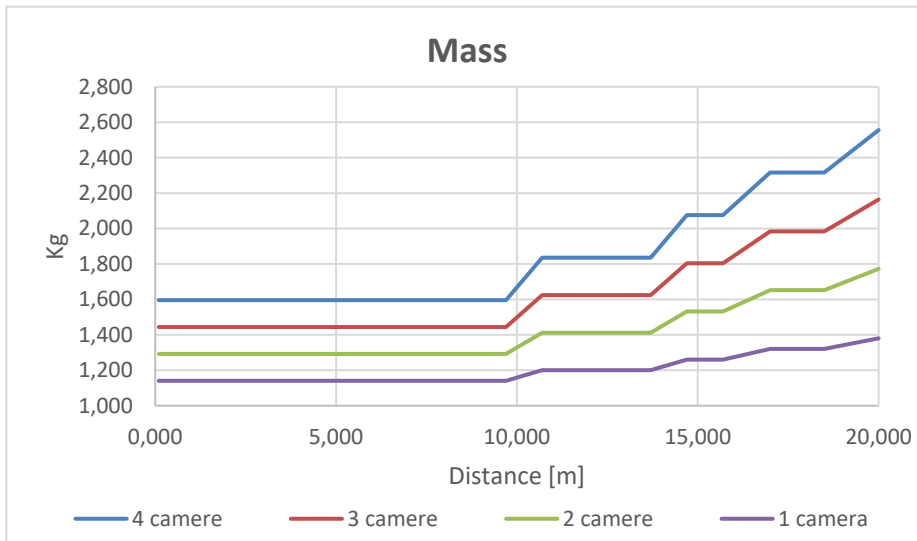


Figure 37 Comparison between the required masses of the different configurations according to the number of cameras and the distance from the walls.

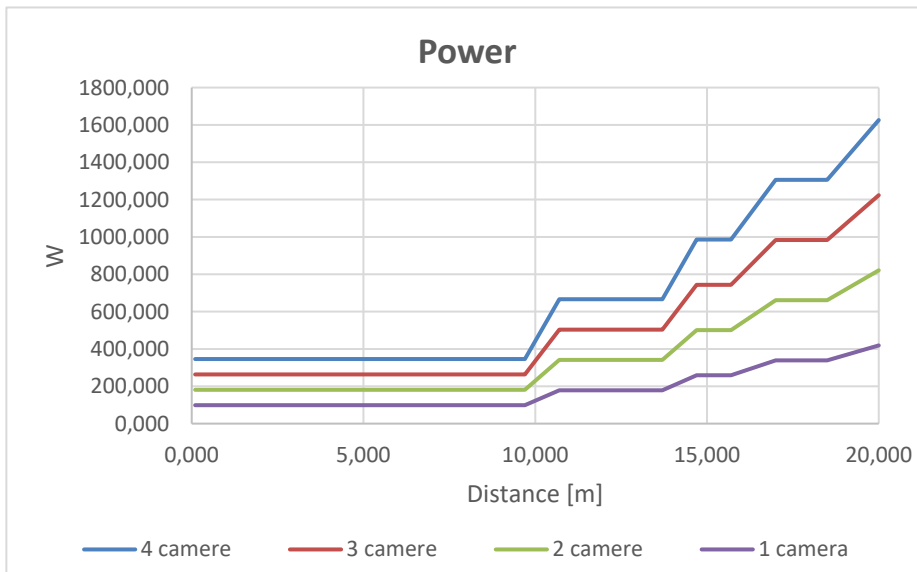


Figure 38 Comparison between the required powers of the different configurations according to the number of cameras and the distance from the walls.

As you can see, the comparison was made taking into account various configurations as the number of cameras varies.

The most stringent parameter is the power, and the bottleneck is 10 meters away, in fact, once that limit is exceeded, the required power increases as it is necessary to add LEDs to meet the minimum lighting requirement.

This is the first limitation of this solution and obviously also involves limitations on the maximum speed and therefore an increase in consumption.

5.1.4 Algorithm Speed consideration

Speed is certainly an important aspect for consumption, the faster you go the less you consume, so less fuel is needed and the drone is lighter and less bulky. But what are the parameters that most influence the maximum speed?

Initially, the major limitation was thought to be the real-time data processing speed of the navigation algorithm, an analysis was carried out to validate this hypothesis [annex AD_11].

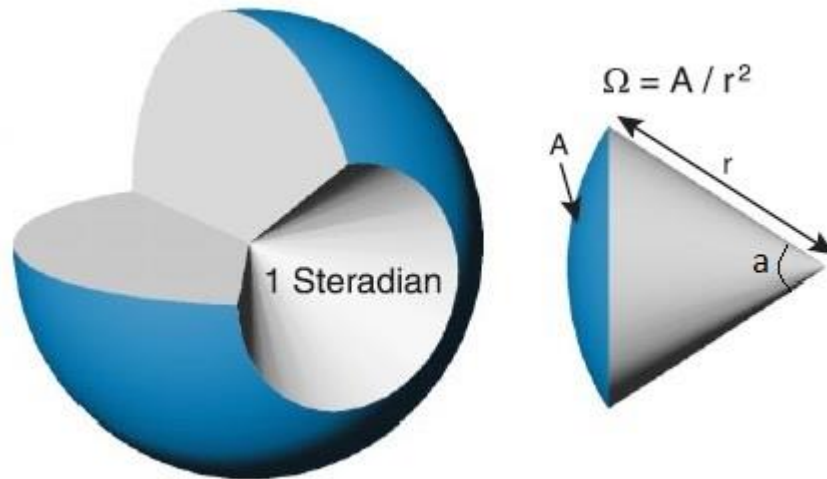


Figure 39 Representation of the aperture cone of visibility in 3D space [140]

The navigation algorithm schematizes the image in reference points such as edges or corners, then superimposes the next image on the previous one and comparing when the images overlap it is able to determine speed and position with respect to the two shots.

In this analysis the percentage of overlap was chosen of 50% which is sufficiently conservative as due to external problems such as shadows, dust and the camera may miss some frames.

Furthermore, agreeing with the previous analysis of the lights, the FOV was chosen at 60 °.

The first analysis takes into account how the data processing speed affects the maximum speed of the drone. at a fixed distance of 10m:

$$V_{max} = \frac{2d \cdot \tan\left(\frac{FOV}{2}\right) \cdot \%sovrapposition}{\frac{1}{10}}$$



Figure 40 Maximum speed according to the refresh rate with a distance from the walls set at 10m.

The second analysis instead compares how the distance affects the maximum speed with a data processing speed set at 10Hz:

$$V_{max} = \frac{\left(2 \cdot 10 \cdot \tan\left(\frac{FOV}{2}\right)\right) \cdot \%sovrapposition}{\frac{1}{RR}}$$

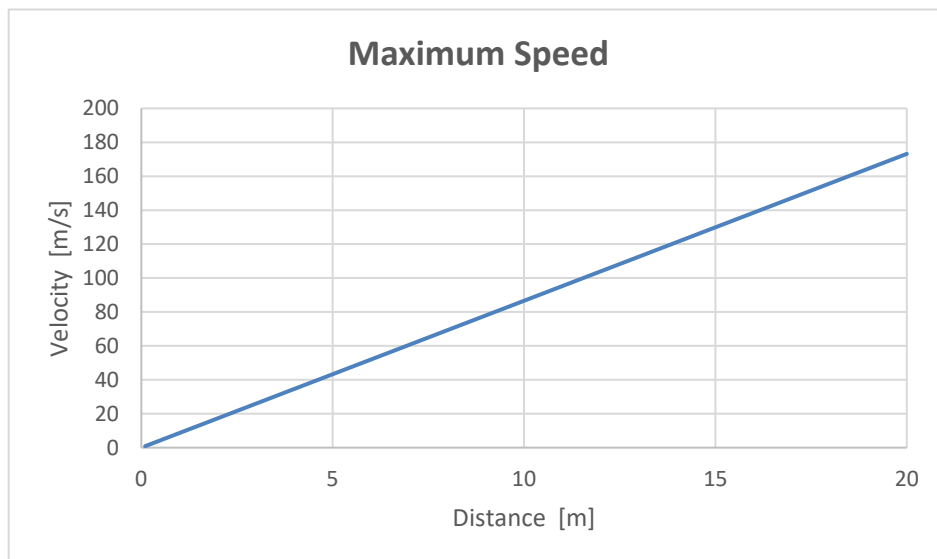


Figure 41 Maximum speed as a function of distance with a refresh rate set at 15Hz.

the hypothesis of 15Hz processing of data in real time derives from literature and other projects, where it is easy to reach even 20Hz [135].

Despite all these limitations we will have a very high theoretical maximum speed, around 60 m/s, this speed would certainly not be a limitation in our configuration, as can be seen in the trajectory study [13].

5.1.5 Thrusters speed limitation

Another limitation on speed is certainly due to the thrusters, in fact our navigation system must be able to perceive an obstacle, process the information, send it to the propulsion system and be able to stop before going to impact [annex AD_11].

Being that our maximum visibility is 10m, the limitation is very narrow.

<i>Horizontal Thrust</i>	1	N
<i>Drone Mass</i>	15	kg
<i>% sovrapposition</i>	50%	
<i>Refresh Rate</i>	10	Hz
<i>FOV</i>	60	deg
<i>Distance</i>	10	m
<i>Delay of the valve</i>	0,050	s
<i>Delay of the truster</i>	0,100	s
<i>Delay of the algorithm</i>	0,100	s
<i>Delay</i>	0,250	s

Table 23 Summary table of parameters used to estimate speed limits in the configuration with visual navigation.

By imposing the final speed equal to 0 it is possible to find the maximum speed that allows us to stop within 10 meters.

$$s = \frac{v^2 - v_0^2}{2a} \quad \rightarrow \quad s = \frac{v^2 - v_0^2}{2 \cdot \frac{T}{m}}$$

to consider the various delays, the space covered during the delay was added and the maximum speed allowed was recalculated

$$s_{delay} = t_{delay} \cdot v_0; \quad t_{delay} = t_{algorithm} + t_{truster} + t_{rotation}$$

$$Distance = s_{delay} + s$$

in this study it was considered an engine with a thrust of 1N to stop us, which would be the engines used for attitude control, furthermore, the assumption of keeping the mass constant is conservative.

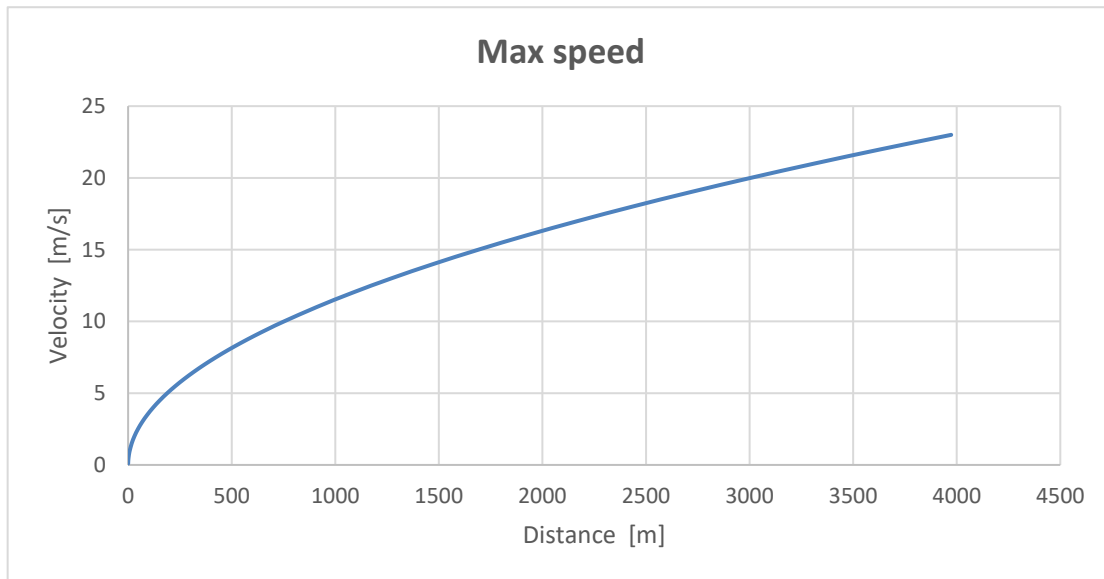


Figure 42 Maximum speed allowed for navigation in caves according to the distance from the walls, with 1N of thrust provided by the auxiliary engines.

As you can see at a distance of 10 meters the speed is very low, just over 1 m/s, this limitation is definitely the most stringent.

To improve the speed the options are to increase the power of the thrusters or change the configuration, perhaps by rotating the main thruster.

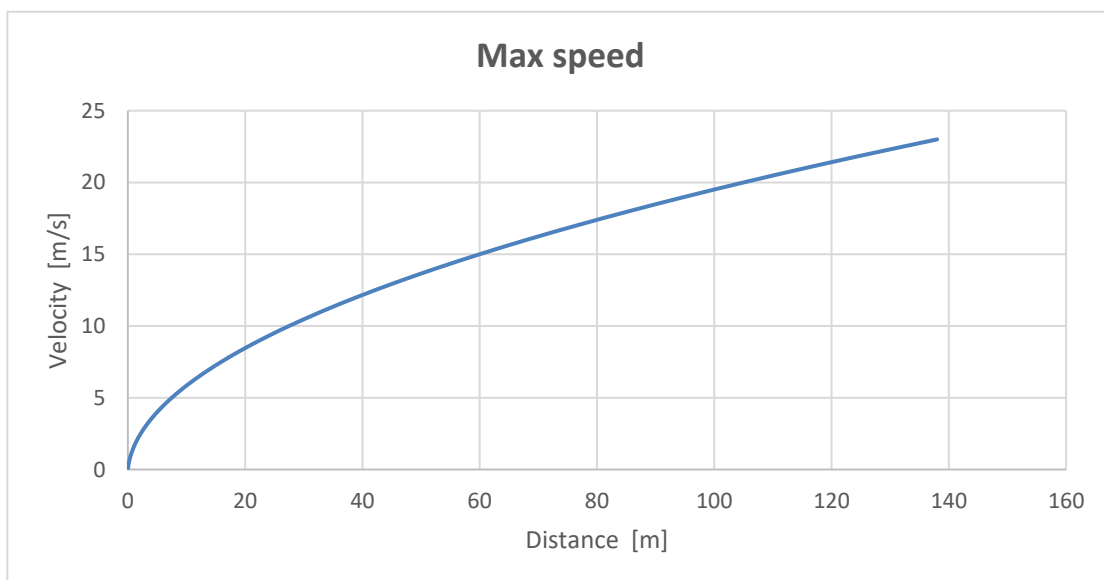


Figure 43 Maximum speed allowed for cave navigation according to the distance from the walls, with 30N of thrust provided by the auxiliary engines.

By increasing the thrust to 30N, the maximum speed allowed is considerably increased, but obviously this significantly affects the masses and dimensions of the propulsion system. A subsequent analysis will certainly be needed to verify this trade off.

On the other hand, the second option to rotate the drone excessively complicates navigation using visual odometry, excessively reducing reliability and increasing errors.

5.1.6 Power consumption

The most stringent part on consumption is lighting. A solution to reduce consumption could be to use a duty cycle on the activation of the LEDs according to the cameras [annex AD_11].

Camera exposition time	0,037	s
Minimum led pulse duration	0,010	s

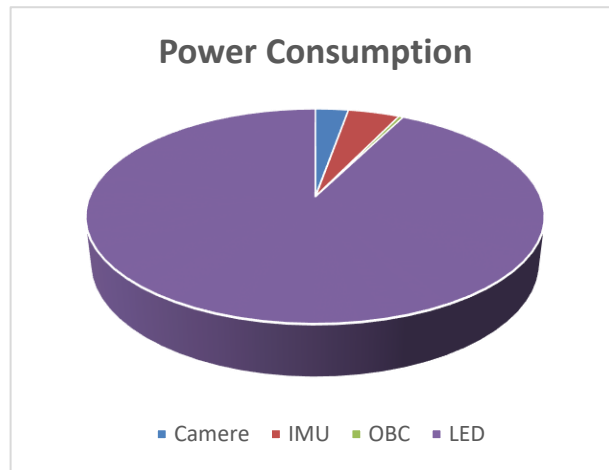


Figure 44 Graphing of the energy consumption levels due to the various components necessary for navigation in this configuration.

Obviously, even here it is a question of trade off, the higher the sampling frequency and the less time you can turn off the lights, furthermore a limitation is the maximum speed of switching on of the LEDs and the exposure time needed by the camera.

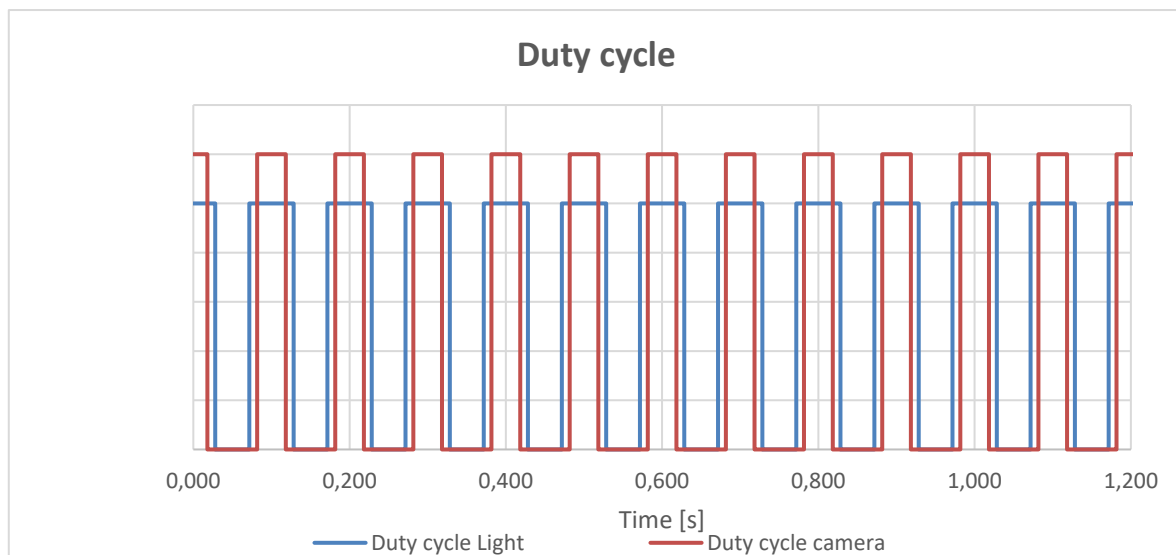


Figure 45 Graphic representation of the Duty Cycle, assuming a refresh rate of 10Hz, of the LEDs and the camera considering the minimum ignition times of the respective components previously analyzed.

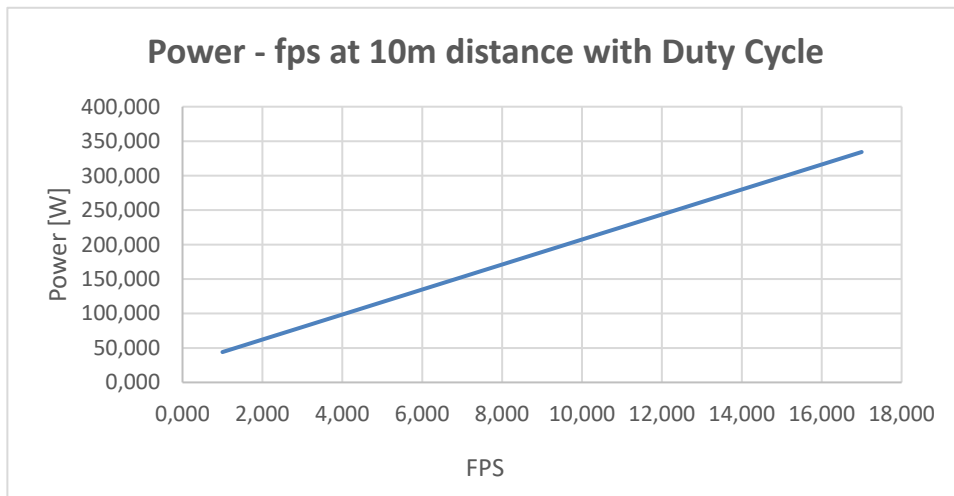


Figure 46 Representation of the energy consumption as a function of the refresh rate using the DC technique, withstanding a distance from the walls set at 10m.

Finally, it is possible to make a comparison on consumption with and without the use of the DC technique. It is important to note that saving in energy consumption also affects masses and dimensions. This is because it limits the size of the batteries.

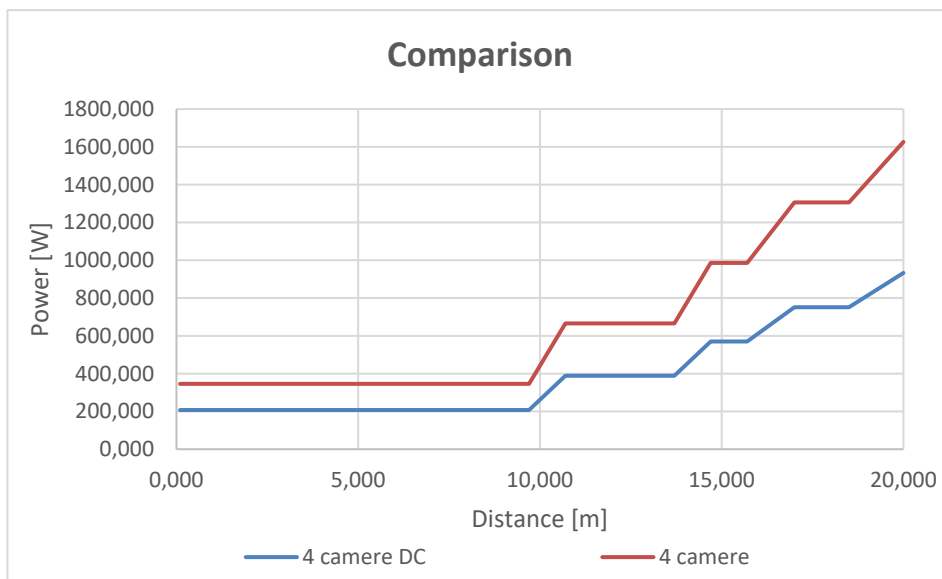


Figure 47 Comparison between the energy consumption of the configuration with DC and the one without.

Using a frequency of 10Hz the saving is just over 40%, this makes the method more easily feasible.

5.2 Led Heat dissipation

To dissipate the heat of the LEDs, classic radiators with fins are not suitable as there is no atmosphere, the heat exchange by convection does not occur. The greatest heat exchanged is that for radiation and also that to heat the structure.

LEDs, when current passes through the junction of the semiconductor chip, generate visible light. However, the efficiency of the LEDs is not 100%, much of their power is emitted as heat and therefore it is necessary to dissipate it. Assuming a conservative case, we can assume that LEDs convert 25% of the input power into light and that they emit 75% of the input power as heat. This estimate varies with current density, brightness, and component, but is a good estimate for thermal design.

Next is an equation showing how to calculate the heat output.

$$P_t = 0,75 \cdot V_f I_f$$

Where:

P_t is the thermal power (W)

V_f is the forward voltage of the LED (V)

I_f is the source current to the LED (A)

The V_f and I_f can be measured directly or calculated from the PCT, so the thermal power can easily be calculated. This is the amount of power the system/heat sink must dissipate [136].

5.2.1 Conduction

Conduction is the main method of heat transfer and consists of the transfer of heat through a solid material by direct contact. This is the main transfer mode for obtaining thermal power from the junction of the LED to the heat sink. Metals are typically the best conductors of heat. Fourier's law allows to calculate the amount of heat transferred by conduction. The thermal conduction potential of all materials can be expressed as thermal conductivity, and is typically shortened to k [136].

$$Q_{cond} = -k A \frac{\Delta T}{\Delta x}$$

Where:

Q_{cond} is the amount of heat transferred through conduction (W)

k is the thermal conductivity of the material (W/mK)

A is the cross sectional area of the material through which the heat flows (m^2)

ΔT is the temperature gradient across the material ($^{\circ}C$)

Δx is the distance for the heat must travel (m)

5.2.2 Radiation

The radiation resulting in the transfer of thermal energy through an electromagnetic field is the second and last component of the heat transfer in space. The amount of heat transfer of the radiation is based on the emissivity of the material, which is the ratio of how close the surface comes to a black body.

Typically this contribution is very small on the net heat transfer of the system as the surface areas are typically quite small and the surface temperatures are relatively low. This is because the LED junction must be maintained at a maximum nominal temperature below 150 °C. The following equation shows how to calculate the amount of heat transferred by radiation [136].

$$Q_{rad} = \varepsilon \sigma A (T_s^4 - T_f^4)$$

Where:

Q_{rad} is the amount of heat transferred through radiation (W)

ε is the emissivity of the surface (dimensionless)

σ is the Stefan-Boltzmann constant ($5,67 \cdot 10^{-8} \text{ W/m}^2 \text{ K}^4$)

A is the surface area (m^2)

T_s is the surface temperature of the material (°C)

T_f is the fluid temperature of the medium (°C), typically referenced to the ambient air temperature

5.2.3 Thermal model

One way to schematize the thermal path of an LED system can be represented with a simple resistor network similar to an electrical circuit.

Thermal resistances are represented by resistors, the heat flow is approximated by the electric current and the corresponding temperatures within the system correspond to the electrical voltages.

where:

T is the temperature at each corresponding location (°C)

θ_{ab} is the thermal resistance from point a to point b (°C/W)

n is the number of LED components on a single PCB

Heat is conducted from the LED junctions through the LED components to the PCB, through the thermal interface material (TIM) to the heat sink and then conveyed and radiated to the ambient air.

The individual sections within the system are represented by nodes in the circuit and are the locations where temperatures can be measured.

The resistances represent the thermal resistances of the individual contributors. For example, θ_{j-sp} represents the thermal resistance of the LED component from junction to solder point.

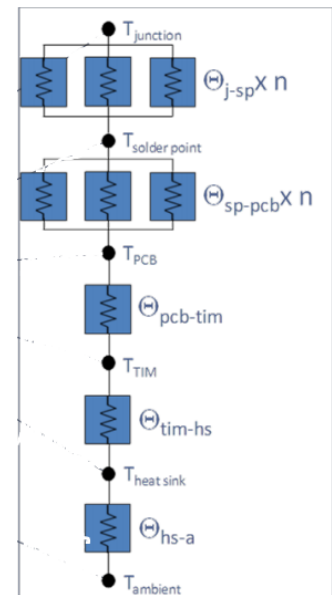


Figure 48 Thermal circuit of an LED array

The individual thermal resistances described above can be calculated by the equation below.

$$\theta_{ab} = \frac{T_a - T_b}{P_t}$$

where:

- θ_{ab} is the thermal resistance from point “a” to point “b” ($^{\circ}C/W$)
- T_a is the temperature at point “a” ($^{\circ}C$)
- T_b is the temperature at point “b” ($^{\circ}C$)
- P_t is the thermal power as calculated before

The thermal resistance of the entire system can also be compared to an electrical circuit in series, where the system thermal resistance can be calculated as shown below.

$$\theta_{sys,az} = \theta_{ab} + \theta_{bc} + \dots + \theta_{yz}$$

where:

- $\theta_{sys,az}$ is the system thermal resistance from point “a” to point “z” ($^{\circ}C/W$)
- θ_{ab} is the thermal resistance from point “a” to point “b” ($^{\circ}C/W$)
- θ_{bc} is the thermal resistance from point “b” to point “c” ($^{\circ}C/W$)
- θ_{yz} is the thermal resistance from point “y” to point “z” ($^{\circ}C/W$)

In an LED system, the total system-level thermal resistance is typically defined as “junction to ambient”, or θ_{ja} . This quantifies how well each component transfers thermal power [136].

5.2.4 Thermal stack

To perform a thermal analysis, an LED system typically consists of a multi-component assembly called a thermal stack. Taken together, all components contribute to a varying extent to the total thermal performance of the system. Typically the LED is soldered to a PCB, with a metal core or FR4, which is usually connected to a heat sink. To maximize the heat transfer between the heatsink and the PCB it is essential to have a good TIM to fill any air gaps. The best approach to optimizing the thermal path is usually to minimize the number of materials in the thermal stack and use the most thermally conductive materials available.

5.2.5 Component

It is possible to estimate the amount of heat based on the measured TSP and the thermal resistance of the LED.

$$T_j = T_{sp} + \theta_{th}P_{total}$$

where:

- T_j is the junction temperature ($^{\circ}C$)
- T_{sp} is the measured solder point temperature ($^{\circ}C$)
- θ_{th} is the thermal resistance of the component ($^{\circ}C/W$)
- P_{total} is the total power (W) input to the LED ($I_f \cdot V_f$)

Usually all LEDs should not exceed their maximum junction temperature which is usually around 150 $^{\circ}C$.

5.2.6 Thermal interface material

In the thermal interface the material plays an important role, regarding the thermal performance of the system, this varies according to the design choices made. TIMs are critical to minimize the air gaps between the heatsink and the PCB. The TIMs allow to have a thermal interface between the PCB and the heat sink and also, depending on the application, they can have other functions. For example, they can perform the function of electrical insulation or the creation of a mechanical connection. Usually various types of TIMs are used in LED systems, including greases, tapes, pads and epoxies. Each has its advantages and disadvantages depending on the application.

TIM	Property					
	Bulk Conductivity	Thermal Resistance	Bond Line Thickness	Production Automation	Reworkability	Stress Relief
Adhesive films	Good	Poor	Fair	Fair	Poor	Fair
Adhesives	Good	Good	Excellent	Excellent	Poor	Fair
Compounds	Good	Excellent	Excellent	Excellent	Good	Excellent
Encapsulants	Excellent	Good	Good	Excellent	Good	Good
Gap fill pads	Excellent	Fair	Poor	Fair	Excellent	Good
Gels	Good	Good	Good	Excellent	Good	Excellent
Phase changes	Excellent	Excellent	Fair	Excellent	Good	Excellent

Table 24 *Relative properties of TIMs, advantages and disadvantages.*

A large number of parameters must be considered when choosing a TIM, not just thermal conductivity. Normally the material seam thickness is neglected, but, as shown in the equation below, the thermal resistance of the material is highly dependent on this thickness.

These basic characteristics are provided by the manufacturer TIM on its technical data sheet.

It is important to understand how all the features interact and decide which is the most important for each specific application.

It may happen that a thinner TIM with poor thermal conductivity has a lower thermal resistance than a thicker TIM with better thermal conductivity.

It is important that both of these attributes are considered when selecting a TIM and their relative effects can be quantified with equations. However, although a TIM may have better thermal conductivity than air, its conductivity will not be as good as that of metal, so the approach of adding material between metal components is wrong, but rather one can think of filling the voids, which are typically occupied by the air. The important thing to remember is that the thinner the better!

$$\theta_{tim} = \frac{L}{kA}$$

where:

θ_{tim} is the thermal resistance of the TIM

L is the thickness of the TIM (m)

k is the thermal conductivity of the TIM ($W/m K$)

A is the contact area (m^2)

5.2.7 Heat sink

The heat sink is the last and most influential part of the thermal stack and is needed first to conduct heat away from the LEDs and then to channel and radiate heat into the ambient air, unfortunately this second point is not needed for our application. Therefore, the first key point of the heat sink is that it is manufactured with a high thermal conductivity material so that it can conduct heat away. The second point is that the heat sink has a large surface area to convey heat into the environment and also has good emissivity so that it can radiate the heat.

In our application, however, the convective part does not have a reduced impact. In some cases, heat sinks are paired with other heat dissipation devices such as housings, enclosures, etc.

In the table below you can see the thermal conductivity of some common materials and an approximate range of their emissivity, which can vary significantly depending on the finish of the material. The choice of the highest thermal conductivity and / or emissivity is obviously not always possible due to other factors that must be considered such as weight, cost and manufacturability. Each of these must be evaluated for each application to determine the best material and manufacturing process.

Cast or forged aluminum is typically used for heat sinks. The anodizing of aluminum gives the heat sink a much higher emissivity (up to about 0.8) than standard aluminum and aids in the transfer of radiative heat into the environment [136].

Material	Thermal Conductivity (W/m K)	Approximate Emissivity
Acrylic	0.2	0.94
Air	0.024	Not applicable
Aluminum	120 - 240	0.02 - 0.9 (depending on finish)
Ceramics	Alumina: 15 - 40 Aluminum nitride: 100 - 200	0.4 - 0.7 0.9
Conductive polymers	3 ~ 20	Not applicable
Copper	401	0.05 - 0.8 (depending on finish)
Diamond	2000	1.0
FR4	0.2	0.7 - 0.8
Glass	1.05	0.6 - 0.97
Silicon	150	0.6
Silicon carbide	350	0.85
Silver	429	0.02 - 0.074
Stainless steel	16	0.1 - 0.9 (depending on finish)
Thermal grease/epoxies/pads	0.1 ~ 10	Not applicable
Water	0.58	0.85 - 0.99
Wood	0.17	0.8 - 0.9

Table 25 Thermal conductivity and emissivity for various materials at 25°C

Heat sink design can be very complicated and limited by many restrictions such as space constraints, cost, weight, manufacturability and countless other requirements. There is no one right answer to heat sink design and each application must be approached on a case-by-case basis, but the following general guidelines can help in the design process.

- A rough estimate of approximately 5-10 in^2 of heat sink surface area per watt of heat can be used for a first-order estimate of heat sink size.
- Choose a material that has good thermal conductivity to spread heat away from the LEDs.
- Use high surface emissivity heat sinks to maximize thermal radiation heat transfer. Anodizing dramatically increases the emissivity of an aluminum heat sink.

- Passive (natural convection) heat sinks are always preferred for many reasons, but if appropriate, actively cooled heat sinks can significantly improve performance.
- Use of thermal modeling can alleviate repetitive prototyping and indicate design deficiencies and potential areas of improvement early in the design process.

A key part of the heatsink design to consider is the manufacturing method that will be used. These methods vary significantly and can produce hugely different heat sinks, which can serve different applications and their specific needs [136].

Heat Sink Aspect	Bonded	Cast	Extruded	Folded	Forged	Skived	Stamped
Maximum fin height	6.0 in	3.0 in	3.0 in	2.0 in	5.0 in	1.5 in	2.0 in
Minimum fin thickness	0.032 in	0.070 in	0.040 in	0.010 in	0.020 in	0.016 in	0.007 in
Maximum aspect ratio	60:1	10:1	10:1	40:1	35:1	16:1	4:1
Type	Straight	Any	Straight Cross-cut	Straight	Any	Not perfectly straight	Straight
Cooling factor	0.8x	1.4x	x	0.7x	1.5x	1.2x	1.4x
Base cost factor	1.3x	0.8x	x	1.2x	1.3x	1.2x	0.7x
Tooling cost factor	1.5x	4.0x	x	1.8x	3.0x	1.2x	2.8x
Material type	Al6063 Cu1100	Al356	Al6063	Al6063 Cu1100	Al6063 Cu1100	Al6063 Cu1100	Al6063 Cu1100

Table 26 Heat sink manufacturing process comparison

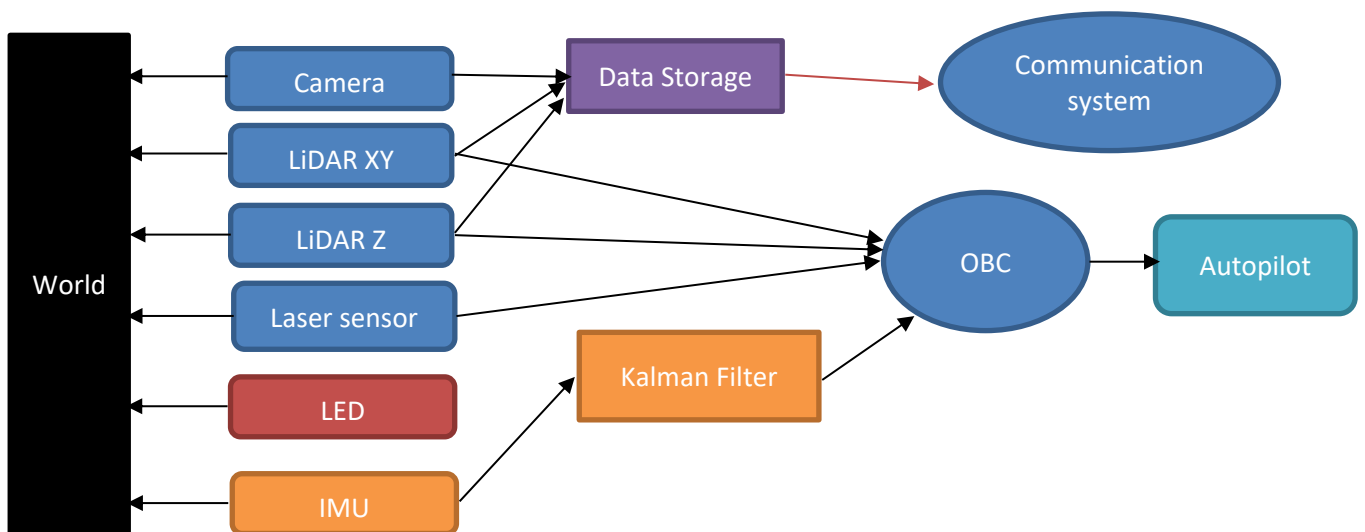
5.3 LiDAR

5.3.1 Configuration

To be able to navigate in an environment without a previous map, the system, in this case, must be able to map the environment through two LiDARs and move by evaluating its position in the newly created map. This procedure must be carried out repeatedly every time the drone arrives in a new area not yet mapped. The need to map involves a time in which the drone must stay in Hovering and therefore an increase in fuel consumption.

Obviously, being the goal of the mission to take photographs, we will need to have a lighting system and a camera able to activate occasionally.

Finally, the estimation of the position using laser detectors is continuously compared with the data provided by the IMU which are then adapted via a Kalman filter.



5.3.2 Figures of Merits

<i>Components</i>	<i>Size [L]</i>	<i>Mass [Kg]</i>	<i>Power [W]</i>
<i>IMU</i>	0,450	0,840	15,000
<i>OBC</i>	0,462	0,500	64,980
<i>LIDAR Z</i>	0,682	0,925	10,000
<i>LiDAR XY</i>	0,682	0,925	10,000
<i>Laser sensor</i>	0,432	0,270	9,000
<i>Camera</i>	0,175	0,379	7,920
<i>LED</i>	0,008	0,060	80,000
<i>Total</i>	2,892	3,899	196,900

Table 27 System features considering the LiDAR configuration with laser distance sensor [annex AD_11]

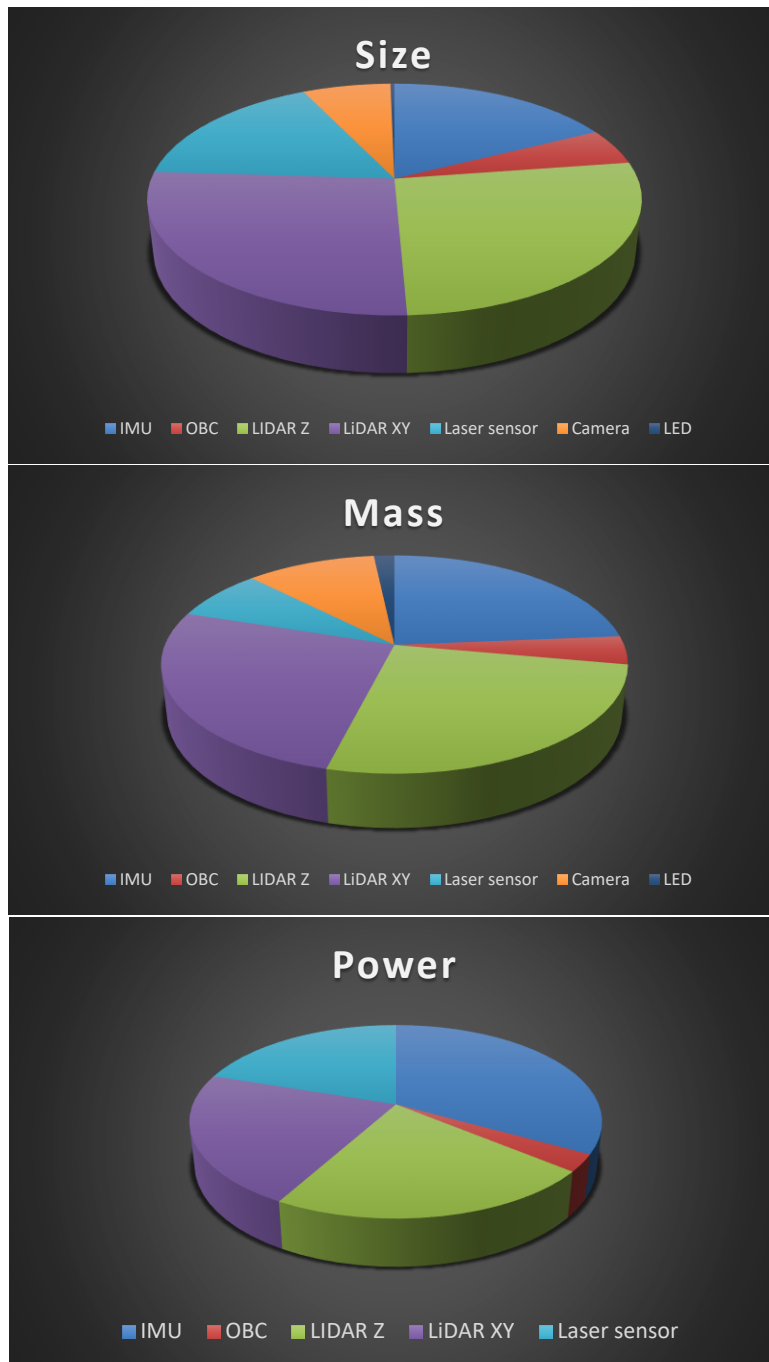


Table 28 Power, Mass, Size comparison considering the LiDAR configuration with laser distance sensor.

5.3.3 Time Mapping

An important aspect to consider is the hovering time required to map the surrounding environment.

The analysis was carried out according to the sampling frequency and the vertical resolution. Obviously, the higher the resolution, the lower the mapping error, since there are more points, and therefore the lower the sampling frequency will also be. At this point a trade off is required [annex AD_11].

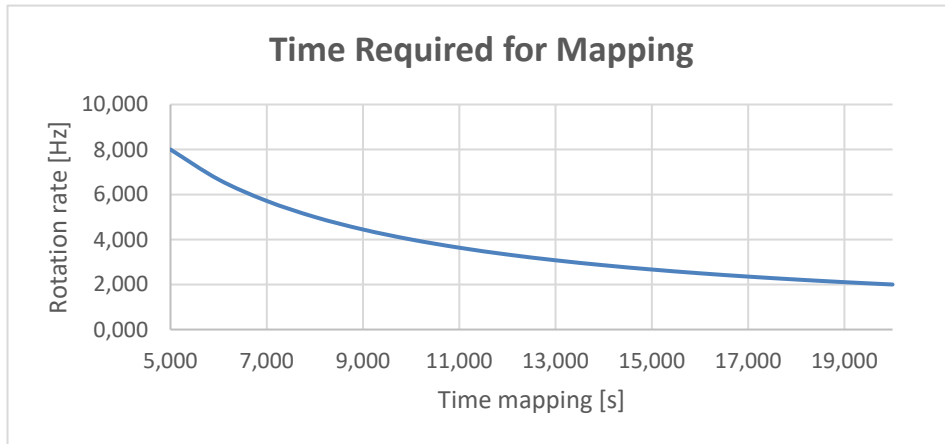


Figure 49 Time required for mapping as a function of the rotation speed of the LiDAR laser sensor. Assuming fixed 1 ° of step as precision in vertical scanning.

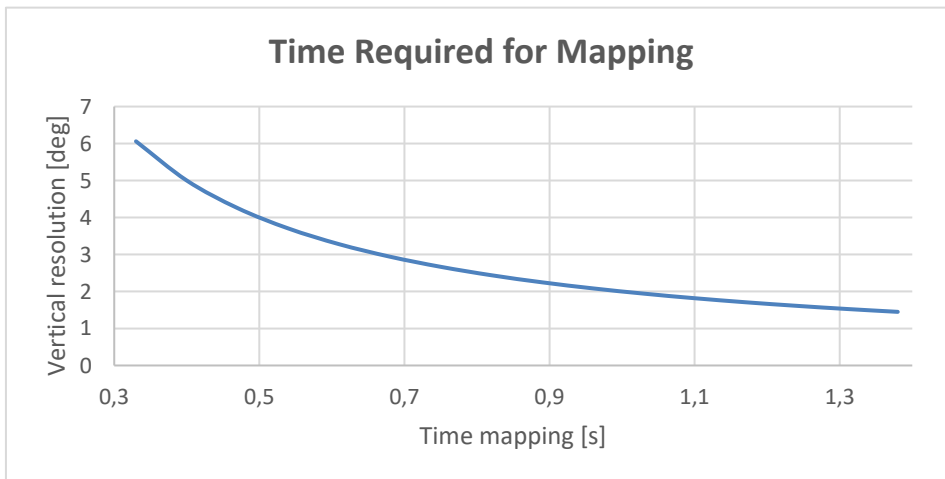


Figure 50 Time required for mapping as a function of accuracy in vertical resolution Assuming a rotation speed of the laser sensor of the LiDAR of 20Hz.

Greater precision also leads to a greater number of data stories and therefore has a greater impact on the OBC and the calculation algorithm.

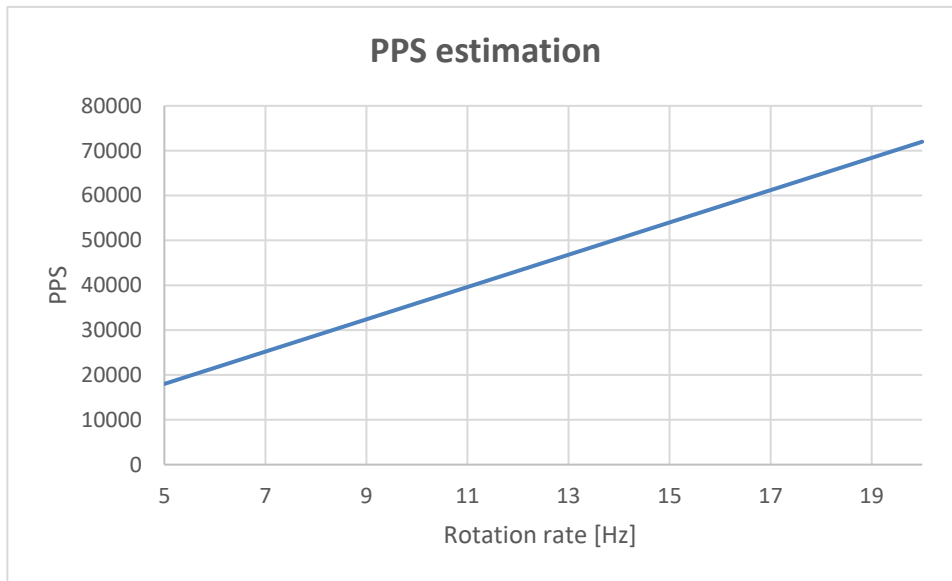


Figure 51 Points per second scanned by LiDAR as a function of rotation speed, assuming a resolution on the horizontal plane of 0.1°.

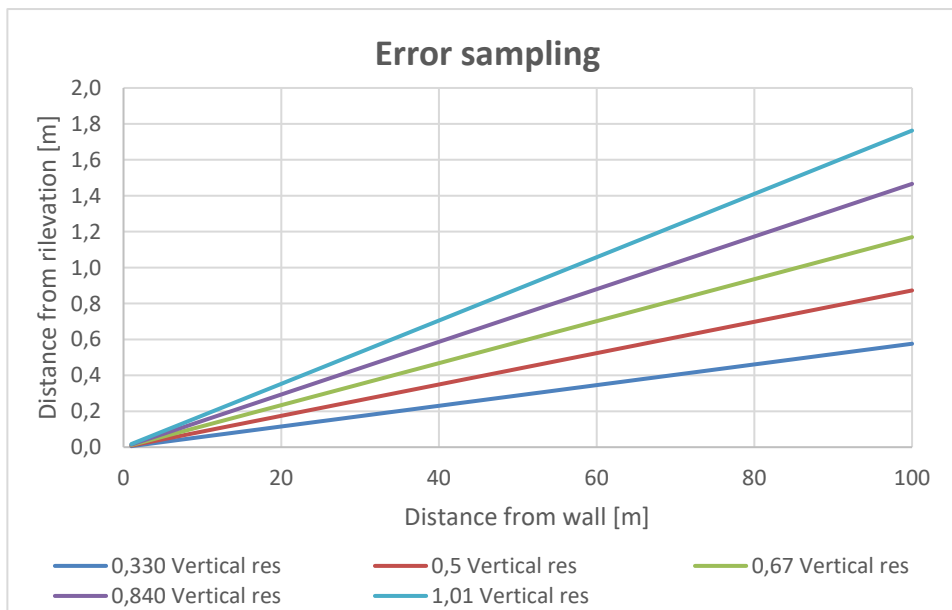


Figure 52 Graph representing the minimum accuracy of object detection as a function of the distance from the walls to be analyzed. The comparison is made considering 5 different levels of vertical resolution.

We need to take into consideration how dense the mapping surveys are, in order to understand if it is acceptable for our mission and how far it is.

5.3.4 Speed consideration

Since we want the control algorithm 10 times slower than the navigation one, the maximum speed that can be reached between the various stops to map will be a function of the distance, taking into account the algorithm delay [annex AD_11].

<i>Speed measurement frequency</i>	20	Hz
<i>Distance measurement frequency</i>	20	Hz
<i>Measuring range</i>	200	m
<i>Measuring accuracy</i>	0,03	m
<i>Delay of the thruster</i>	0,02	s
<i>Delay of the algorithm</i>	0,5	s
<i>Delay</i>	0,52	s
<i>Thrust</i>	50	N
<i>Drone Mass</i>	15	kg

Table 29 Summary table of parameters used to estimate speed limits in the configuration with LiDAR.

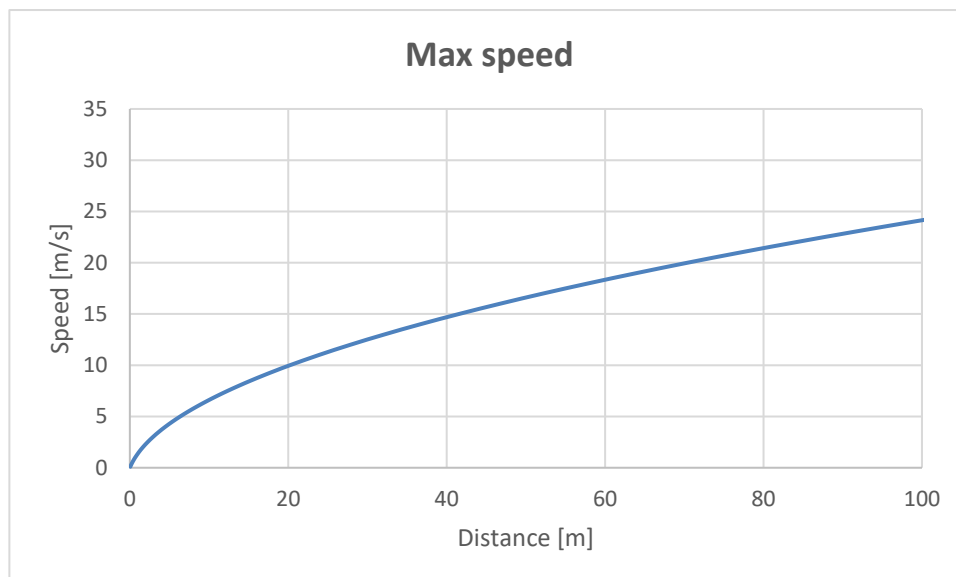


Figure 53 Maximum speed allowed for navigation in caves according to the distance from the walls, with 50N of thrust provided by rotation of the main motor.

Since the drone must be stationary when it maps, it must accelerate and decelerate between one mapping and the other. this leads to lower speeds

5.4 Comparison LiDAR vs Visual Odometry

The first considerations that we are going to do will be taking into account only the architecture and the impact on EPS.

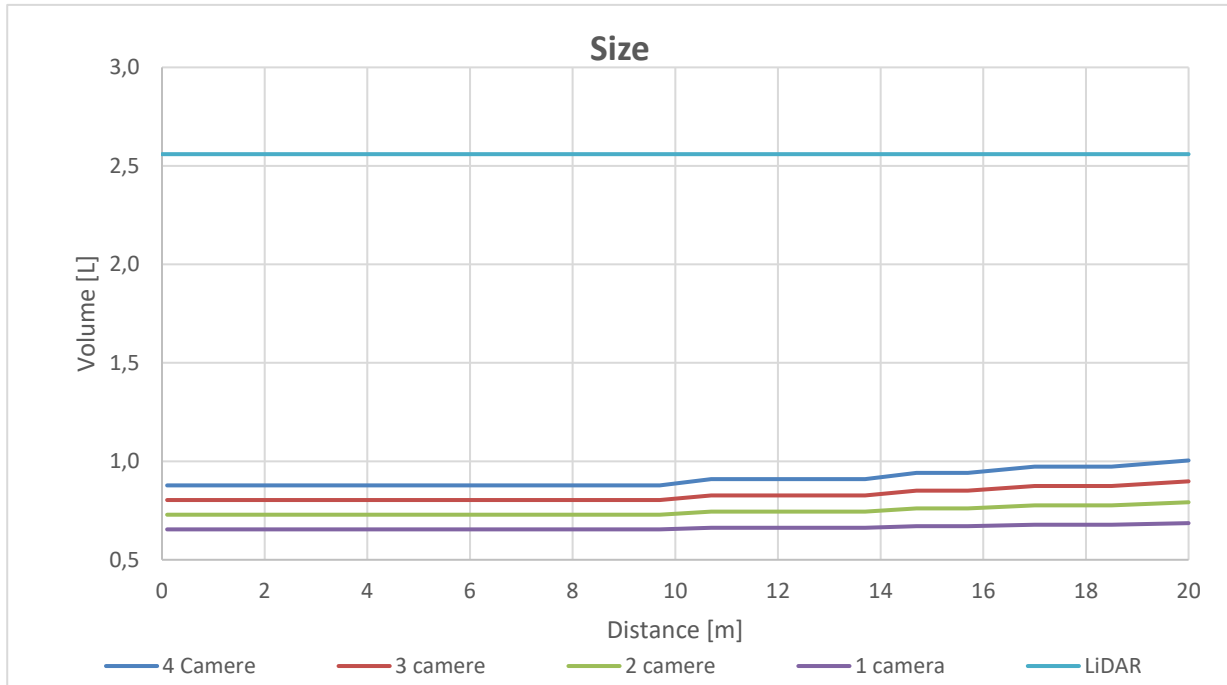


Figure 54 Size comparison between LiDAR configuration and visual navigation configuration with various cameras.

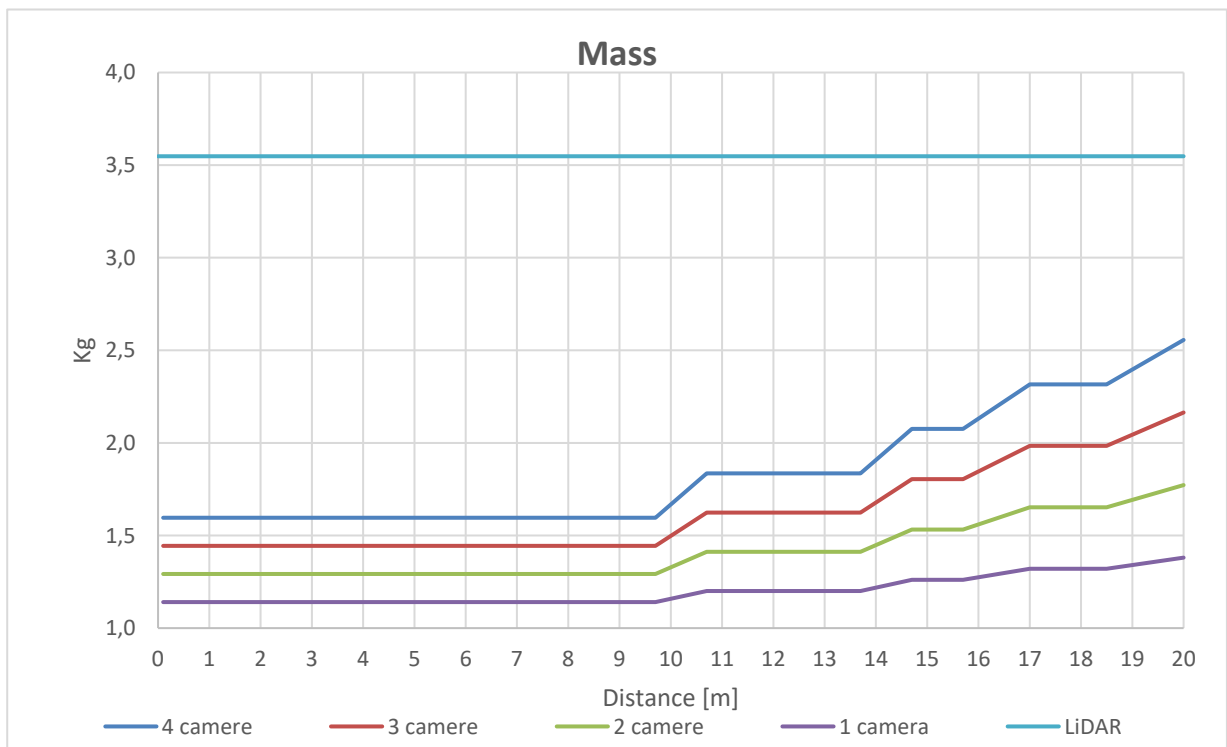


Figure 55 Mass comparison between LiDAR configuration and visual navigation configuration with various cameras.

As far as dimensions and masses are concerned, a clear advantage of visual odometry seems evident, but it must be remembered that for visual odometry a solution to dispose of the heat generated by LEDs was not considered. This discussion will need work in the future.

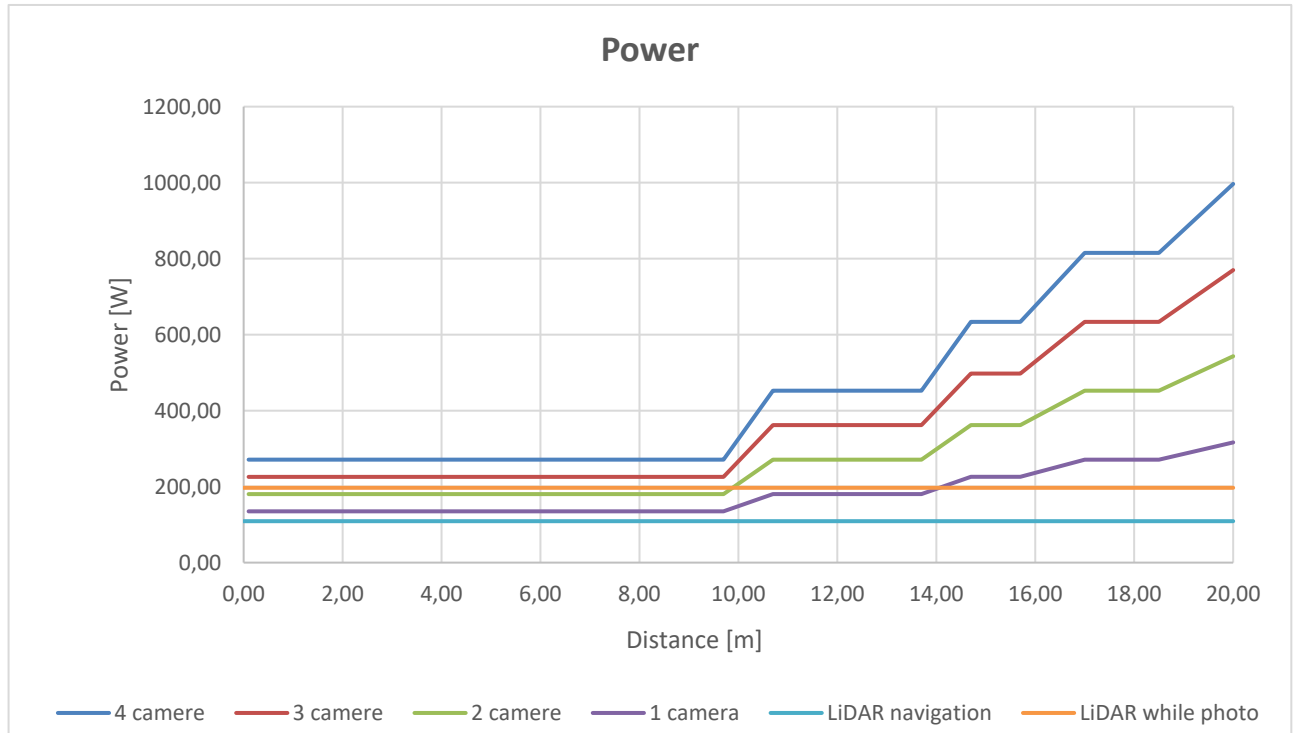


Figure 56 Power consumption comparison between LiDAR configuration and visual navigation configuration with various cameras.

As far as power is concerned, the matter gets more complicated. The power required for navigation alone is much lower than that required for visual navigation, because with LiDAR we do not need to illuminate. Only when we need to take some photos as a mission objective do we consume a little more, but it is still significantly lower, furthermore being a sporadic use we do not need additional solutions to disperse the heat generated by the LEDs.

5.5 Custom Battery consideration

Taking into consideration the calculations carried out by the EPS [13], it is possible to estimate the impact in terms of weight and size of the batteries needed to support the navigation system [annex AD_14].

SIZE [dm ³]	MASS [Kg]	POWER [W]	Wh	Battery size [dm ³]	Battery mass [Kg]
2,56	3,55	133,22	22,20	0,06	0,09

Table 30 Summary table of the parameters obtained considering the batteries to power the navigation system.

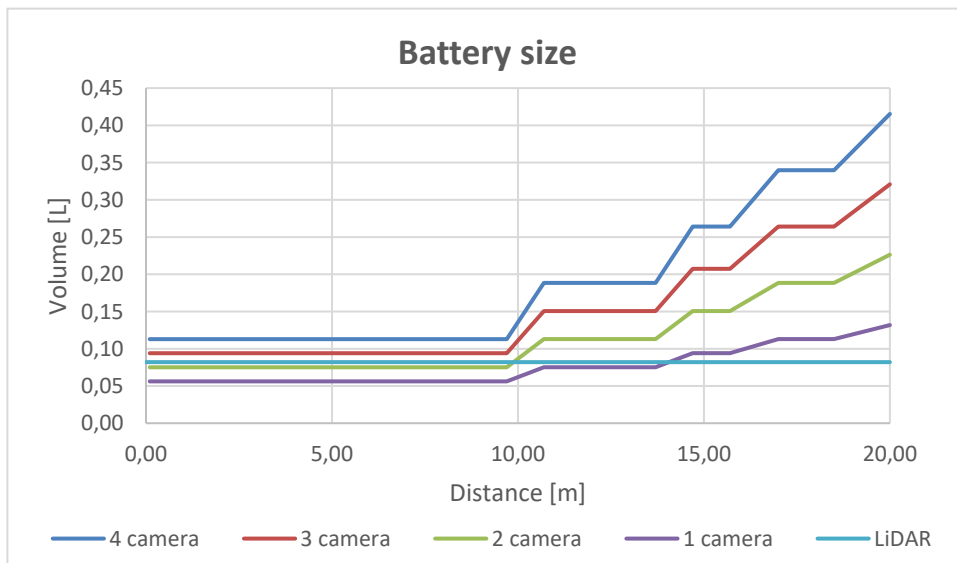


Figure 57 Comparison of the dimensions between LiDAR technology and visual navigation as the number of cameras varies, taking into account the relative sizes of the batteries needed to power it.

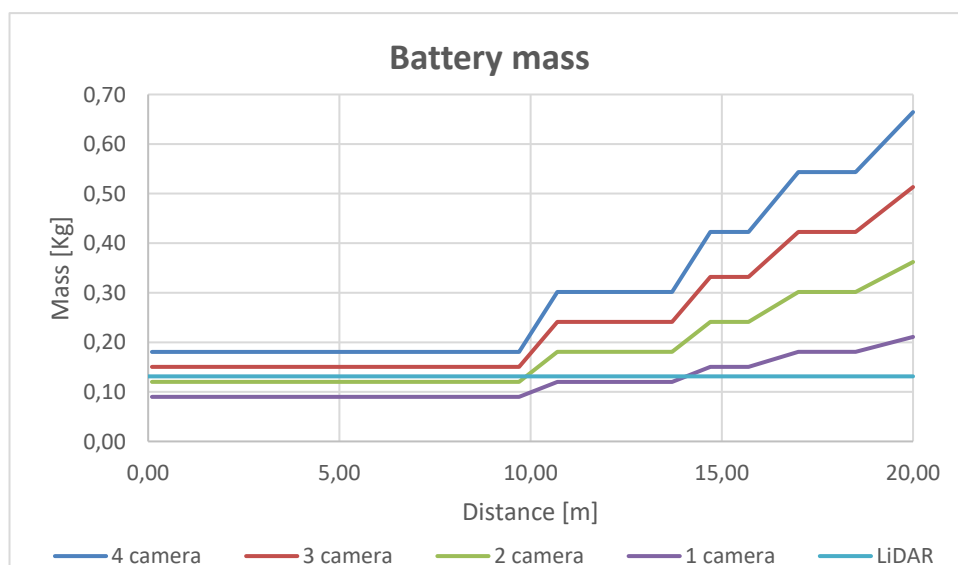


Figure 58 Comparison of masses between LiDAR technology and visual navigation as the number of cameras varies, taking into account the relative masses of the batteries needed to power it.

5.6 Pros and Cons

Visual odometry is easier to implement as the algorithm must be able to process less data, this leads to a smaller processor. Furthermore, the components are much simpler and cheaper than the LiDAR. a further point in favor is that to satisfy the mission objective no additional instruments are needed as we use navigation data as images.

However, at the same time if we use images to navigate we need to have the surrounding environment illuminated, and this requires a lot of power, moreover this power used to illuminate generates heat, which since there is no atmosphere becomes very difficult to disperse and involves the addition of components.

Having to illuminate the environment leads to the possibility that shadows are generated and therefore false detections from the images can occur. This can lead to errors in the navigation system.

A further problem is related to dust, in fact near the ground the jet of the engine raises a large amount of dust that can obscure the field of view of the cameras, completely canceling the effectiveness of the navigation system.

All these limitations lead to the most limiting one which is the maximum range of image acquisition, therefore the maximum distance at which we can stand with respect to the walls. this goes against the problems of dust and also limits the maximum speed allowed in an extremely drastic way. This entails a not negligible increase in fuel consumption which has a very significant impact on all the other sub-systems.

Finally, a configuration with a single main engine and the drone rotating to direct thrust is not possible with visual navigation.

LiDAR on the other hand consumes much less power but needs a hovering time to map the surrounding environment before moving. It also needs a lighting system and a camera to meet the mission requirement of taking pictures

6 CAD

6.1 Introduction

In this section we will discuss the geometry of the individual components. This procedure will be carried out by drawing the individual components on SolidWorks so that you can then see the possible system configurations.

Furthermore, this work, once a configuration is chosen, will be used to 3D print the individual components and the entire drone.

Finally, in the future it will be essential to be able to see the interfaces between the various components, such as wiring and connectors, so as to be able to plan and evaluate the feasibility and effectiveness.

6.2 Navigation System

As far as the navigation system is concerned, the components chosen for the missions are the following, and a faithful copy of the previously chosen COTs components was made on the CAD.

6.2.1 Camera

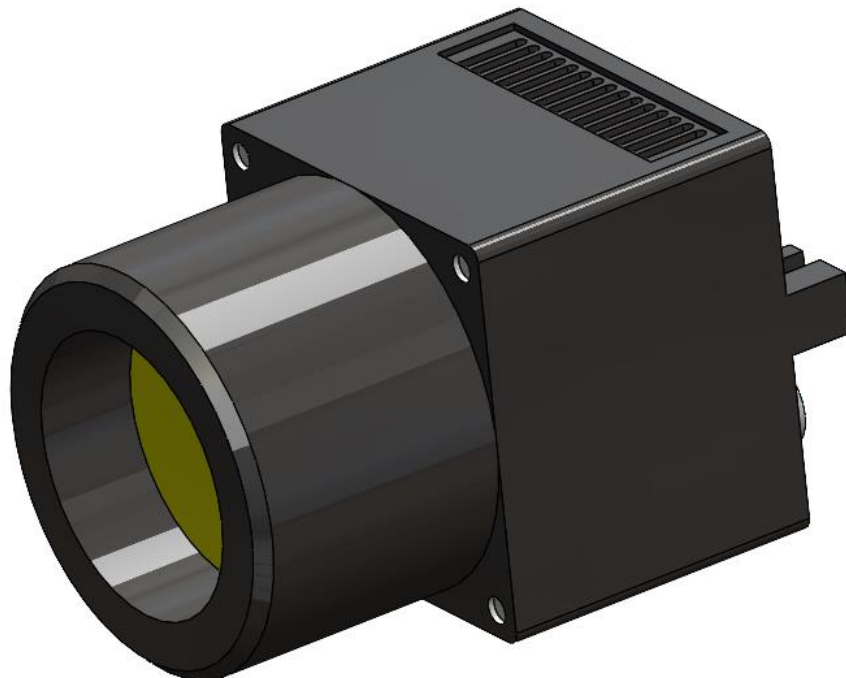


Figure 59 Front view of camera and ImperX lens [annex AD_17].



Figure 60 Rear view of camera and ImperX lens.

6.2.2 IMU

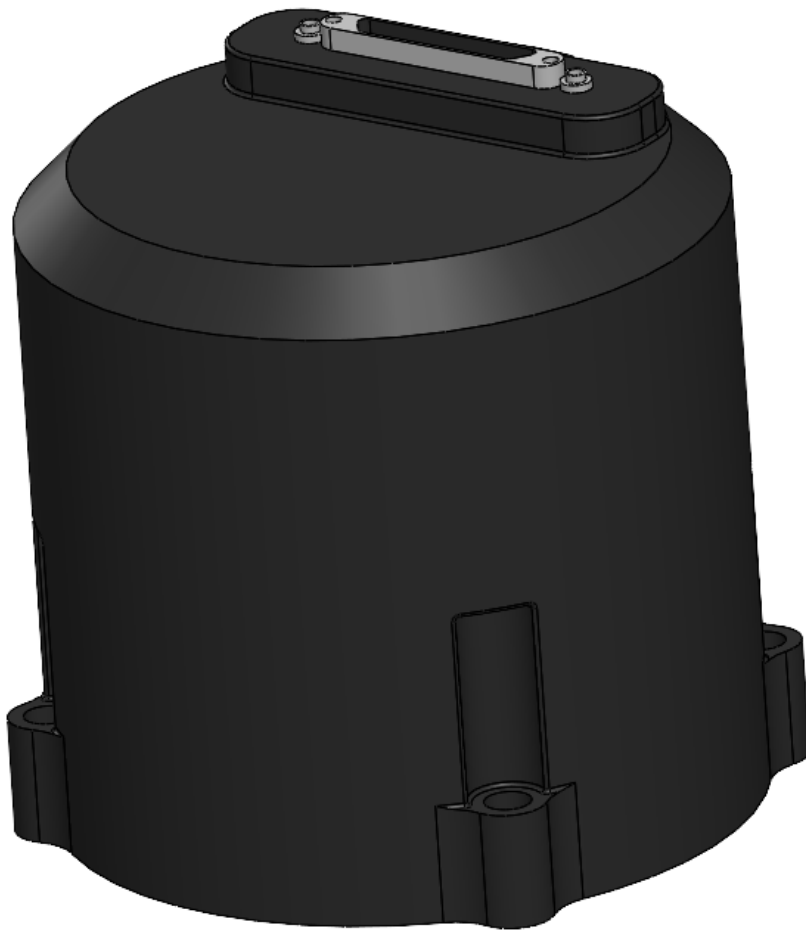


Figure 61 Front view IMU, the rear view is omitted as before of significance [annex AD_18]

6.2.3 LED

This is just the LED, the optic that will be mounted on it is missing.

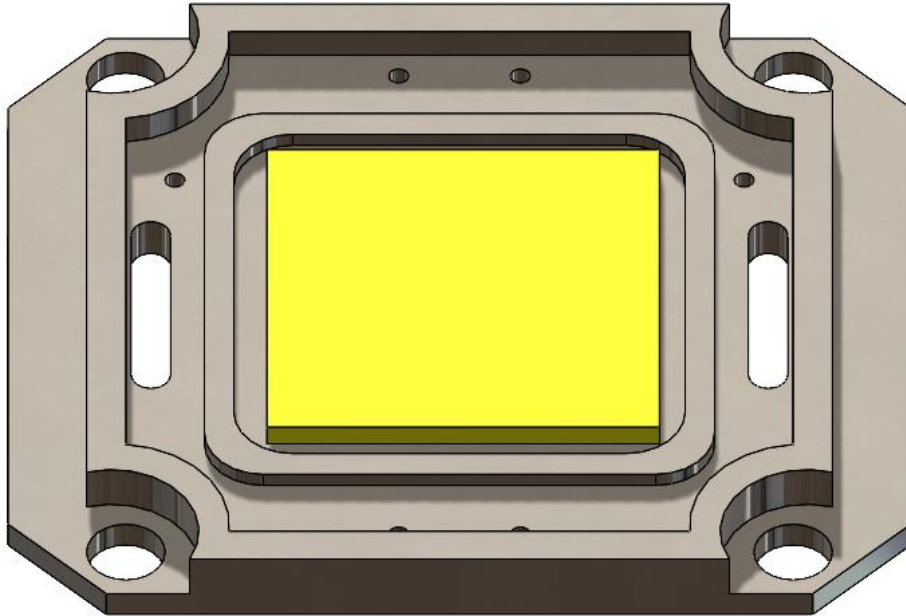


Figure 62 *Front view of the LED [annex AD_19]*

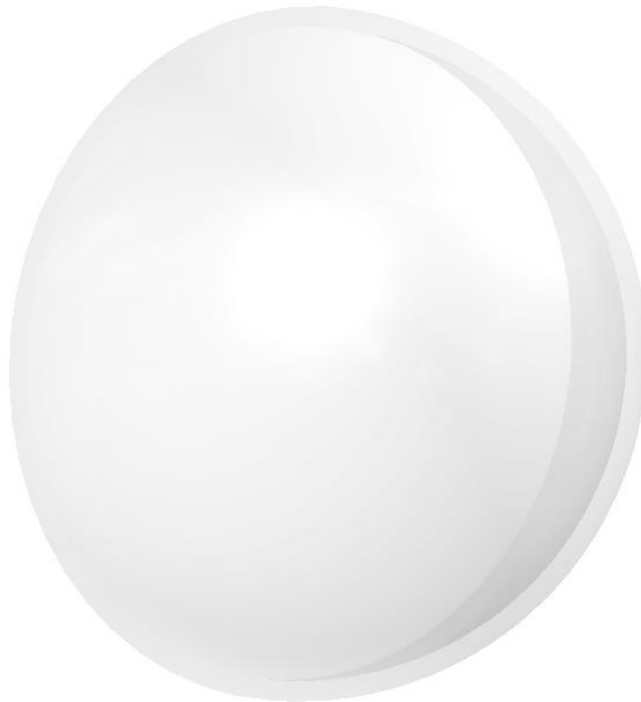


Figure 63 *Front view of LED optics with 60 ° FOV [annex AD_20]*

6.2.4 LiDAR Horizontal plane



Figure 64 *Front view of the LiDAR which deals with mapping at 360 ° on the horizontal plane [annex AD_21]*

6.2.5 LiDAR Vertical Plane

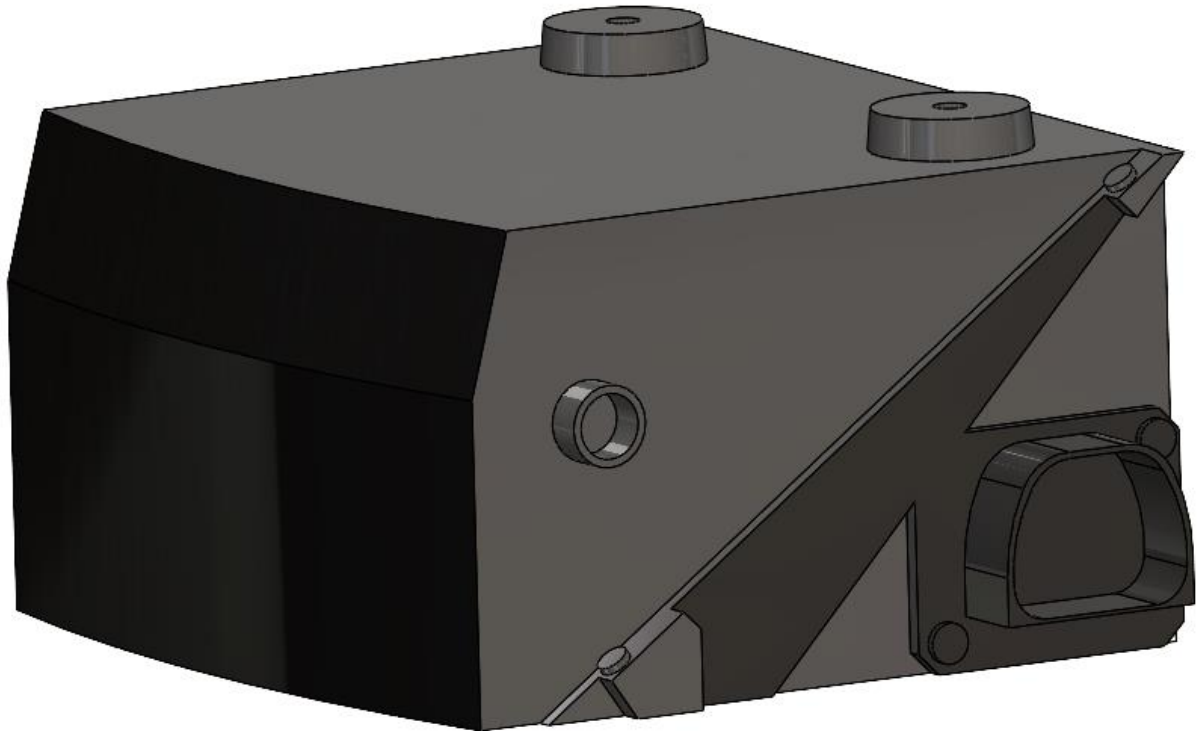


Figure 65 *Front view of the LiDAR which takes care of mapping the ground and estimating the height [annex AD_22]*

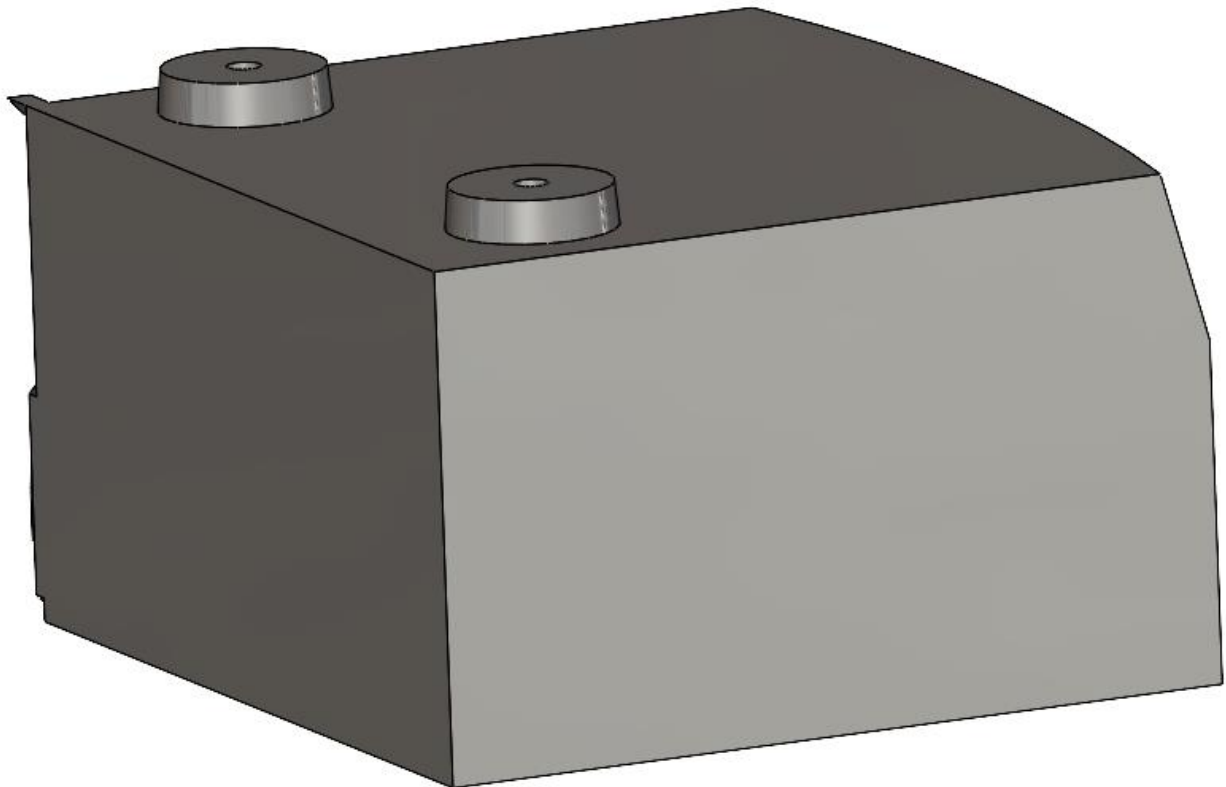


Figure 66 *Rear view of the LiDAR which takes care of mapping the ground and estimating the height*

6.3 OBC

The OBC is a COTs model for spatial use, more thorough calculations could lead to having to change the component or add more than one, for the moment we have chosen to consider this to get an idea of the dimensions and masses required [annex AD_23].

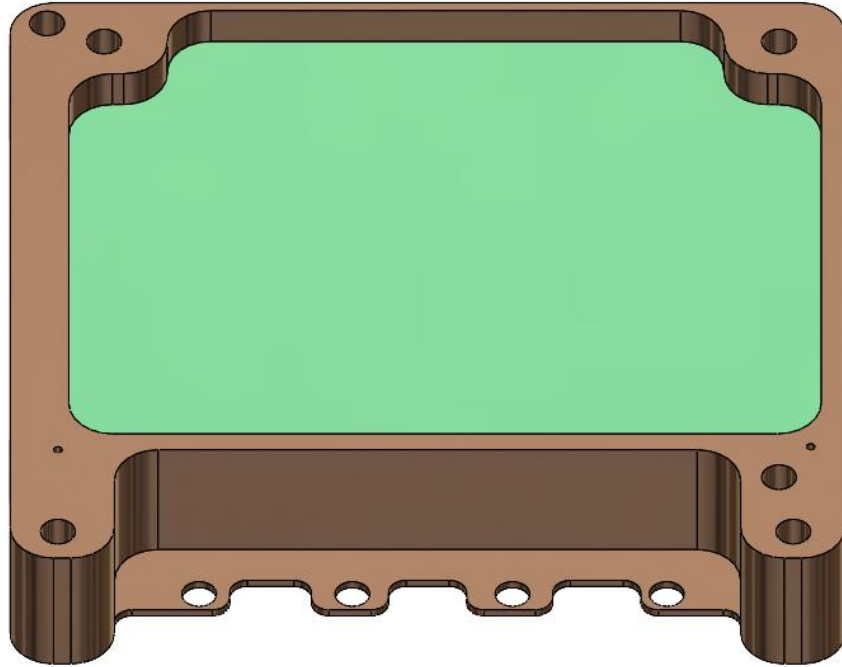


Figure 67 OBC front view

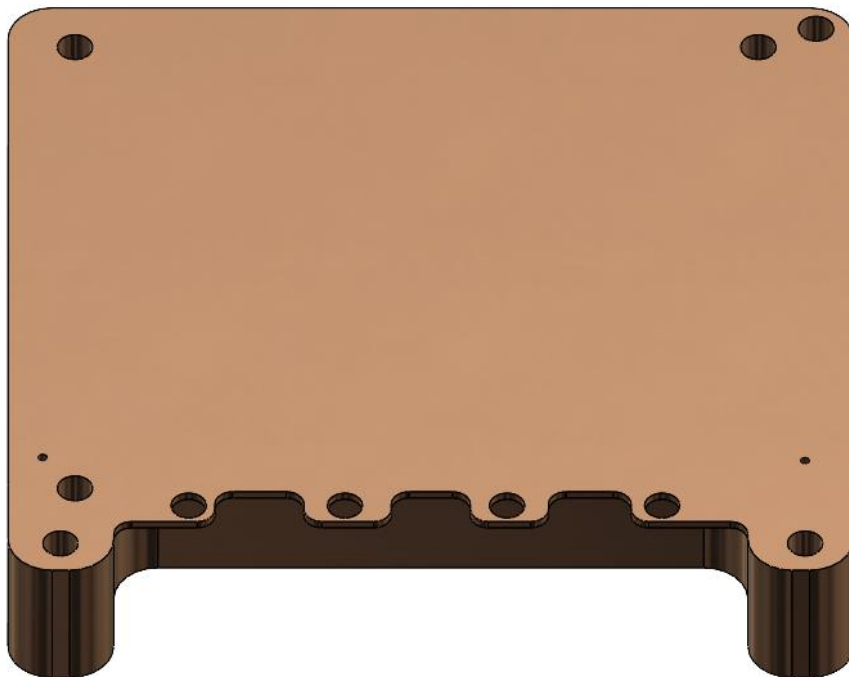


Figure 68 OBC rear view

6.4 EPS

From the data provided by the EPS two possible configurations of commercial batteries were considered, the wiring and connectors have not yet been considered.

6.4.1 Battery

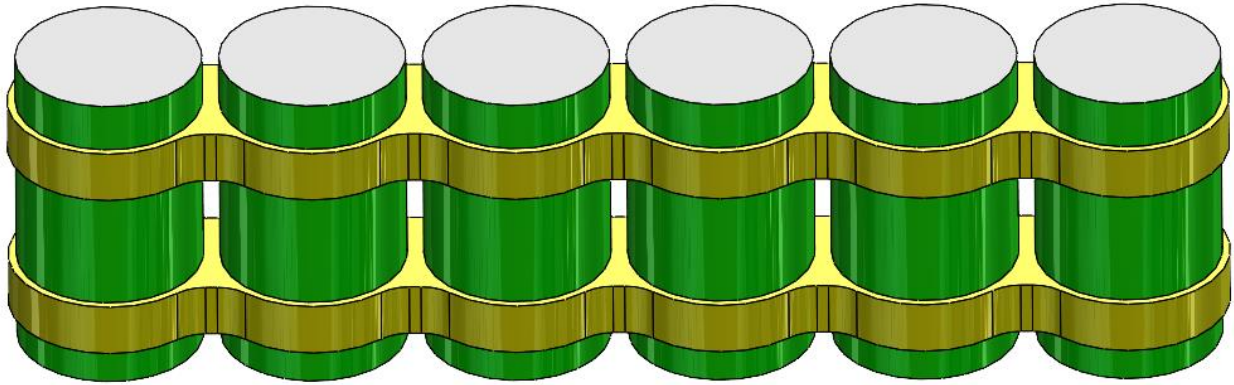


Figure 69 Battery pack with connectors in the 6x1 configuration [annex AD_15]

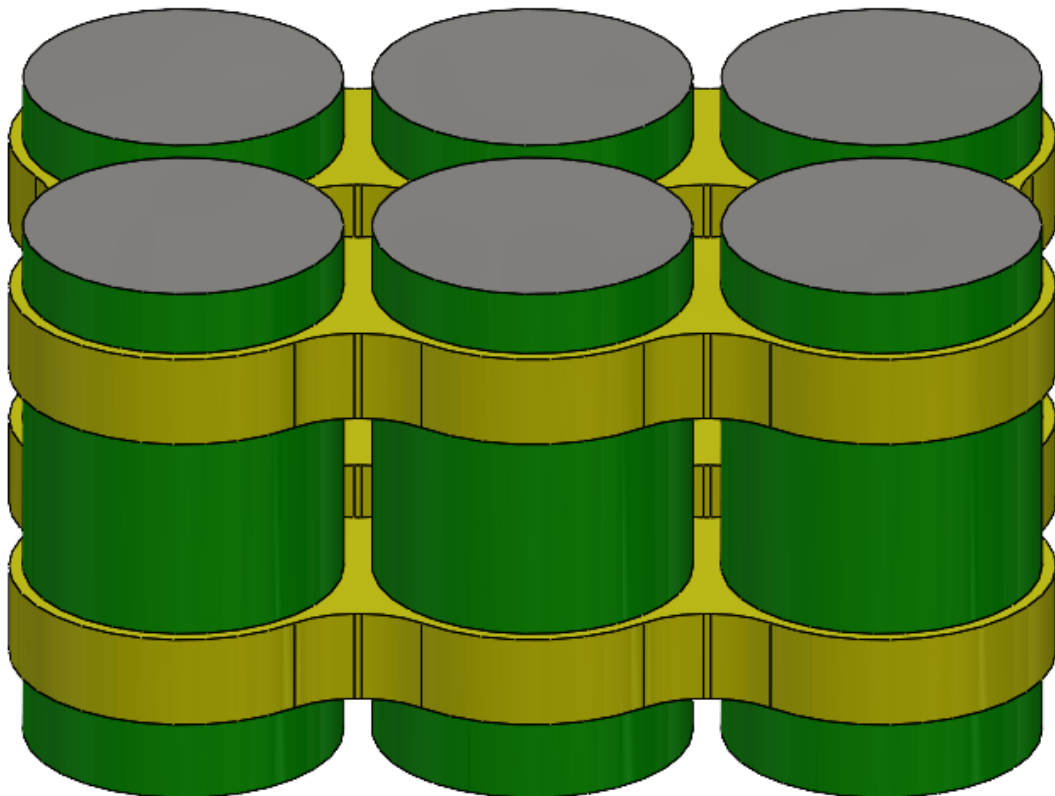


Figure 70 Battery pack with connectors in 3x2 configuration [annex AD_16]

Due to the need for space, the second configuration, the 3x2 one, is the most suitable for our drone.

6.5 Propulsion

The geometric data relating to the thrusters comes from the propulsion system [14] and has been designed specifically for our drone, all followed by the T4i company.

6.5.1 Main Thruster

Three different motors have been designed: 50N, 75N and 100N. All with $ISP = 155$ and $\varepsilon = 70$. The necessary data were provided by the study of the propulsion system.

From system analysis, comparing consumption, dimensions and weights the 75N configuration was chosen.

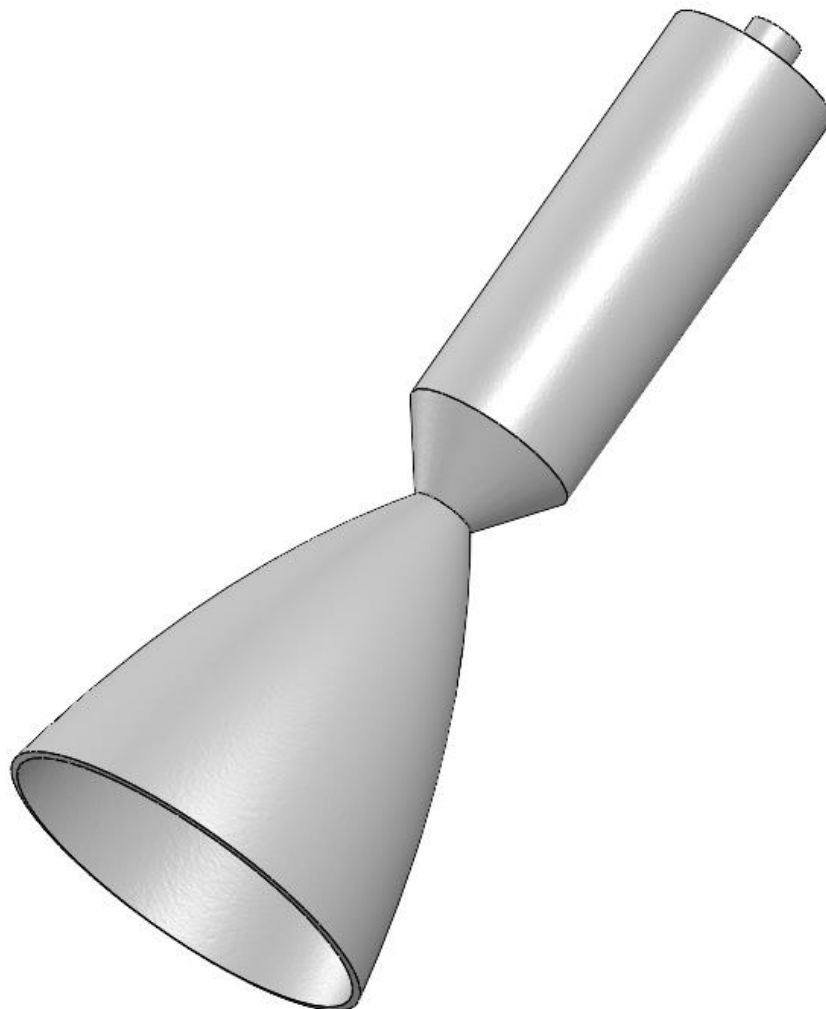


Figure 71 50 N thruster front view [annex AD_26]

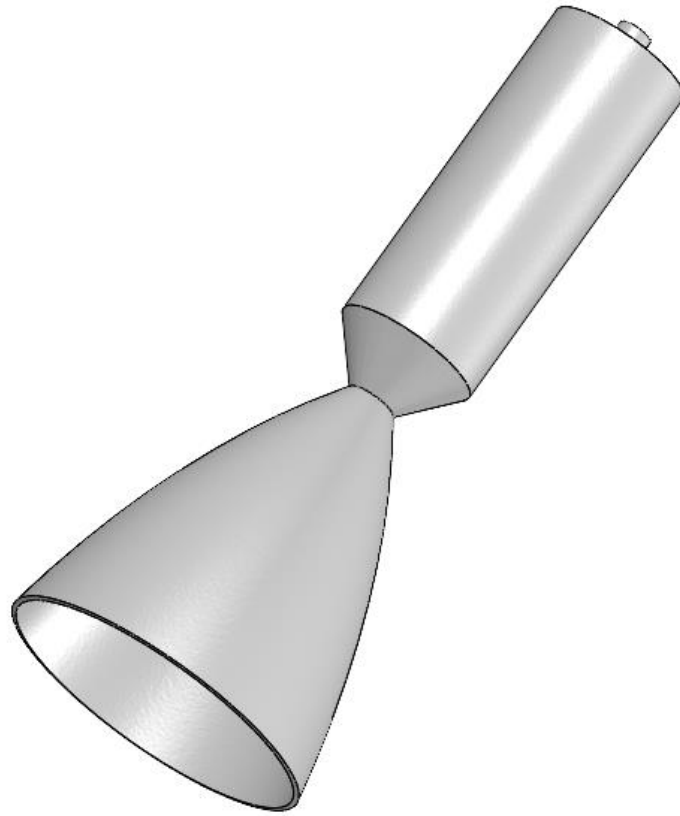


Figure 73 75 N thruster front view [annex AD_27]

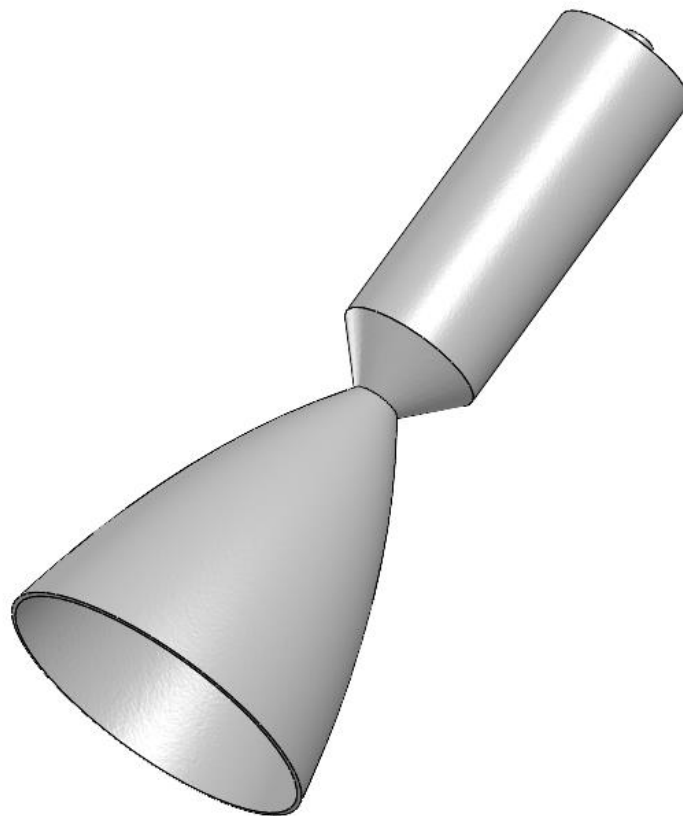


Figure 72 100 N thruster front view [annex AD_28]

6.5.2 Reaction control system

Two models were chosen for the attitude control engine. 5N and 1N of thrust. The data has always been provided by the study of the propulsion system [14].

The configuration with 1N of thrust appears to be the most promising for the overall dimensions and pressure drops of the valves necessary to manage the thrust.

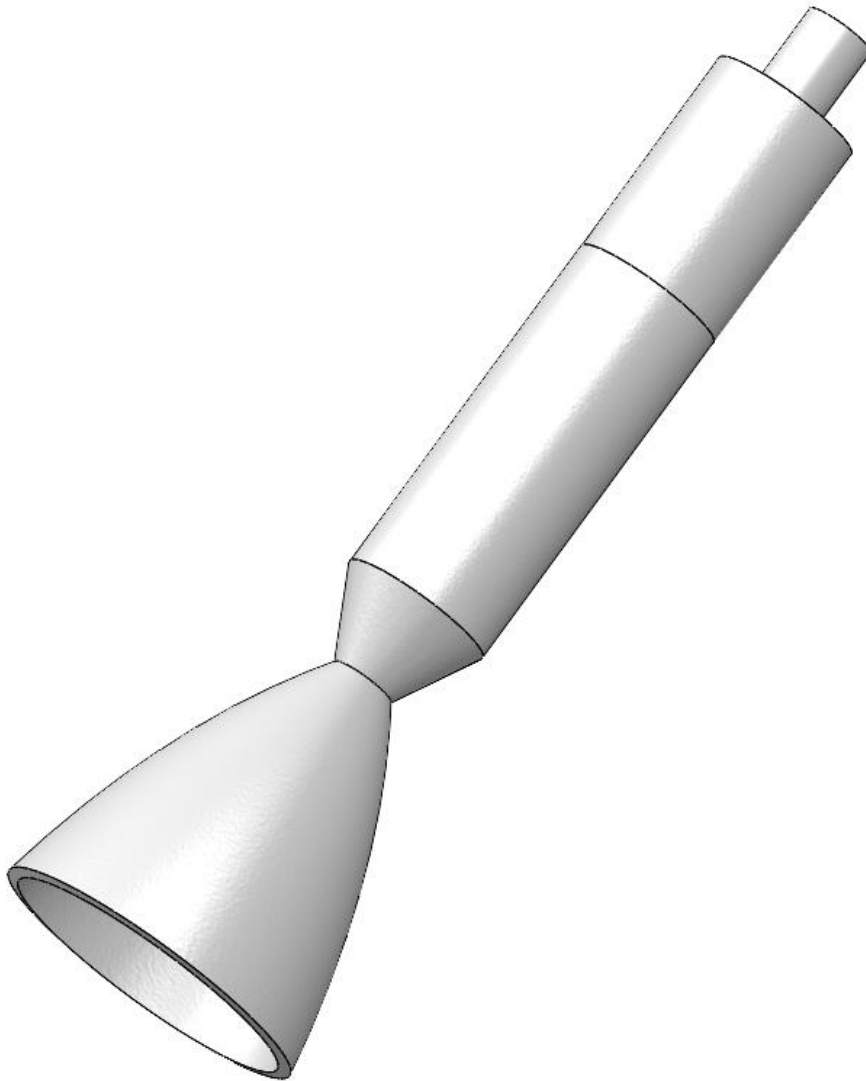


Figure 74 Front view of the 1N thruster necessary for the attitude control of the drone [annex AD_24]

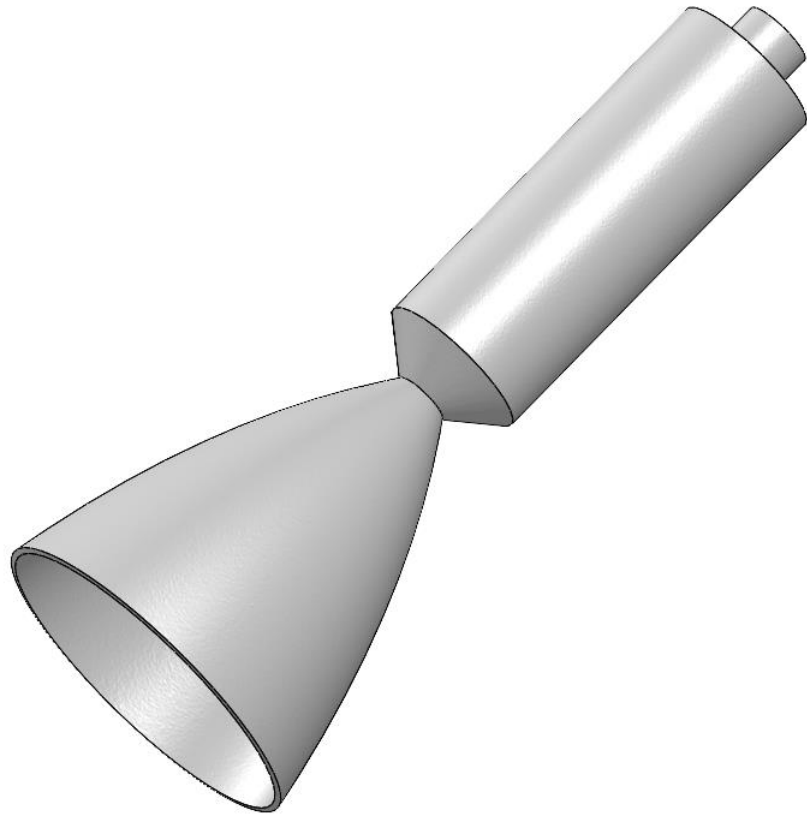


Figure 75 Front view of the 5N thruster necessary for the attitude control of the drone [annex AD_25]

6.5.3 Valves

The valves necessary for the propulsion system are many and of many types depending on the application they must perform. Data are provided by the study of the propulsion system [14].



Figure 76 Front view of a LEE IEP solenoid valve used for trim control thrusters [annex AD_33]

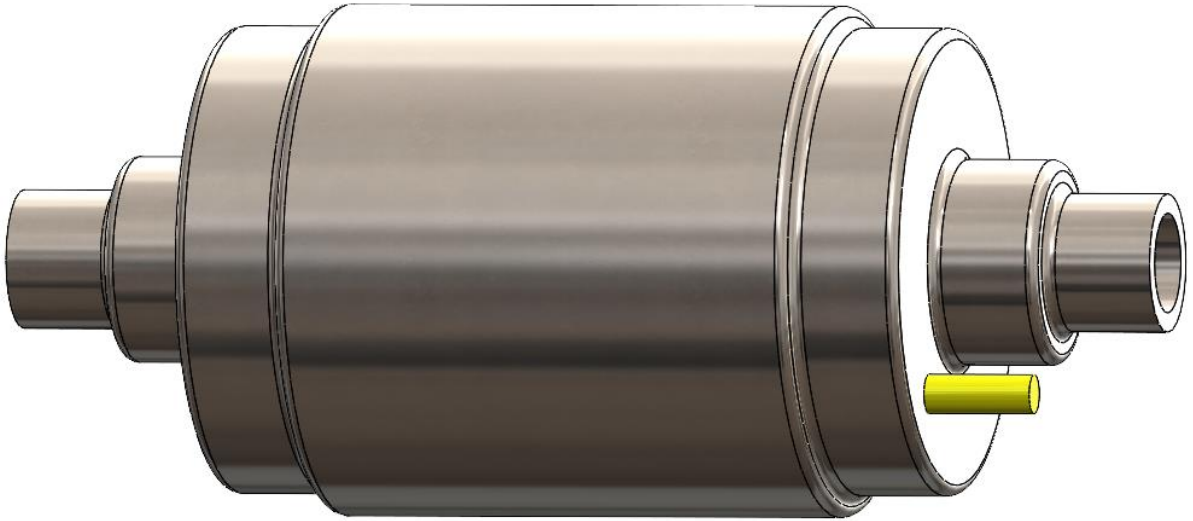


Figure 78 Front view of a Latch valve [annex AD_34]



Figure 77 Front view of a pintle [annex AD_35]

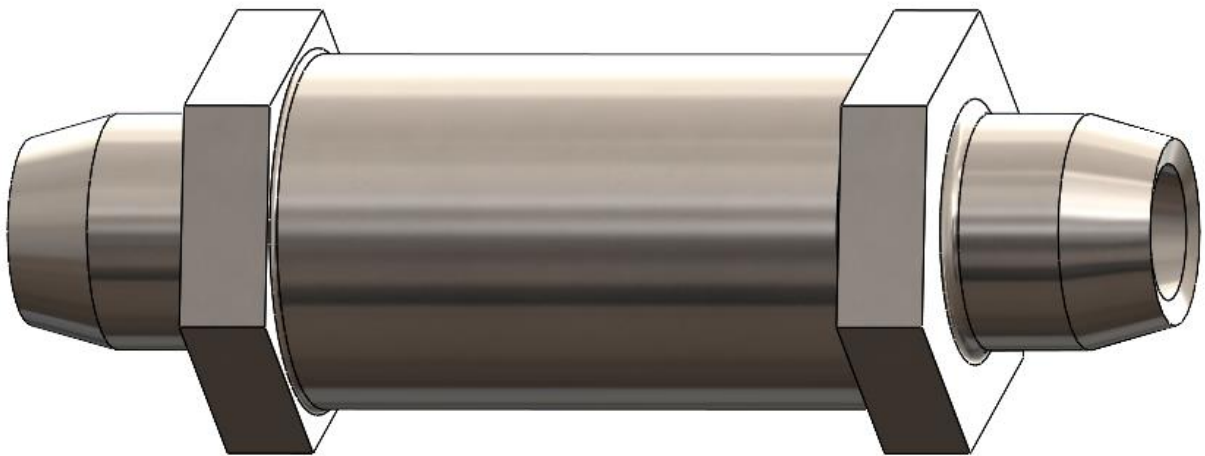


Figure 79 Front view of a check valve [annex AD_36]

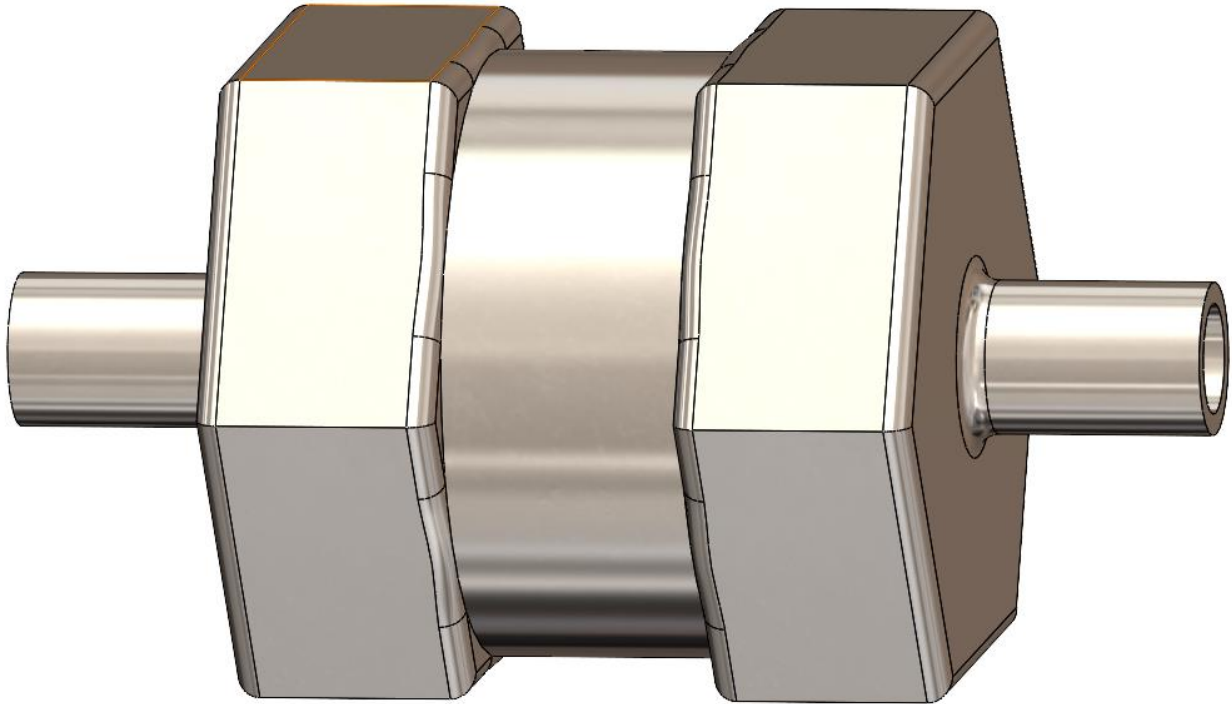


Figure 80 *Front view of a Filter [annex AD_37]*

6.5.4 Propellant Tank

For the realization of the propellant tank it is possible to make it with various shapes. The only real limitation that has been found are the very small spaces that remain available in the drone. Thanks to the data provided by the study on the propulsion system [14], it was possible to create an optimal tank for our configuration [annex AD_29].



Figure 81 *Front view of the propellant tank*

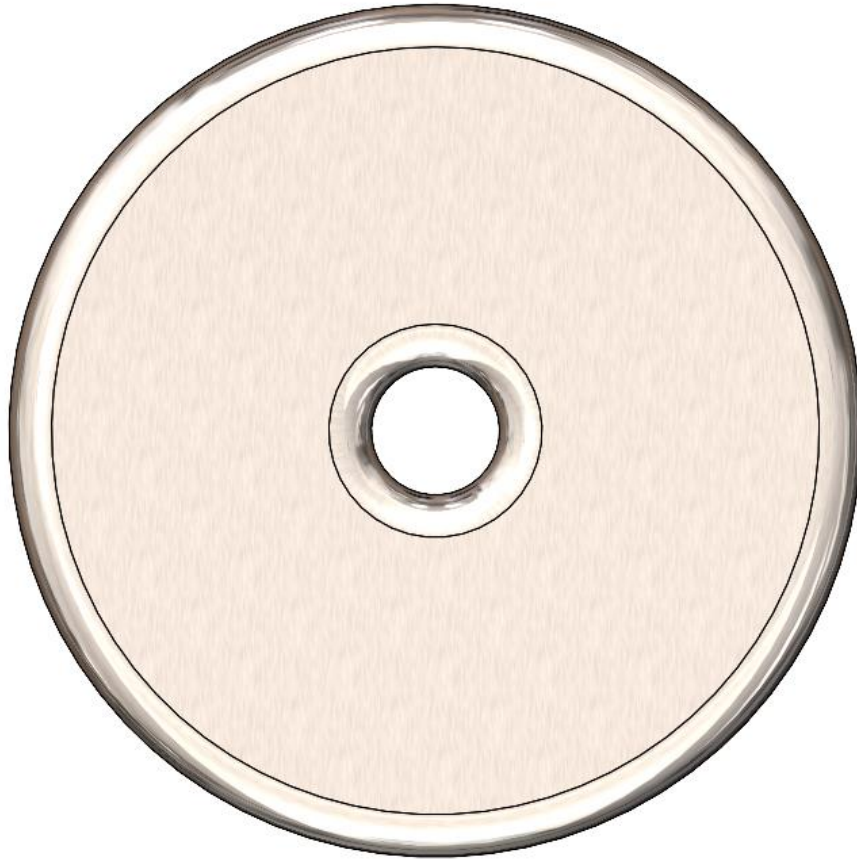


Figure 82 *Upper view of the propellant tank*

6.5.5 Pressurant Tank

In the same way as the propellant tank, in this situation the greatest limitation is the space, however for the pressurizing tank there is also the limitation on the shape. As having extremely high pressures, hundreds of BAR the only possible configuration is the sphere [annex AD_30] [14].



Figure 83 *Front view of the pressurizing tank*

6.6 Structure

The external structure has not yet been analyzed, and a structural analysis to ensure survival at the launch is certainly necessary. The enclosures that will be seen later have the sole purpose of showing the placement of the components in the required 12Us and also to understand which configurations are feasible and which are the best.

6.6.1 Configuration 10x20x60

This configuration is very unstable, as the length on one side, much greater than the others, leads to unsatability. Furthermore, the need to have the lidar on the vertical plane looking into the same face of the engine leads to a non-symmetrical system and therefore complications at the level of attitude control. Furthermore, the trim control system trusters are not small enough to put 8 paired, as the smaller side is only 10 cm [annex AD_31].

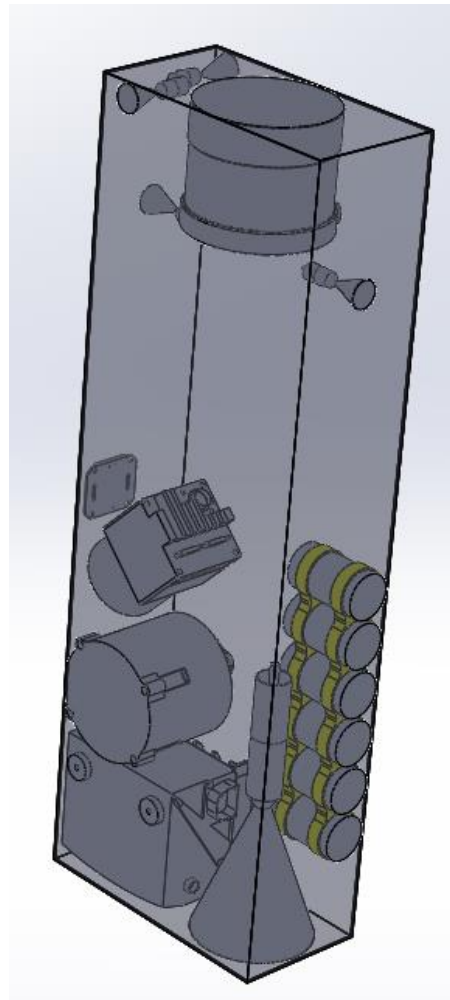


Figure 84 Front view of the assembly in the 10x20x60 configuration

This configuration was immediately abandoned in the design phase due to both dimensions and instability problems.

6.6.2 Configuration 20x20x30

This is the configuration we have chosen to adopt. After other iterations, the arrangement could certainly change. This is a much more stable and compact setup.

It is important to remember that the structure has not been studied but a hypothetical one has been designed to show how some components interface with the structure and how a final result can come. [annex AD_32].

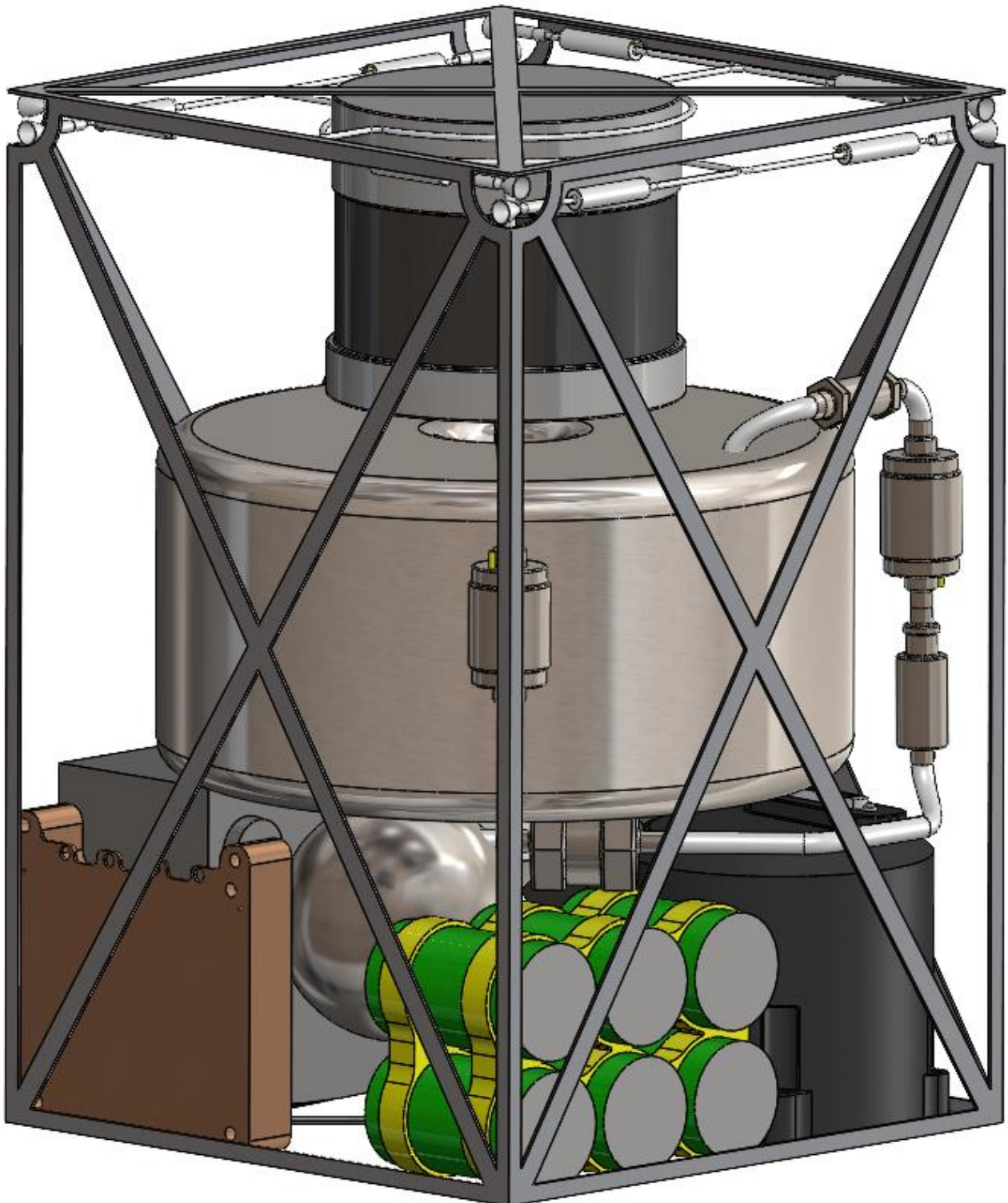


Figure 85 Side view of the drone assembly with structure and components.

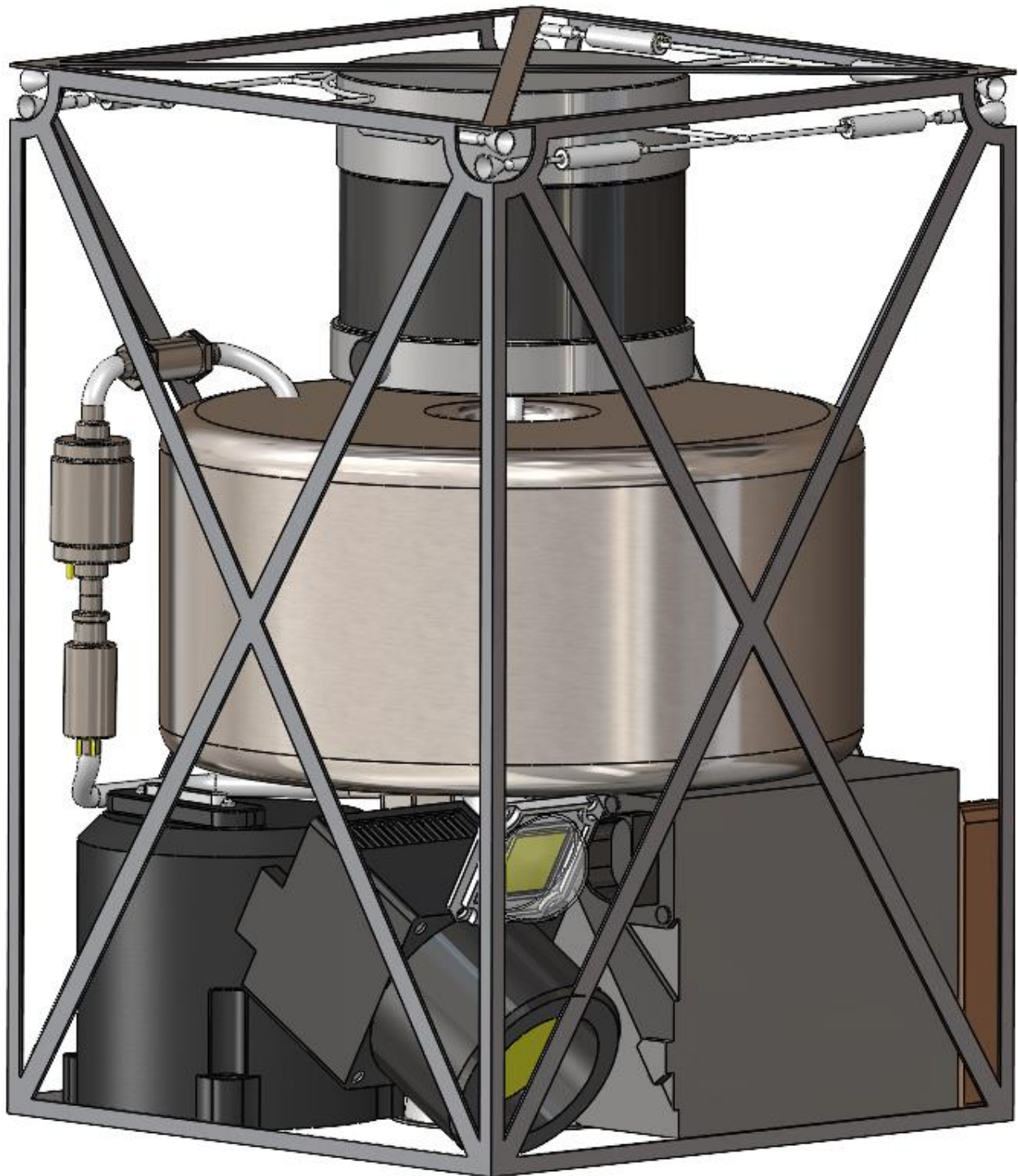


Figure 86 Side view of the drone assembly with structure and components.

Surely a structural calculation and more considerations will lead to modify and implement this first iteration.

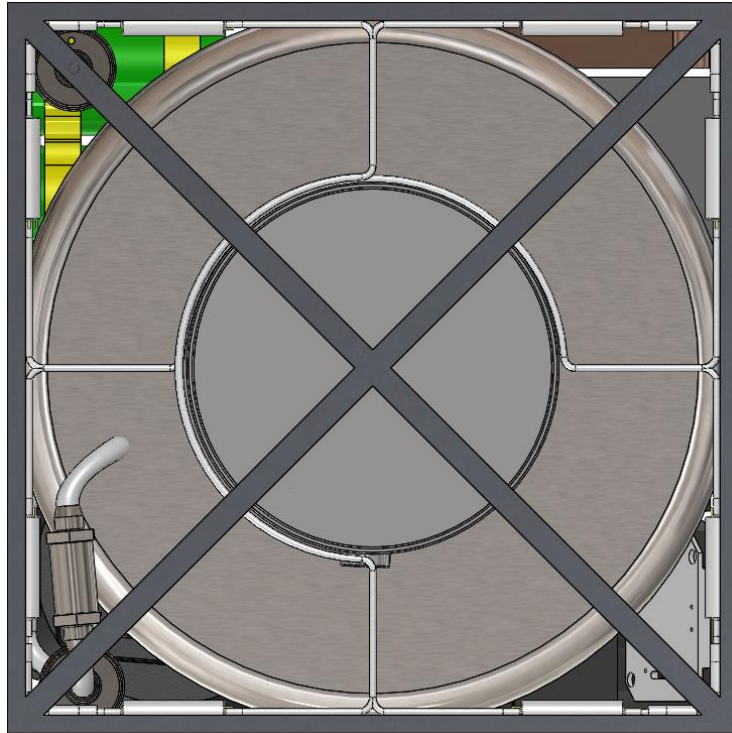


Figure 87 *Top view of drone with structure*

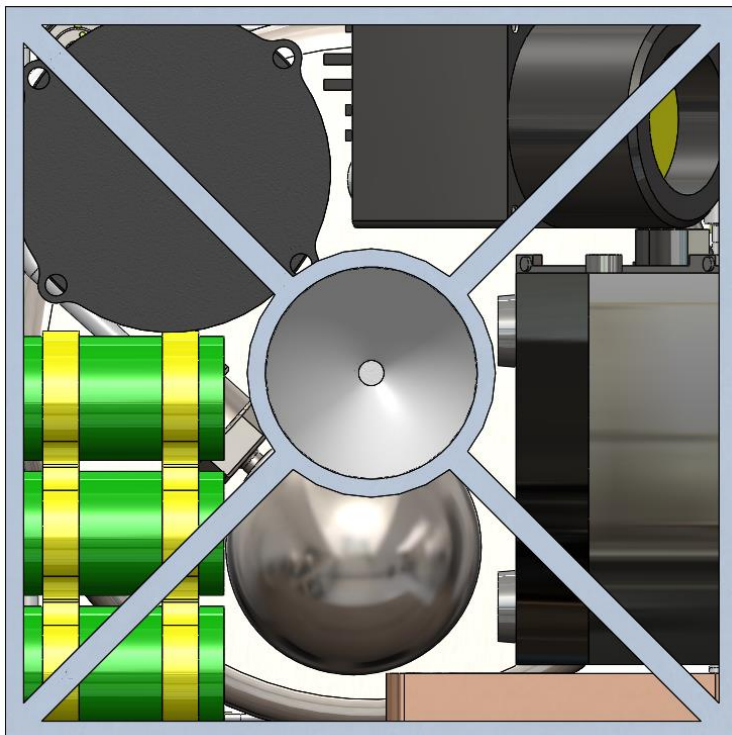


Figure 88 *Bottom view of drone with structure*

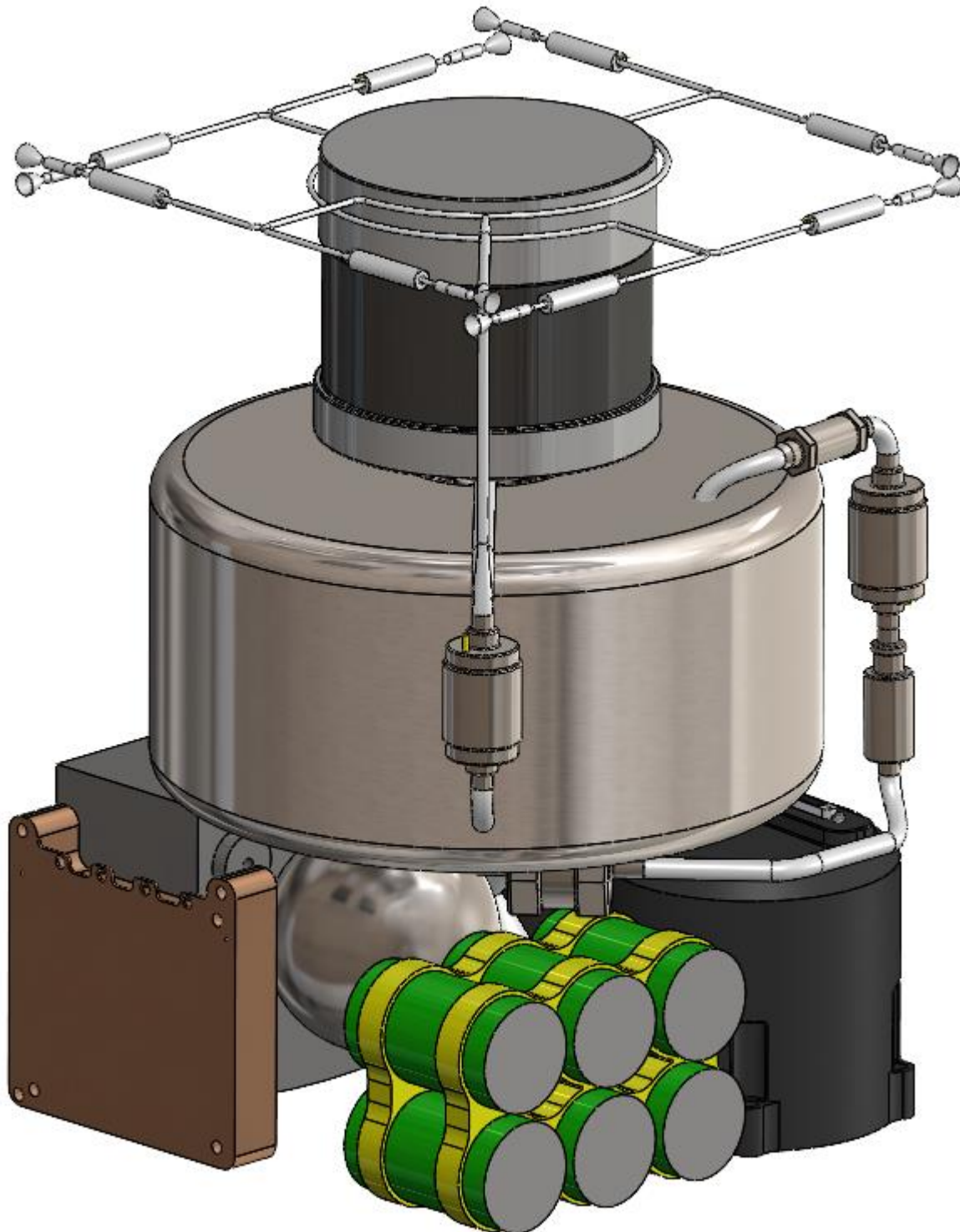


Figure 89 Side view of the drone assembly considering only the components, without structure.

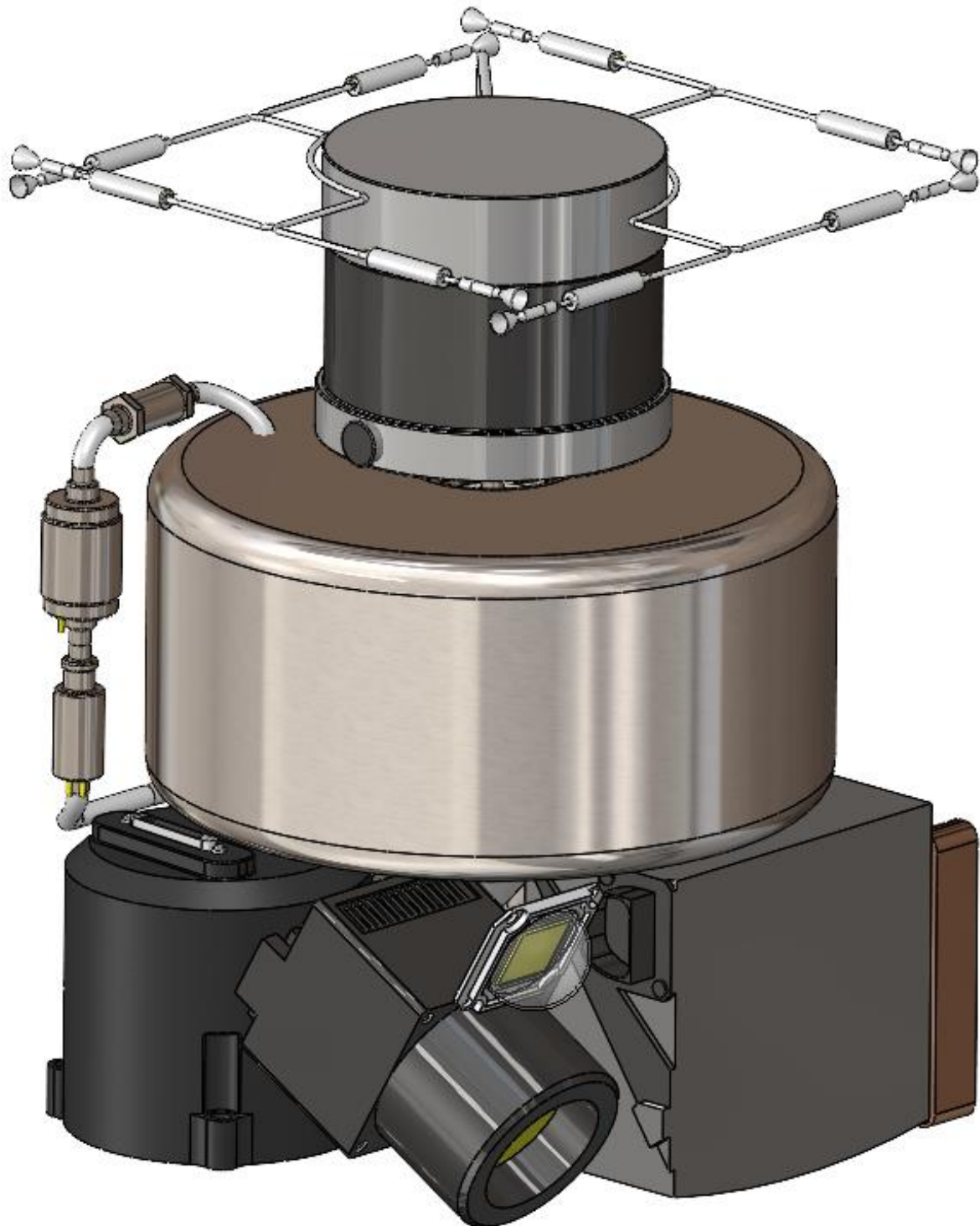


Figure 90 Side view of the drone assembly considering only the components, without structure.

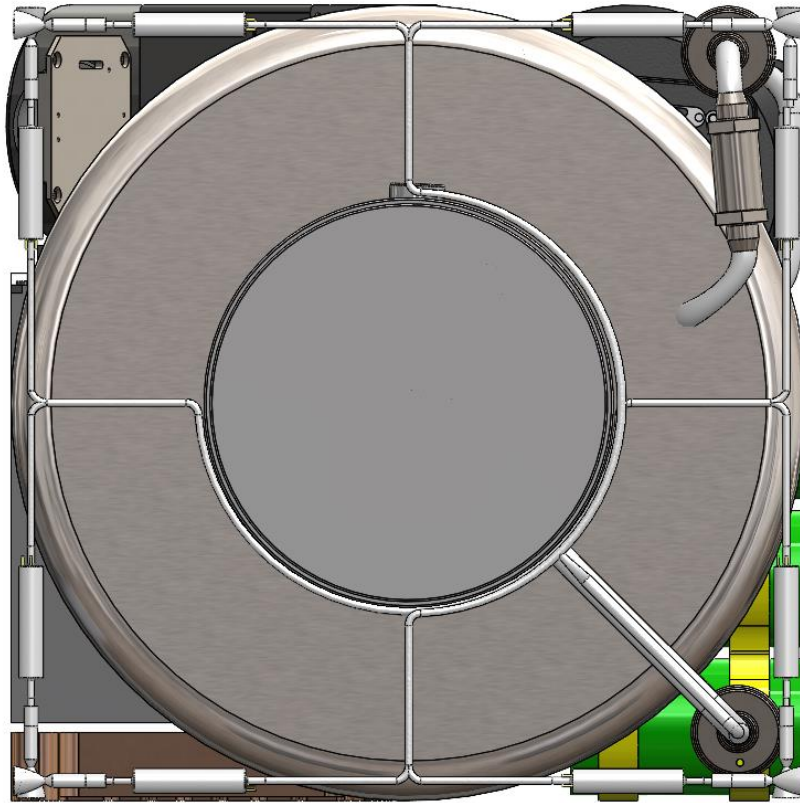


Figure 91 *Top view of the drone without structure*

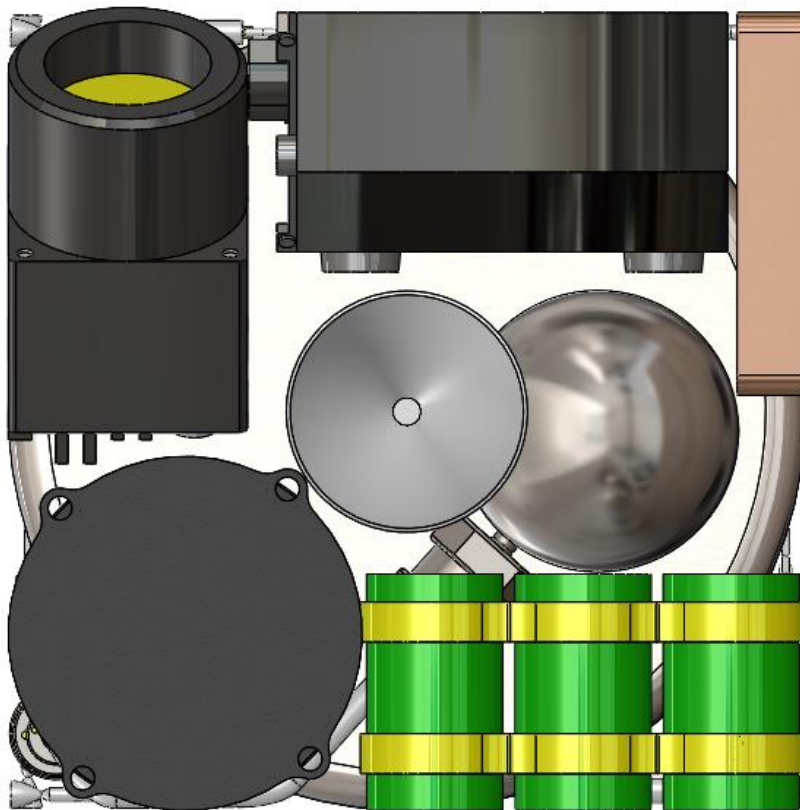


Figure 92 *Bottom view of the drone without structure*

7 Conclusions and recommendations

The analysis carried out shows the most suitable configuration for the mission is the second (LiDAR + Visual navigation). During vertical take-off the LiDAR is used as an altimeter in conjunction with the IMU and camera to locate the crater and therefore the direction, a hovering time was assumed in which the rotation of 5 s takes place. The height after the vertical climb that has been chosen to adopt is 30m and is in accordance with the minimum requirements necessary for the navigation system and the minimum consumption of the propulsion system

During the approach phase to the crater the same components are used and also from the study carried out it is clear that the optimal inclination angle of the drone is 37° taking as parameters 120° FOV of the camera and 120° of inclination from the vertical axis.

During the hovering phase above the crater, the time necessary for the mapping was estimated to be 0.160 ms, but it was decided to keep 0.5s as the time required as a conservative hypothesis.

During the descent into the crater, the second LiDAR is also used to map the surrounding walls and correct the error generated by the integrations of the IMU on the position and therefore improve the accuracy of the navigation system.

At the bottom of the crater there is the most important phase which consists in hovering at a constant height by rotating on itself and photographing the surrounding environment, in this phase the LEDs are also used to allow the camera to better capture the images, a duration of 10 seconds was assumed, even in this case there were conservatives.

During the ascent phase, the crater is remapped with LiDAR and provides indications and corrections on the position until reaching the outside where the drone must be able to relocate the rover thanks to the visual navigation and start sending the previously taken and stored images to the rover. At the peak of the ascent, another 5 seconds of hovering were assumed in which there is the location of the rover and therefore the estimate of the direction to take.

Finally, the drone must approach the rover and start the landing maneuver, in this step the LiDAR that allows to map the ground is essential in conjunction with the attitude control system, the time estimated necessary to carry out the mapping is 0.5 seconds.

This project led to an initial analysis of the navigation system. What has been done so far is only a first iteration, in the future many more iterations with other systems and an optimization work will be needed in order to reach convergence to the optimal solution.

The components considered, in this first iteration, for the navigation system, are high-performance but relatively bulky when compared with the size of the drone. In the future, it could be taken into account to decrease the performance of the individual components in order to have more space for other subsystems.

The first work that will be done in the future is to optimize the image acquisition system, then the optics and the camera.

The feedback that has been obtained at the moment with regard to the optics is inherent to an Italian company, which has proposed to develop a variable FOV optic via a motor. The FOV would vary between about 120° and about 50° respectively used in the first phase for navigation and inside the crater to shoot the images.

As far as the camera is concerned, we are already in communication with another Italian company, which also develops the communication and image storage system and also the visual navigation algorithm. The

solution proposed at the moment and under development would be a 12 Mpx camera, but in order to increase the frame rate for navigation, it is possible to reduce, as mentioned before, the FOV and the resolution. This reduction will take into account various parameters and will allow us to have at least 15 FPS for the navigation phase.

For camera dimensions they propose about 52x71x25mm while for the Storage & Data handling module they propose 80x80x25mm. These modules can also be separated and flexible PCBs are used to connect them. Finally, an additional module is required for image transmission.

For the transmission they propose an x band at 8 GHz which requires a few tens of *mW* and which works at 40-50 Mbit/s. With these parameters the transmission of 12 MPx images, which will also be compressed, requires 0,2s - 1s.

Another future work is to deepen what addressed in chapter 5, i.e. navigation inside the crater, to be able to develop an autonomous navigation system capable of flying inside the tunnels and that is compact enough to fit in the drone.

Finally, it is necessary to deepen the approach to the rover and the landing phase, these two phases still need to be studied in more detail and optimized. These are very critical phases and also require the study of other systems such as, for example, the communication system and the attitude control algorithm.

8 References

- [1] R. Greeley, «Lava Tubes and Channels at Lunar Marius Hills,» [Online]. Available: <https://ntrs.nasa.gov/archive/nasa/casi.ntrs.nasa.gov/19710008532.pdf>.
- [2] J. Universities, «Mission Concepts of Unprecedented Zipangu Underworld of the Moon Exploration».
- [3] H. e. al., «Possible lunar lava tube skylight observed by SELENE cameras».
- [4] «Photojournal JPL,» [Online]. Available: <https://photojournal.jpl.nasa.gov/catalog/PIA12954>.
- [5] NASA. [Online]. Available: <https://www.nasa.gov/content/goddard/lunar-pits-could-shelter-astronauts-reveal-details-of-how-man-in-the-moon-formed>.
- [6] L. Chappaz, «Evidence of large empty lava tubes».
- [7] A. Arya, «Detection of potential site for future human habitability on the Moon using Chandrayaan-1 data,» 2011.
- [8] W. Whittaker, «Technologies Enabling Exploration of Skylights, Lava Tubes and Caves,» in *NASA Innovative Advanced Concepts (NIAC) Phase I*, 2011.
- [9] U. Today. [Online]. Available: <https://www.universetoday.com/tag/lunar-lava-tubes/>.
- [10] S. S. T. M. T. y. S. F. I. N. Junichi Haruyama, «Exploration of Lunar Holes, Possible Skylights of Underlying Lava Tubes, by Smart Lander for Investigating Moon,» 2011.
- [11] NASA. [Online]. Available: <https://www.nasa.gov/content/commercial-lunar-payload-services-overview>.
- [12] iSpace. [Online]. Available: <https://ispace-inc.com/project/>.
- [13] S. Pescaglia, «Preliminary design of a Lunar Nano Drone for a mission of exploration of lava tubes on the Moon: study of the Mission Flight Profile and identification of the most suitable Energy Storage System,» 2020.
- [14] G. Podestà, «Lunar Nano Drone for a mission of exploration of lava tubes on the Moon: Navigation System,» 2020.
- [15] E. K. L. C. F. C. R. G. M. H. Reid Simmons, «Experience with Rover Navigation for Lunar-Like Terrains».
- [16] «Visual SLAM algorithms: a survey from 2010 to 2016,» [Online]. Available: <https://link.springer.com/article/10.1186/s41074-017-0027-2#author-information>.
- [17] C. R. L. JP, «Position referencing and consistent world modeling for mobile robots».
- [18] B. T. Durrant-Whyte H, «Simultaneous localization and mapping: part i. Robot Autom Mag IEEE».
- [19] D.-W. H. Bailey T, «Simultaneous localization and mapping (slam)».
- [20] L. J. Thrun S, «Handbook of robotics. Chap. Simultaneous localization and mapping,» 2008.
- [21] P. Y. S. J. L. X. Aulinas J, «The slam problem: a survey In: Proceedings of Conference on Artificial Intelligence Research and Development,» 2008.
- [22] C. A. L. G. Billingham M, «A survey of augmented reality. Found Trends Human-Computer Interact,» 2015.
- [23] S. J. C. D. Engel J, «Camera-based navigation of a low-cost quadcopter,» 2012.
- [24] K. A. S. K. Klette R, «Computer vision: three-dimensional data from images,» 1998.
- [25] N. D, «Proceedings of IEEE Conference on Computer Vision and Pattern Recognition,» *A minimal solution to the generalised 3-point pose problem*, 2004.
- [26] K. R. S. C. B. W. Grisetti G, «A tutorial on graph-based slam. Intell Transp Syst Mag IEEE,» 2010.
- [27] G. G. S. H. K. K. B. W. Kümmerle R, «Proceedings of International Conference on Robotics and Automation,» *A general framework for graph optimization*, 2011.
- [28] M. P. H. R. F. Triggs B, «Vision algorithms: theory and practice,» 2000.

- [29] M. D. Klein G, «Proceedings of International Symposium on Mixed and Augmented Reality,» *Parallel tracking and mapping for small AR workspaces*, 2007.
- [30] S. J. C. D. Engel J, «Proceedings of International Conference on Computer Vision,» *Semi-dense visual odometry for a monocular camera*, 2013.
- [31] S. T. C. D. Engel J, «LSD-SLAM: large-scale direct monocular SLAM,» *Proceedings of European Conference on Computer Vision*, 2014.
- [32] S. J. C. D. Kerl C, «Robust odometry estimation for RGB-D cameras,» *Proceedings of International Conference on Robotics and Automation*, 2013.
- [33] S. J. C. D. Kerl C, «Dense visual SLAM for RGB-D cameras,» *Proceedings of International Conference on Intelligent Robots and Systems*, 2013.
- [34] F. Y. S. N. S. I. C. B. S. S. S. R. Agarwal S, «Building rome in a day,» 2011.
- [35] D. AJ, «Real-time simultaneous localisation and mapping with a single camera».
- [36] D. AJ, «Real-time simultaneous localisation and mapping with a single camera,» *Proceedings of International Conference on Computer Vision*, 2003.
- [37] R. I. M. N. S. O. Davison AJ, «Monoslam: real-time single camera SLAM,» 2007.
- [38] M. D. Klein G, «arallel tracking and mapping for small AR workspaces».
- [39] N. D, «An efficient solution to the five-point relative pose problem».
- [40] K. G. R. I. Williams B, «Real-time SLAM relocalisation In: Proceedings of International Conference on Computer Vision».
- [41] N. D, «An efficient solution to the five-point relative pose problem,» 2004.
- [42] K. G. R. I. Williams B, «Real-time SLAM relocalisation,» *Proceedings of International Conference on Computer Vision*, 2007.
- [43] M. J. D. A. Strasdat H, «Visual SLAM: why filter?».
- [44] S. G. C. M. N. P. R. I. Mei C, «A constant-time efficient stereo slam system».
- [45] N. P. Cummins M, «probabilistic localization and mapping in the space of appearance».
- [46] M. J. D. A. Strasdat H, «Scale drift-aware large scale monocular slam».
- [47] M. J. T. J. Mur-Artal R, «ORB-SLAM: a versatile and accurate monocular SLAM system».
- [48] T. J. Mur-Artal R, «ORB-SLAM2: an open-source SLAM system for monocular, stereo and RGB-D cameras».
- [49] K. T. Okutomi M, «A multiple-baseline stereo. Pattern Anal Mach Intell IEEE Trans».
- [50] O. S. F. E. Rudin LI, «Nonlinear total variation based noise removal algorithms. Phys D Nonlinear Phenom».
- [51] L. S. D. A. Newcombe RA, «DTAM: dense tracking and mapping in real-time,» *Proceedings of International Conference on Computer Vision*, 2011.
- [52] K. P. I. S. Ondruska P, «MobileFusion: real-time volumetric surface reconstruction and dense tracking on mobile phones,» 2015.
- [53] G. S. C. D. Stühmer J, «Real-time dense geometry from a handheld camera,» 2010.
- [54] S. J. C. D. Engel J, «Semi-dense visual odometry for a monocular camera,» *Proceedings of International Conference on Computer Vision*, 2013.
- [55] S. J. C. D. Engel J, «Semi-dense visual odometry for a monocular camera».
- [56] S. T. C. D. Engel J, «arge-scale direct monocular SLAM».
- [57] E. J. C. D. Schöps T, «Semi-dense visual odometry for AR on a smartphone».
- [58] E. J. C. D. Caruso D, « Large-scale direct SLAM for omnidirectional cameras».
- [59] M. I. Baker S, «Lucas-kanade 20 years on: a unifying framework».

- [60] P. M. S. D. Forster C, «SVO: fast semi-direct monocular visual odometry,» *Proceedings of International Conference on Robotics and Automation*, 2014.
- [61] K. V. C. D. Engel J, «Direct sparse odometry,» 2016.
- [62] M. N. Besl PJ, «A method for registration of 3-d shapes».
- [63] I. S. H. O. M. D. K. D. D. A. K. P. S. J. H. S. F. A. Newcombe RA, «KinectFusion: real-time dense surface mapping and tracking,» *Proceedngs of International Symposium on Mixed and Augmented Reality*, 2011.
- [64] G. B. K. P. D. A. Salas-Moreno RF, «Dense planar SLAM».
- [65] N. R. Salas-Moreno RF, «simultaneous localisation and mapping at the level of objects».
- [66] T. F. N. N. Tateno K, «When 2.5D is not enough: Simultaneous reconstruction, segmentation and recognition on dense SLAM».
- [67] K. M. H. E. R. X. F. D. Henry P, «RGB-D mapping: using Kinect-style depth cameras for dense 3D modeling of indoor environments».
- [68] H. J. E. N. S. J. C. D. B. W. Endres F, «An evaluation of the RGB-D SLAM system,» *Proceedings of International Conference on Robotics and Automation*, 2012.
- [69] H. J. E. N. S. J. C. D. B. W. Endres F, «An evaluation of the RGB-D SLAM system In: Proceedings of International Conference on Robotics and Automation».
- [70] L. S. D. A. Newcombe RA, «DTAM: dense tracking and mapping in real-time,» *Proceedings of International Conference on Computer Vision*, 2011.
- [71] S. J. C. D. Kerl C, «Dense visual SLAM for RGB-D cameras».
- [72] K. M. L. J. M. J. Whelan T, «Deformation-based loop closure for large scale dense RGB-D SLAM».
- [73] L. S. M. R. G. B. D. A. Whelan T, «ElasticFusion: dense slam without a pose graph».
- [74] S. D. R. G. Pirchheim C, «andling pure camera rotation in keyframe-based SLAM».
- [75] K. K. K. J. P. K. H. J. Herrera C, «Dt-slam: deferred triangulation for robust SLAM».
- [76] R. M. R. G. W. D. Mulloni A, «Proceedngs of International Symposium on Mixed and Augmented Reality».
- [77] P. C. V. J. S. D. L. V. Arth C, «nstant outdoor localization and SLAM initialization from 2.5 d maps».
- [78] B. D. D. A. M. J. Civera J, «Camera self-calibration for sequential bayesian structure from motion».
- [79] H. J. Taketomi T, «Focal length change compensation for monocular slam».
- [80] K. R. G. L. Pollefeys M, «elf-calibration and metric reconstruction in spite of varying and unknown internal camera parameters».
- [81] C. C. R. I. Kim JH, «Direct semi-dense SLAM for rolling shutter cameras».
- [82] H. T. Lee T, «Multithreaded hybrid feature tracking for markerless augmented reality».
- [83] K. D. Knorr SB, «Leveraging the user's face for absolute scale estimation in handheld monocular SLAM».
- [84] K. J. S. S. M. J. H. J. Mustaniemi J, «Inertial-based scale estimation for structure from motion on mobile devices».
- [85] K. H. Tamura H, «roposal of international voluntary activities on establishing benchmark test schemes for ar/mr geometric registration and tracking methods».
- [86] O. T. I. T. N. L. K. T. Makita K, «Virtualized reality model-based benchmarking of AR/MR camera tracking methods in TrakMark».
- [87] M. M. F. K. Martull S, «Realistic CG stereo image dataset with ground truth disparity maps».
- [88] E. N. E. F. B. W. Sturm J, «A benchmark for the evaluation of RGB-D SLAM systems».
- [89] L. P. U. R. Geiger A, «Are we ready for autonomous driving? The kitti vision benchmark suite».

- [90] B. B. Z. M. M. J. N. A. K. P. D. A. L. M. O. M. R. G. T. N. F. S. Nardi L, «Introducing SLAMBench, a performance and accuracy benchmarking methodology for SLAM».
- [91] «Table 2,» [Online]. Available: <https://link.springer.com/article/10.1186/s41074-017-0027-2/tables/1>.
- [92] Z. J, «Singh S. Low-drift and Real-time Lidar Odometry and Mapping. Auton. Robots,» [Online].
- [93] «A Review of Visual-LiDAR Fusion based Simultaneous Localization and Mapping,» [Online]. Available: <https://www.mdpi.com/1424-8220/20/7/2068/htm>.
- [94] L. K. H. J. S. H. Nuchter A., «6D SLAM—3D mapping outdoor environments,» [Online].
- [95] L. J. Z. L. H. Y. Li R., «LIDAR/MEMS IMU integrated navigation (SLAM) method for a small UAV in indoor environments,» [Online].
- [96] V. D, «Extracting Proprioceptive Information By Analyzing Rotating Range Sensors Induced Distortion,» [Online].
- [97] M. H. Besl P., « A method for registration of 3-D shapes,» [Online].
- [98] Z. J, « Low-drift and Real-time Lidar Odometry and Mapping. Auton. Robots,» [Online].
- [99] H. D. Segal A., «Science and Systems. MIT Press,» [Online].
- [100] K. L. Diosi A., «Fast Laser Scan Matching using Polar Coordinates,» [Online].
- [101] G. G. Konolige K., «Efficient Sparse Pose Adjustment for 2D mapping,» [Online].
- [102] C. T. Crocoll P., «Laser-aided navigation with loop closure capabilities for Micro Aerial Vehicles in indoor and urban environments,» [Online].
- [103] S. C. B. Grisetti G., «Improved Techniques for Grid Mapping With Rao-Blackwellized Particle Filters,» [Online].
- [104] S. C. Grisetti G., «Improving grid-based slam with rao-blackwellized particle filters by adaptive proposals and selective resampling,» [Online].
- [105] T. R. Martín F., «Two different tools for three-dimensional mapping: DE-based scan matching and feature-based loop detection,» [Online].
- [106] K. D. R. H. Hess W., «Real-time loop closure in 2D LIDAR SLAM,» [Online].
- [107] M. M, «Appearance-Based Loop Detection from 3D Laser Data Using the Normal Distributions Transform,» [Online].
- [108] C. T. H. B. L. M. Crocoll P., «Laser-aided navigation with loop closure capabilities for Micro Aerial Vehicles in indoor and urban environments,» [Online].
- [109] U. R, «Fast Extrinsic Calibration of a Laser Rangefinder to a Camera,» [Online].
- [110] P. T. Kassir A., «Reliable automatic camera-laser calibration,» [Online].
- [111] K. S. Park K., «High-Precision Depth Estimation Using Uncalibrated LiDAR and Stereo Fusion,» [Online].
- [112] Z. Y. L. C. Sun F., «Research on active SLAM with fusion of monocular vision and laser range data,» [Online].
- [113] O. Y. X. T. Xu Y., «SLAM of Robot based on the Fusion of Vision and LIDAR,» [Online].
- [114] G. S. Guillén M., «Sensorial Simultaneous Localization and Mapping (SLAM) System for Low-Cost Micro Aerial Vehicles in GPS-Denied Environments,» [Online].
- [115] W. A. Graeter J., «Lidar-monocular visual odometry,» [Online].
- [116] P. Y. K. A. Shin Y.S., «Direct visual SLAM using sparse depth for camera-lidar system,» [Online].
- [117] R. J. De Silva V., « Fusion of LiDAR and camera sensor data for environment sensing in driverless vehicles,» [Online].
- [118] Z. R. L. E. Y. K. Zhang Z., «Scale Estimation and Correction of the Monocular Simultaneous Localization and Mapping,» [Online].
- [119] R. J. A. S. Scherer S., «River Mapping From a Flying Robot: State Estimation, River Detection, and Obstacle Mapping,» [Online].

- [120] X. J. S. C. Huang K., «Accurate Direct Visual-Laser Odometry with Explicit Occlusion Handling and Plane Detection,» [Online].
- [121] C. H. Liang X., «Visual laser-SLAM in large-scale indoor environments,» [Online].
- [122] Y. S. D. H. Zhu Z., «Loop Detection and Correction of 3D Laser-Based SLAM with Visual Information,» [Online].
- [123] M. J. Pandey G., «Visually bootstrapped generalized ICP,» [Online].
- [124] C. C. Seo Y., «A Tight Coupling of Vision-Lidar Measurements for an Effective Odometry,» [Online].
- [125] S. S. Zhang J., «Visual-lidar Odometry and Mapping: Low-drift, Robust, and Fast,» [Online].
- [126] L. Y. J. S. T. C. M. X. Jiang G., «A Simultaneous Localization and Mapping (SLAM) Framework for 2.5D Map Building Based on Low-Cost LiDAR and Vision Fusion,» [Online].
- [127] «IMU 42,» [Online]. Available: https://www.cielo-inertial.com/wp-content/uploads/2019/10/Cielo_IMU42_F_Datasheet-1.pdf.
- [128] «Led white,» [Online]. Available: <https://www.ebay.com/itm/Warm-White-High-Power-80W-LED-Panel-Energy-Saving/160922202554?hash=item2577b5f1ba:g:KLcAAOxyY3ZR4Ryw>.
- [129] «LiDAR Ultra Puck,» [Online]. Available: http://www.3dtarget.it/eu/images/stories/virtuemart/product/Velodyne_VLP-32C_Datasheet_Web_FINAL_it.pdf.
- [130] «LiDAR Z,» [Online]. Available: <https://autonomoustuff.com/wp-content/uploads/2020/10/valeo-scala-datasheet-whitelabel.pdf>.
- [131] «OBC,» [Online]. Available: https://www.aac-clyde.space/assets/000/000/181/AAC_DataSheet_Sirius_OBC_-_updated_tables_original.pdf?1601990253.
- [132] «High-performance distance sensor,» Micro epsilon, [Online]. Available: https://www.micro-epsilon.com/displacement-position-sensors/laser-distance-sensor/optoNCDT_ILR_1191/.
- [133] [Online]. Available: <https://www.omnicalculator.com/physics/lumen>.
- [134] [Online]. Available: <http://www.dmslighting.com/tools/illuminationconverter.html>.
- [135] E. A. F. K. A. H. Kerry Snyder, «AstroNav: Engineering Robust Subterranean State Estimation for Lunar Exploration».
- [136] «Thermal management of leds lamp,» [Online]. Available: <https://www.cree.com/led-components/media/documents/XLampThermalManagement.pdf>.
- [137] O. B. Samuel W. Ximenes and J. O. Elliott, «Defining a Mission Architecture and Technologies for Lunar Lava Tube Reconnaissance,» 2012.
- [138] M. Robinson, «Annual Meeting of the Lunar Exploration Analysis Group, ARNE - SUBLUNAREAN EXPLORER,» 2014.
- [139] NASA, 17 July 2014. [Online]. Available: <https://www.nasa.gov/content/goddard/lunar-pits-could-shelter-astronauts-reveal-details-of-how-man-in-the-moon-formed>.
- [140] [Online]. Available: <http://www.progettazioneottica.it/unita-fotometriche-lumen-candele-lux/1172>.
- [141] «ImperX,» ImperX, [Online]. Available: <https://www.imperx.com/cmos-cameras/C2420/>.